DEPARTMENT OF MECHANICAL & AEROSPACE ENGINEERING

NUMERICAL OPTIMISATION OF LOW ALLOY STEEL FRICTION STIR WELDING

BILAL AHMAD

A thesis submitted in fulfilment of the requirements for the

degree of Doctor of Philosophy

2019

This thesis is the result of the author’s original research. It has been composed by the author and has not been previously submitted for examination, which has led to the award of a degree.

Signed: Bilal Ahmad Date: 21st January 2019

Abstract

The development of advanced joining processes such as friction stir welding (FSW) is necessary to maintain manufacturing competitiveness in any industrial nation. Substantial research that has been carried out on FSW of aluminium alloys has demonstrated considerable benefits; this has led to greater interest in FSW of steel and other high melting temperature alloys. In this context, numerical modelling can provide cost-effective development of steel FSW.

This thesis is focussed on a three dimensional thermomechanical simulation of FSW in Abaqus/Explicit, featuring low alloy steel with previously generated experimental temperature dependant properties. Unlike any previous numerical research in which either the workpiece is assumed as a highly viscous body or the tool is modelled as a moving heating source, the Coupled Eulerian Lagrangian approach has been innovatively applied to model the FSW process on steel. All stages of FSW (plunge, dwell and traverse) have been modelled for slow and fast process parameters and their results compared with previous experimental work on the same grade of steel. Various numerical results, such as temperature distribution, plastic strain, reaction forces, material flow and flash generation, were analysed for both models. In each model, the weld shape and weld surface flash were found to be in exceptionally close alignment with previous experimental results.

To optimise the FSW process and reduce the forces on the tool, laser assisted FSW (LAFSW) on steel has been numerically developed and analysed as a viable process amendment. LAFSW increased the traverse speed from 500 mm/min to 1500 mm/min, significantly higher than conventional steel FSW. The application of laser assistance with a distance of 20 mm from the rotating tool reduced the reaction forces on the tool probe tip up to 55% as compared to standard FSW during the plunge stage.

Acknowledgements

Firstly, I thank Allah Almighty to providing me such a blissful life, and an ability to interpret and extend the knowledge.

I would like to express my sincere gratitude to my supervisors, Dr. Alexander M Galloway and Dr. Athanasios I Toumpis, for their continued guidance, advice and encouragement throughout this research. It is indeed an honour for me to work with such an experienced and dedicated supervisors like them. I am indebted to their kind and indefatigable assistances in refining my skills on both professional and personal level.

Huge thanks to my beloved Ami, Abu and Mamujaan for believing in me. It would had not been possible without the unconditional love and support from them. I would had not be who I am today without them. I dedicate this thesis to them.

I would like to thank my sisters (Dede and Meme), brother (Bhai), friends (Jd, Qureshi, Fazi, Ali, Arshad lala, Jawad lala, Shahzad bhaou and Abdul bhai) and the Glasvegas group. They are a big part of my personality. Exclusive acknowledgements for the support of Meme and Fazi in getting through some of the worst times of depression during my PhD. I love you people.

I thank everyone who contributed to this thesis, directly or indirectly.

Contents

1. Introduction

1.1. Background

The aim of every structural design is to consider the cost effectiveness and the optimisation of material utilisation under the provided specifications. The fabrication of such structural designs often requires efficient joints to achieve both of the aforementioned objectives. The application of an advanced joining process, known as friction stir welding (FSW), has proven to be a strong contender for joining a wide range of metallic materials. It was developed at The Welding Institute (TWI) for aluminium and patented in 1991 by Thomas et al. [1.1]. It is a solid state joining process that uses a rotating tool to plasticise the material during welding [1.2,1.3]. Figure 1.1 shows an illustration of FSW. Heat is generated due to the frictional contact between the rotating tool and the workpiece, which in turn, softens the material around the tool [1.4,1.5], resulting in localised plastic deformation referred to as metal stirring. The factors affecting the quality of friction stir (FS) welds are, among other things, the rotational and traverse speed of the tool, the plunging force of the tool on the workpiece, and the contact angle between the tool and the workpiece [1.6-1.8].

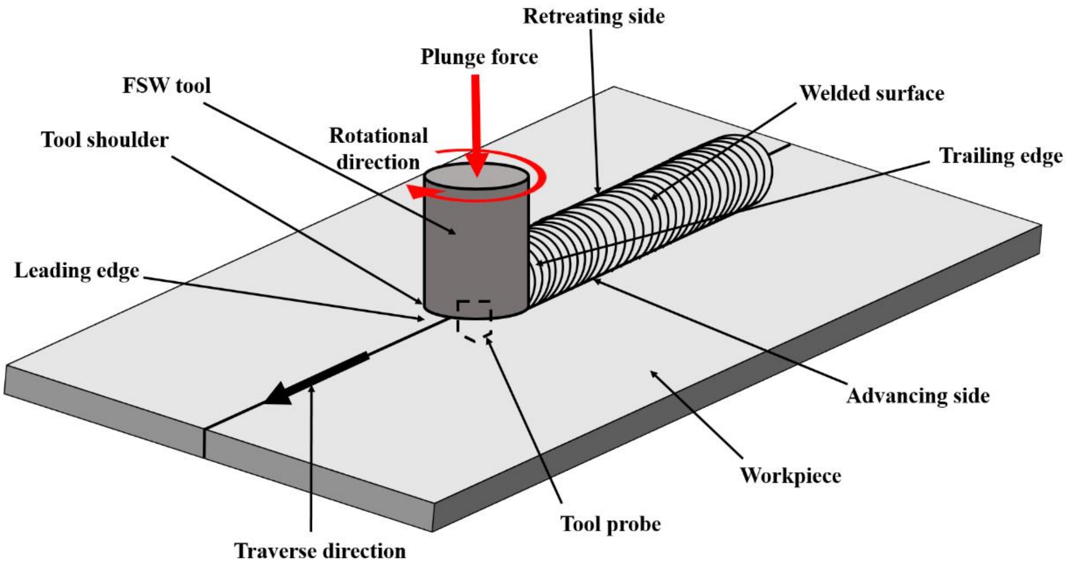

Figure 1.1. A schematic diagram of FSW.

Compared to liquid state welding techniques that are conventionally used in industry [1.9], FSW has the ability to generate higher quality welds with enhanced fatigue strength. Several studies have shown that the elimination of porosity [1.10], cracking [1.11] and distortion [1.12] can be achieved with FSW. Since FSW takes place below the melting temperature of the material, significantly less energy is consumed during the process [1.10]. The FSW tool covers the joint gap during the welding process, hence there is no need for any additional shielding gas or smoke extraction equipment during the process [1.11,1.13]. This offers great opportunities in terms of process automation and integration in industry.

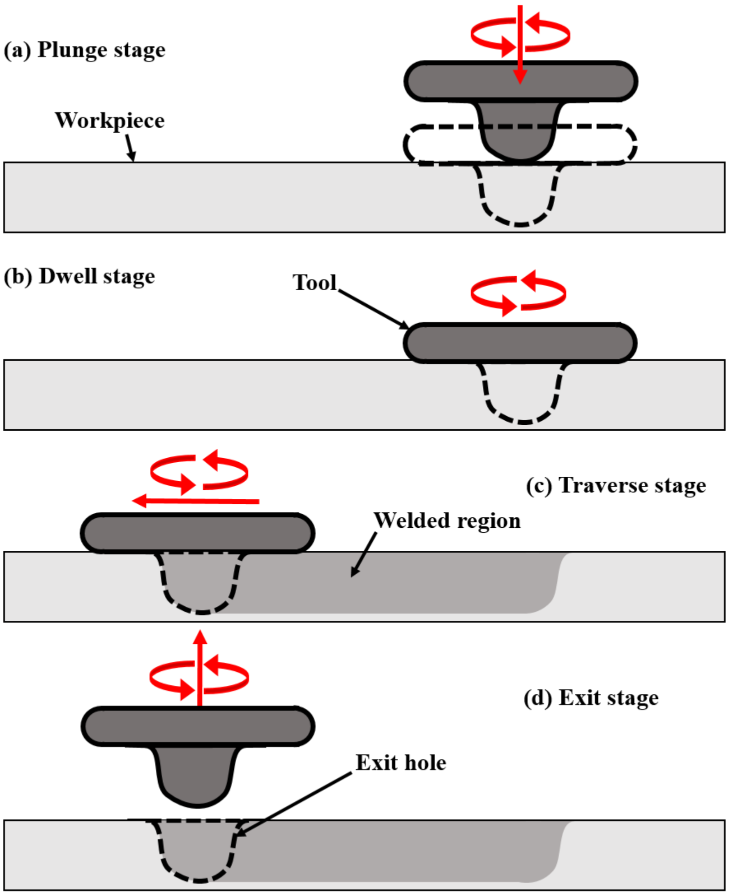

Figure 1.2: All four stages of FSW.

FSW can generally be divided into four main stages [1.14], as shown in Figure 1.2.

1. Plunge: The rotating tool penetrates into the workpiece until the tool shoulder makes contact with the surface of the materials.
2. Dwell: The tool keeps on rotating until enough frictional heat is generated to plasticise the surrounding material of the workpieces.
3. Traverse: The workpieces are welded by moving the rotating tool in the welding

direction under an axial force.
4. Exit: The welding tool is retracted from the welded workpieces after reaching the preferred length.

The plunge stage can be compared to hole drilling where the wear resistant rotating tool is bored inside the workpieces but without any corresponding material removal (Figure 1.2. (a)). In the dwell stage, the materials to be welded are initially softened and plasticised locally around the tool (Figure 1.2. (b)). During this time, the heat introduced into the workpieces disperses and thus precedes the process, which facilitates the welding in the traverse stage. In the traverse stage, the movement of the rotating tool in the weld direction assists in the mixing of each material, hence forming a weld (Figure 1.2. (c)). In contrast to fusion welding, a weld is not achieved by the local melting, but is produced by mixing the viscous material in the solid state. After the desired length of the weld is achieved, the tool is removed from the workpiece in the exit stage, leaving a hole at the end position, as shown in Figure 1.2. (d). The exit hole poses no problems for most applications as a removable scrap plate can be attached to the workpiece [1.15]. In that case, the exit stage is then performed on the scrap plate, leaving the finished workpiece with a fine weld without any hole in it.

1.1.1. Process parameters

FSW includes many modifiable features to influence the weld properties. These factors, known as the process parameters, are the tool's [1.6]:

1. Rotational speed.
2. Traverse speed.
3. Plunge depth.
4. Tilt angle.

The industrial FSW systems are capable of welding with a traverse speed of up to 3 m/min [1.16]. The reported tool's rotational speeds for steel FSW are typically between 100 and 1000 revolutions per minute [1.2,1.3,1.17]. The rotational speed is directly related to the softening and the mixing of the material due to its direct influence on the friction and the heat input during FSW. The tool's rotation produces an asymmetry in the weld profile when the tool is traversed in the weld direction. This is due to the superposition of the tool's rotation and the translation, which causes an asymmetrical material flow [1.18]. The FSW tool can be controlled by two techniques:

1. Position control
2. Force control

In the case of position control, the tool is placed at a constant distance from the workpiece irrespective of the forces being applied on it [1.19], whereas in the force control technique, the traverse is due to the application of an axial force on the tool in the direction of the weld [1.20]. The tilt angle of the tool is the angle of the tool's central axis from the vertical axis [1.21]. A tilt angle up to 3.5^o has been reported for the investigations related to steel FSW [1.22,1.23]. The main purpose of the tilt angle is to provide a continuous supply of the material in the stir zone along with compressing the weld pool from the trailing edge of the tool shoulder [1.11]. However, the tilt angle is avoided by introducing various modifications to the structure of the shoulder, such as grooves or concentric circles, for an enhanced material flow [1.11]. In addition to the main process parameters mentioned above, there are some other factors whose variations may affect FSW [1.2]. These may include the plunge depth, the tool cooling, the backing plate and the clamping configuration of the workpieces during all stages of FSW [1.2].

1.1.2. FSW Nomenclature

Since FSW is a localised plastic deformation process, FS welds have a characteristic morphology unlike fusion welding [1.24]. A basic understanding of the main regions of the FS weld is necessary before studying further aspects of FSW in the subsequent chapters. For this reason, a nomenclature is adopted for the zones of a FS welded joint from previous researches [1.2,1.25-1.27]; this has been illustrated in Figure 1.3.

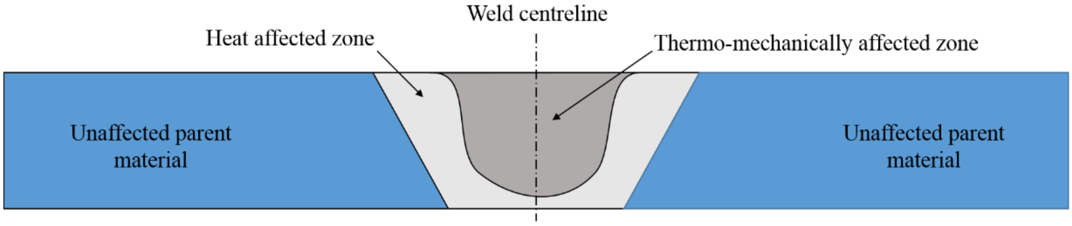

Figure 1.3: Illustration of the characteristic morphology of the FS weld.

The FS welded plates typically have three distinct zones with different characteristics; thermomechanically affected zone (TMAZ), heat affected zone (HAZ) and the unaffected parent material [1.25]. The centre zone of the weld is the TMAZ. This region is subjected to a large plastic deformation during the welding process, which results in a fine and dynamically recrystallised structure. As a result, a weld nugget is developed in this zone. As the tool rotation is influenced from the traverse direction, an asymmetrical shape is developed in the stir zone with respect to the weld centreline [1.19]. In general, the characteristic onion ring structure of FS welds only shows up in the nugget area in the transverse sectioning [1.28,1.29].

A HAZ is formed at the boundary of the TMAZ, as shown in Figure 1.4. Although the HAZ is not subjected to any noticeable plastic deformation, the process heat can also change the microstructure in this zone [1.25]. The HAZ is surrounded by the parent material, in which no effects of the process are recognised due to FSW being highly localised [1.2,1.26].

1.1.3. Tool characteristics

From section 1.1.1, it is clear that both the plasticisation of the workpiece material and its mixing is accomplished by a single rotating tool. Therefore, characteristics of the tool such as its geometry and material properties play a significant role in FSW [1.10,1.11]. The tool's geometry governs the stirring effect of the material, which therefore influences the mechanical properties and quality of the weld [1.6], while the material of the tool determines the weld quality as an influence of the heat generation and the heat transfer in the workpiece [1.10]. The design of the FSW tool is primarily influenced by the material selection, geometry and production cost. The tool technology for welding steel is comparatively underdeveloped, and more research needs to be conducted to ensure that the whole welding process becomes entirely independent from the tool life [1.17]. This is the reason that the tool's geometry and material are subjects of constant optimisation [1.11,1.30]. The tool in its basic form consists of two essential components, the cylindrical tool shoulder and a centrally protruding welding pin, also known as the probe, as shown in Figure 1.4. There are two main functions of the tool shoulder in FSW:

1. It directs the large proportion of the process forces to the workpiece [1.11].
2. It covers the joining zone, such that any plasticised material is trapped under the shoulder [1.11], hence producing a smooth surface finishing [1.31].

The shoulder is often designed as concave or convex to achieve minimum flash and defect free welds [1.10]. The tool shoulder also generates heat, and influences the mixing of the material near the workpiece surface [1.11]. The main task of the tool probe is to improve material mixing in the TMAZ [1.6,1.32]. For this purpose, the tool probe is completely plunged in the workpieces during the welding process. In addition, the probe's shape also impacts the weld properties by influencing the material flow in the TMAZ [1.33]. Therefore, it is often provided with threads or grooves that further help in intermixing the plasticised material from the workpiece surface to the material near the weld root. In the simplest embodiment, the tool probe is designed as a cylinder or truncated cone. This is generally adequate as long as the shoulder provides a sufficient heat generation since about 80% of the heat is generated from the tool shoulder [1.34]. In addition, to improve the material flow in the workpiece, vertical and horizontal features such as the aforementioned spiral grooves, threads or other tool triangular or square probe geometries exist [1.15,1.35-1.37]. Also, there are other adapted tool geometries for special purpose applications such as parallel, tandem or overlapping welds [1.15].

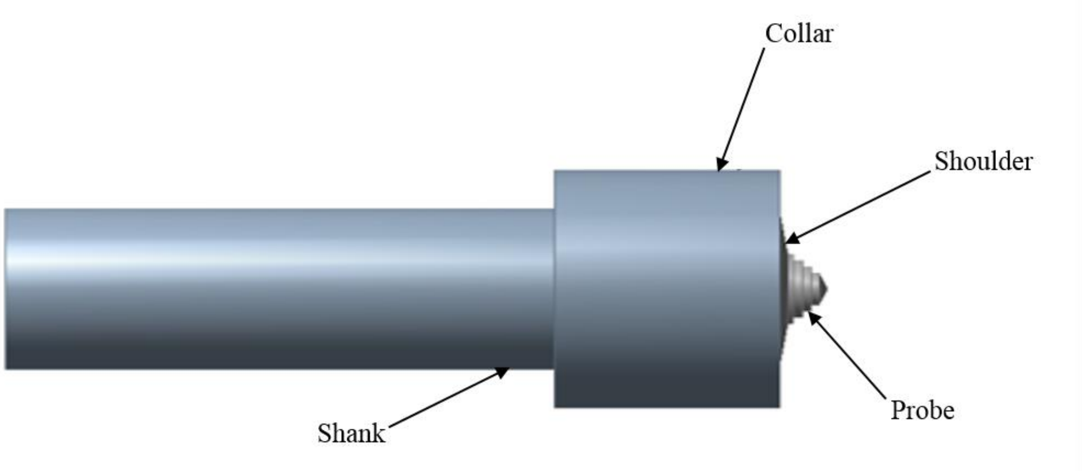

Figure 1.4: FSW tool.

The tool material can significantly influence FSW [1.10,1.11]. For instance, the heat balance of the process is achieved by the heat conduction and the heat capacity of the tool. The material itself, or the tool's surface coating, can make an impact on the desired heat output as well as the workpiece material flow. Therefore, different properties of the material are required to optimise the above-mentioned factors. Essentially, the following properties are crucial for the suitability of the tool material [1.10,1.11]:

1. It must have sufficient strength at the elevated operating temperatures.
2. It must be sufficiently resistant to wear during the plunge and the traverse stage.
3. It must have a low coefficient of thermal expansion so that the thermal stresses are minimised.
4. The cost of the material and its manufacturing should be affordable.
5. It must have no detrimental reaction with the workpiece material. It should be chemically inert with respect to the workpieces materials being joined.

With regard to the process reliability, it is necessary that the tool structure does not fail due to the continuous wear, hence resulting in poor weld quality and high production cost [1.38]. In addition, significant dynamic loads, such as contact shock or periodic process forces, can often cause the tool to fail due to fatigue. The failure usually takes place in the area of the highest stress concentration, which is the tool probe during FSW [1.18,1.39]. It is therefore necessary to take into account the fatigue behaviour of the tool material, especially for the complex geometries.

1.1.4. Selection of the FSW tools

To FS weld a high melting temperature material such as low alloy steel, an even higher melting temperature material is required to be used as a tool. This makes steel tools a viable option when welding low melting temperature materials such as aluminium alloys, aluminium matrix composites (AMC) and magnesium alloys [1.10,1.40]. Steel tools are also used for the joining of low melting temperature dissimilar materials for both butt and lap welding configurations [1.7,1.41,1.42]. The requirement of the tool materials entirely changes for welding higher melting temperature materials such as steel or titanium alloys. For the welding of such materials, wear resistant and high strength materials are needed as a tool. These requirements can be partly fulfilled by using super alloys such as Nimonic 105 or Inconel 718 [1.40,1.43,1.44]. There are also refractory alloy-based tools, such as tungsten carbide or molybdenum, and ceramic composites, such as polycrystalline cubic boron nitride (pcBN) [1.5,1.45-1.47], as shown in Figure 1.5. pcBN is often chosen due to its high temperature stability, strength and hardness to weld steel and similar high strength materials such as titanium alloys [1.2,1.17,1.27,1.48,1.49]. Since pcBN offers a low coefficient of friction, this assists in providing smooth weld surfaces [1.50]. However, the pcBN material is considered expensive and has also been shown to exhibit cracks and significant wear due to its low fracture toughness [1.10].

Figure 1.5: FSW tool with pcBN probe and shoulder [1.46].

1.2. Limitations and research challenges of steel FSW

Based on the numerous advantages of the process, FSW has been successfully applied for the welding of aluminium alloys and other low melting alloys [1.3,1.10,1.32,1.51,1.52]. However, despite of the extensive research being carried out on steel FSW [1.2,1.19,1.26,1.53,1.54], the commercialisation of FSW for steel application has significant limitations, mainly due to the high cost and short life of the tool [1.3,1.10,1.26]. The cost of a FSW tool for steel is approx. €3,000 (based on 2018 cost) with a maximum service life of about 40 m [1.26], although this is controlled by process parameters. Due to the solid state nature of the process, the tool experiences severe stresses mainly during the plunge stage [1.10]. These stresses are caused by the high tool speeds or lack of preheating of the workpiece, hence often resulting in failure of the tool [1.55]. The short life of the tool consequently increases the tooling cost of the welds [1.56], thus making it commercially unviable. In addition, the slow traverse speeds of steel FSW increase the overall process duration, hence affecting the productivity in potential industrial applications [1.2].

Many fundamental phenomena of steel FSW, such as material flow or defect formation, which are crucial for the quality of the welded component, are still not adequately explained. An extensive research study is required to comprehend the principal problems of steel FSW. A significant insight about these issues can be obtained by numerical modelling of FSW, which will also save the cost, time and efforts to setup an experimental programme [1.6]. Since all previous research work on numerical modelling of steel FSW assume, either the tool as a virtual heat source or the workpiece as a highly viscous fluid, a fully coupled thermomechanical model is required by considering both the tool and the workpiece as solids. Moreover, the numerical models in the previous research work mainly take theoretical based material properties into account for steel FSW instead of the experimentally generated material data. Therefore, the use of experimentally generated material data considerably improves the accuracy of the modelling results for steel FSW.

The aim of this novel work is to contribute to the understanding of FSW for low alloy steel through numerical modelling. Based on an analytical comparison with a recent industrial scale experimental investigation [1.2], a thermomechanical model will be developed, which will comprehensively describe various results in all stages of FSW. The use of an advanced numerical approach, known as Coupled Eulerian Lagrangian (CEL), along with the experimentally generated temperature dependent material properties of steel will enable the investigation of the physical phenomenon of FSW, along with predicting the temperature distribution, plastic strain, material flow visualisation, weld shape and flash generation in the workpiece, and the reaction forces on the FSW tool. All these aspects will assist in producing more realistic results, and have not been previously presented for steel FSW.

To address the issues related to the slow traverse speeds and maximum reaction forces on the tool, a feasibility of the introduction of an auxiliary energy source to the already developed FSW model will be studied. This will provide an approach to optimise the process parameters of steel FSW while reducing the reaction forces on the FSW tool. Therefore, the increase in the traverse speed will improve the productivity in the potential industrial applications.

1.3. Structure of the thesis

This thesis is divided into five further chapters. Experimental advances and the numerical development of steel FSW is given in Chapter 2. The previous associated research is discussed with regards to the material models for FSW simulations and application of auxiliary energy in FSW.

Chapter 3 provides an insight on the numerical modelling techniques used for the simulation of FSW. It discusses different solution methods for partial differential equations, and various domain discretisation techniques such as Lagrangian, Eulerian, Arbitrary Lagrangian and Eulerian (ALE) and CEL approaches. Mathematical models of fully coupled thermal structural elements, heat transfer and metal mechanics are presented. Two major approaches, Implicit and Explicit analyses, for the finite element formulation are then presented.

Based on the numerical approaches in Chapter 3, the detailed development of an FSW thermomechanical model featuring shipbuilding steel grade DH36 workpiece is discussed in Chapter 4 with actual high temperature dependant material properties and simulation of tool/workpiece as solid bodies. These aspects have not been previously implemented for the numerical simulation of steel FSW, and have allowed the present models to produce more realistic results on this solid state joining process. Details of various aspects associated with the advanced finite element model such as material modelling, boundary conditions, contact formulation, meshing techniques and numerous other analysis options are presented. Both structural and thermal conditions have been solved in parallel so that the effect of one parameter on the other can be studied. Therefore, a better analysis is achieved by the examination of the tool's impact on the process. The simulation results including temperature distribution, plastic strain, flash generation, material movement and reaction forces are presented to investigate the coupled thermomechanical behaviour of FSW.

To reduce the reaction forces on the tool during FSW, the inclusion of an auxiliary energy source to the predefined model from Chapter 4 is discussed in Chapter 5. The use of the laser power as an assisted heat source to the FSW model is thoroughly explained. Real time data of the laser source is applied to provide a realistic comparison between the laser assisted and simple FSW. Diverse sets of process parameters are modelled to visualise the effect of assisted heating on the process. The distance between the heat source and the tool during the traverse stage is optimised by simulating the laser assisted FSW (LAFSW) models. Comparison of models with and without the heat source through the reaction forces on the tool, temperature distribution, plastic strain and material flow in the workpiece is discussed. Finally, optimised process parameters are achieved for LAFSW so that defect free welds could be obtained at maximum traverse speed.

The thesis concludes with a critical assessment of the progress achieved and an outlook in Chapter 6. The significant outcomes of this work have been published in the journal papers listed in Appendix 1.

1.4. References

[1.1] Wayne M. Thomas, Nicholas ED, Needham JC, Murch MG, Temple-Smith P, Dawes CJ. Friction welding, 1991.

[1.2] Toumpis A, Galloway A, Cater S, McPherson N. Development of a process envelope for friction stir welding of DH36 steel - A step change. Mater Des 2014;62:64–75. doi:10.1016/j.matdes.2014.04.066.

[1.3] Çam G. Friction stir welded structural materials: beyond Al-alloys. Int Mater Rev 2011;56:1–48. doi:10.1179/095066010X12777205875750.

[1.4] Shi L, Wu CS, Padhy GK, Gao S. Numerical simulation of ultrasonic field and its acoustoplastic influence on friction stir welding. Mater Des 2016;104:102–15. doi:10.1016/j.matdes.2016.05.001.

[1.5] Lienert TJ, Stellwag WL, JR, Grimmett BB, Warke RW. Friction Stir Welding Studies on Mild Steel. Weld J 2003;82:1–9.

[1.6] He X, Gu F, Ball A. A review of numerical analysis of friction stir welding. Prog Mater Sci 2014;65:1–66. doi:10.1016/j.pmatsci.2014.03.003.

[1.7] Chen T. Process parameters study on FSW joint of dissimilar metals for aluminum-steel. J Mater Sci 2009;44:2573–80. doi:10.1007/s10853-009-3336-8.

[1.8] Seighalani KR, Givi MKB, Nasiri AM, Bahemmat P. Investigations on the effects of the tool material, geometry, and tilt angle on friction stir welding of pure titanium. J Mater Eng Perform 2010;19:955–62. doi:10.1007/s11665-009-9582-8.

[1.9] Potluri H, Jones JJ, Mears L. Comparison of Electrically-Assisted and Conventional Friction Stir Welding Processes by Feed Force and Torque. ASME 2013 Int. Manuf. Sci. Eng. Conf., Madison: 2013, p. 10. doi:10.1115/MSEC2013-1192.

[1.10] Rai R, De A, Bhadeshia HKDH, DebRoy T. Review: friction stir welding tools. Sci Technol Weld Join 2011;16:325–42. doi:10.1179/1362171811Y.0000000023.

[1.11] Zhang YN, Cao X, Larose S, Wanjara P. Review of tools for friction stir welding and processing. Can Metall Q 2012;51:250–61. doi:10.1179/1879139512Y.0000000015.

[1.12] Salih OS, Ou H, Sun W, McCartney DG. A review of friction stir welding of aluminium matrix composites. Mater Des 2015;86:61–71. doi:10.1016/j.matdes.2015.07.071.

[1.13] Dubourg L, Dacheux P. Design and properties of FSW tools : a literature review. 6th Int. Symp. Frict. Stir Weld., Saint-Sauveur: 2006, p. 16.

[1.14] Arif A, Abhishek, Pandey KN. Thermo-mechanical Modeling for Residual Stresses of Friction Stir Welding of Dissimilar Alloys. Int J Eng Sci Technol 2013;5:1195–204.

[1.15] Rowe CED, Wayne T. Advances in Tooling Materials for Friction stir welding. TWI Cedar Met Ltd 2006:1–11.

[1.16] Almoussawi M. A Mathematical and Experimental Analysis of Friction Stir Welding of Steel. Sheffield Hallam University, 2018.

[1.17] Toumpis A, Galloway A, Cater S, Micallef D, Camilleri D, Poletz N, et al. Advances in friction stir welding of steel – project HILDA. Transp. Res. Arena, Paris, France: 2014.

[1.18] Buffa G, Hua J, Shivpuri R, Fratini L. Design of the friction stir welding tool using the continuum based FEM model. Mater Sci Eng A 2006;419:381–8. doi:10.1016/j.msea.2005.09.041.

[1.19] Toumpis AI, Galloway AM, Arbaoui L, Poletz N. Thermomechanical deformation behaviour of DH36 steel during friction stir welding by experimental validation and modelling. Sci Technol Weld Join 2014;19:653–63. doi:10.1179/1362171814Y.0000000239.

[1.20] Busu N, Jaffarullah MS, Low CY, Shaari MSB, Armansyah, Jaffar A. A Review of Force Control Techniques in Friction Stir Process. Procedia Comput Sci 2015;76:528–33. doi:10.1016/j.procs.2015.12.331.

[1.21] Kumar K, Kailas S V. The role of friction stir welding tool on material flow and weld formation. Mater Sci Eng A 2008;485:367–74. doi:10.1016/j.msea.2007.08.013.

[1.22] Sato YS, Nelson TW, Sterling CJ, Steel RJ, Pettersson CO. Microstructure and mechanical properties of friction stir welded SAF 2507 super duplex stainless steel. Mater Sci Eng A 2005;397:376–84. doi:10.1016/j.msea.2005.02.054.

[1.23] Chen YC, Nakata K. Effect of tool geometry on microstructure and mechanical properties of friction stir lap welded magnesium alloy and steel. Mater Des 2009;30:3913–9. doi:10.1016/j.matdes.2009.03.007.

[1.24] Surovek AE. Friction Stir Welding of Steel Connections. 7th Int. Work. Connect. Steel Struct., Timisoara, Romania: 2012.

[1.25] Threadgill PL. Terminology in friction stir welding. Sci Technol Weld Join 2007;12:357–60. doi:10.1179/174329307X197629.

[1.26] Toumpis A, Galloway A, Cater S, Molter L. A techno-economic evaluation of friction stir welding of DH36 steel. 10th Int. Symp. Frict. Stir Weld., Beijing: 2014.

[1.27] Toumpis A, Galloway A, Cater SR, Burling P, Stanhope C. Friction stir welding of steel for marine applications. 33rd Int. Conf. Ocean. Offshore Arct. Eng. OMAE 2014, California: 2014.

[1.28] Simar A, Bréchet Y, De Meester B, Denquin A, Gallais C, Pardoen T. Integrated modeling of friction stir welding of 6xxx series Al alloys: Process, microstructure and properties. Prog Mater Sci 2012;57:95–183. doi:10.1016/j.pmatsci.2011.05.003.

[1.29] Nandan R, Debroy T, Bhadeshia HKDH. Recent Advances in Friction Stir Welding – Process, Weldment Structure and Properties. Prog Mater Sci 2008;53:980–1023. doi:10.1016/j.pmatsci.2008.05.001.

[1.30] Arora A, De A, Debroy T. Toward optimum friction stir welding tool shoulder diameter. Scr Mater 2011;64:9–12. doi:10.1016/j.scriptamat.2010.08.052.

[1.31] Padmanaban G, Balasubramanian V. Selection of FSW tool pin profile, shoulder diameter and material for joining AZ31B magnesium alloy - An experimental approach. Mater Des 2009;30:2647–56. doi:10.1016/j.matdes.2008.10.021.

[1.32] Aissani M, Gachi S, Boubenider F, Benkedda Y. Design and Optimization of

Friction Stir Welding Tool. Mater Manuf Process 2010;25:1199–205. doi:10.1080/10426910903536733.

[1.33] Lin S-B, Zhao Y-H, He Z-Q, Wu L. Modeling of friction stir welding process for tools design. Front Mater Sci 2011;5:236–45. doi:10.1007/s11706-011-0128-2.

[1.34] Nandan R, Roy GG, Lienert TJ, DebRoy T. Numerical modelling of 3D plastic flow and heat transfer during friction stir welding of stainless steel. Sci Technol Weld Join 2006;11:526–37. doi:10.1179/174329306X107692.

[1.35] Chao YJ, Qi X, Tang W. Heat Transfer in Friction Stir Welding—Experimental and Numerical Studies. J Manuf Sci Eng 2003;125:138. doi:10.1115/1.1537741.

[1.36] Zhang Q, Mahfouf M, Panoutsos G, Beamish K, Norris I. Knowledge discovery for friction stir welding via data driven approaches. Part 1 - correlation analyses of internal process variables and weld quality. Sci Technol Weld Join 2012;17:672–80. doi:10.1179/1362171812Y.0000000061.

[1.37] Gibson BT, Lammlein DH, Prater TJ, Longhurst WR, Cox CD, Ballun MC, et al. Friction stir welding: Process, automation, and control. J Manuf Process 2014;16:56–73. doi:10.1016/j.jmapro.2013.04.002.

[1.38] Padhy GK, Wu CS, Gao S. Auxiliary energy assisted friction stir welding – status review. Sci Technol Weld Join 2015;20:631–49. doi:10.1179/1362171815Y.0000000048.

[1.39] Sorensen CD, Stahl AL. Experimental measurements of load distributions on friction stir weld pin tools. Metall Mater Trans B Process Metall Mater Process Sci 2007;38:451–9. doi:10.1007/s11663-007-9041-6.

[1.40] Mishra RS, Ma ZY. Friction stir welding and processing. Mater Sci Eng R Reports 2005;50:1–78. doi:10.1016/j.mser.2005.07.001.

[1.41] Lee C-Y, Choi D-H, Yeon Y-M, Jung S-B. Dissimilar friction stir spot welding of low carbon steel and Al–Mg alloy by formation of IMCs. Sci Technol Weld Join 2009;14:216–20. doi:10.1179/136217109X400439.

[1.42] Chen TP, Lin W-B. Optimal FSW process parameters for interface and welded zone toughness of dissimilar aluminium–steel joint. Sci Technol Weld Join 2010;15:279–85. doi:10.1179/136217109X12518083193711.

[1.43] Cederqvist L. Friction Stir Welding of Copper Canisters Using Power and Temperature Control. Lund University, 2011.

[1.44] Hossfeld M. High speed friction stir welding of thick copper plates. Int. Conf. Frict. Stir Weld. Process. FSWP, Ordizia: 2015, p. 23–7.

[1.45] Sato YS, Arkom P, Kokawa H, Nelson TW, Steel RJ. Effect of microstructure on properties of friction stir welded Inconel Alloy 600. Mater Sci Eng A 2008;477:250–8. doi:10.1016/j.msea.2007.07.002.

[1.46] Megastir. https://megastir.com/tools/.

[1.47] Sinclair PC, Longhurst WR, Cox CD, Lammlein DH, Strauss AM, Cook GE. Heated friction stir welding: An experimental and theoretical investigation into how preheating influences process forces. Mater Manuf Process 2010;25:1283–91. doi:10.1080/10426914.2010.496122.

[1.48] Miles MP, Nelson TW, Steel R, Olsen E, Gallagher M. Effect of friction stir welding conditions on properties and microstructures of high strength automotive steel. Sci Technol Weld Join 2009;14:228–32. doi:10.1179/136217108X388633.

[1.49] Zhang Y, Sato YS, Kokawa H, Park SHC, Hirano S. Stir zone microstructure of commercial purity titanium friction stir welded using pcBN tool. Mater Sci Eng A 2008;488:25–30. doi:10.1016/j.msea.2007.10.062.

[1.50] Sorensen CD, Nelson TW. Friction stir welding of ferrous and nickel alloys. Frict. stir Weld. Process., ASM International; 2007, p. 111–21.

[1.51] Li H, Liu D. Simplified Thermo-Mechanical Modeling of Friction Stir Welding with a Sequential FE Method. Int J Model Optim 2014;4:410–6. doi:10.7763/IJMO.2014.V4.409.

[1.52] Yin YH, Sun N, North TH, Hu SS. Influence of tool design on mechanical properties of AZ31 friction stir spot welds. Sci Technol Weld Join 2010;15:81–6. doi:10.1179/136217109X12489665059384.

[1.53] Ahmad B, Galloway A, Toumpis A. Advanced numerical modelling of friction stir welded low alloy steel. J Manuf Process 2018;34:625–36. doi:10.1016/j.jmapro.2018.07.003.

[1.54] Polezhayeva H, Toumpis AI, Galloway AM, Molter L, Ahmad B, Fitzpatrick ME. Fatigue performance of friction stir welded marine grade steel. Int J Fatigue 2015;81:162–70. doi:10.1016/j.ijfatigue.2015.08.003.

[1.55] Ulysse P. Three-dimensional modeling of the friction stir-welding process. Int J Mach Tools Manuf 2002;42:1549–57. doi:10.1016/S0890-6955(02)00114-1.

[1.56] Álvarez AI, Cid V, Pena G, Sotelo J, Verdera D. Assisted friction stir welding of carbon steel: Use of induction and laser as preheating techniques. Frict Stir Weld Process VII 2016:117–26. doi:10.1007/978-3-319-48108-1_13.

2. Literature review

This chapter provides a detailed review of the experimental and numerical modelling research performed on the friction stir welding (FSW) technology for steel alloys. The major focus is on the numerical simulation of the FSW process including various modelling techniques and their limitations for steel alloys. The issues related to increasing the traverse speed and the life of the tool will lead to the introduction of the auxiliary energy to the FSW process. Based on the potential advantages of the auxiliary energy, developments in the laser assisted FSW will be discussed.

2.1. Experimental advances in the FSW of steel

FSW of aluminium and other low melting temperature alloys has been widely accepted by industry, as discussed in Chapter 1. However, in the case of steel and other high melting temperature alloys, FSW has yet to be fully adopted by industry as an economical joining process. It has been demonstrated that steel FSW provides a good quality weld with even higher strength in HAZ and TMAZ when compared to other welding techniques [2.1-2.4]. Despite this, the FSW tooling cost is seen as a commercial barrier to the implementation of FSW for steel fabrication by industry [2.2,2.5].

Since a publication in 1999 by Thomas et al. [2.6], the potential for steel FSW is still being explored. Due to the gradual wear of the tool in FSW [2.7-2.10], it becomes difficult to generate identical results by using similar process parameters. In an early development of the FSW of steel AISI 1018, a maximum traverse speed of 101.6 mm/min was obtained by Lienert et al. [2.11]. A tool shoulder of diameter 19 mm and a probe length of 6.22 mm was used, which was made of molybdenum and tungsten based alloys [2.11]. It was reported that the wear of the tool's probe had no noteworthy effect on the tensile strength of the welds [2.11]. The maximum wear on the tool was experienced during the plunge stage [2.11]. However, no work was performed on the influence of process parameters or the tool geometry. In addition, the traverse speed of ~ 100 mm/min is considered too low for steel FSW application in industry as compared to conventional fusion welding methods. To increase the traverse speed, Gosh et al. [2.12] proposed an optimal process parameters window for the application of FSW for high strength M190 steel. A CY16 Carbide tool of shoulder diameter 10 mm and probe length 1.2 mm was used to weld the steel with rotational speeds ranging from 600 to 1200 rpm [2.12]. The effect of the cooling rates was analysed on the microstructural changes in the weld regions. A process window of 101 to 203 mm/min with 1000 rpm was preferred for FS lap welding of the M190 steel [2.12]. The plunge depth was 1.85 mm with a tool tilt angle of 2.5^o but there was no discussion on the tool geometry and wear for the presented process parameters. Therefore, the provided process parameters cannot be considered as an optimal process window for steel FSW.

The effects of the tool's traverse and rotational speed on steel FSW were reported by Bilgin et al. [2.13]. The tool was made of tungsten carbide and the shoulder diameter was 20 mm with a triangular probe of length 2.5 mm [2.13]. A maximum traverse speed of 200 mm/min was applied to weld the AISI 430 steel with a tool rotational speed of 1120 rpm [2.13]. The tool temperature had a direct and inverse relation with the tool rotational speed and traverse speed, respectively [2.13]. The maximum traverse speed applied in this research [2.13] is still not commercially attractive compared to conventional fusion welding speeds. Moreover, the influence of the triangular probe on FSW has not been discussed with reference to using a simple cylindrical probe.

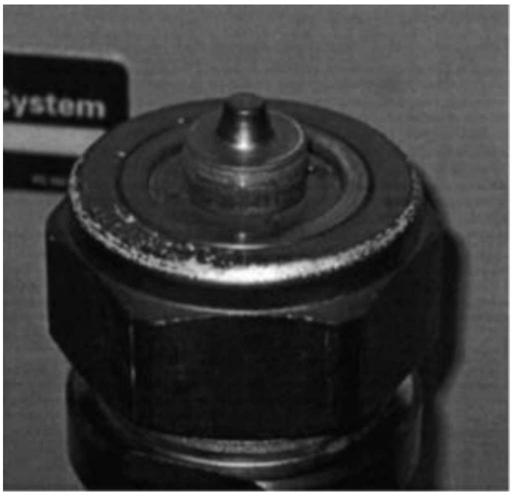

Figure 2.1: Tungsten alloy tool used by Reynolds et al. [2.14].

Reynolds et al. [2.14] examined the microstructural properties of single pass friction stir (FS) welds in a 6.4 mm thick low alloy DH36 steel plate. A tungsten alloy tool of shoulder diameter 19 mm and probe length 5.6 mm with a slight tapering was used for the experiments [2.14], as shown in Figure 2.1. A maximum traverse speed of 456 mm/min was successfully obtained with the reduced specific weld energy (energy input per unit length of weld) [2.14]. However, wear on the tool was observed after several metres of welding along with material loss at the root of the weld. This demonstrates that the weld's quality is compromised by repeated use of the FSW tool.

Further work on DH36 steel has been reported by McPherson et al. [2.15] who examined three different thicknesses of DH36 steel (4, 6 and 8 mm) that were welded by FSW. To evaluate the potential in the shipbuilding industry, the FSW process was compared with the submerged arc welding (SAW) process [2.15]. FSW was found to be superior to SAW in terms of distortion and the fatigue properties of the welded plates [2.15]. Since no information regarding the material and the geometry of the FSW tool has been provided, the comparison of both processes requires further research. However, similar results for DH36 and EH36 steel have been reported by Cater et al. [2.5] who used a WRe-pcBN based tool with stepped spiral probe and a scrolled shoulder. An argon shielding gas was used to protect the tool from the atmosphere. It was concluded that FSW generated reduced angular and longitudinal distortion than SAW on the same grade of steel [2.5]. Moreover, the FSW welds were at least as strong as the parent material [2.5].

One of the extensive research studies on DH36 steel has been reported by Toumpis et al. [2.2-2.4,2.16-2.20]. A WRe-pcBN FSW tool with a convex scrolled shoulder of diameter 25 mm and threaded pin of length 5.7 mm was used for steel FSW [2.2,2.4,2.16-2.18,2.20,2.21]. A general view of the FSW machine and experimental setup used by Toumpis et al. [2.3] is shown in Figure 2.2. The tool traverse speeds were successfully increased from 100 mm/min to 500 mm/min for steel FSW [2.2,2.16-2.18]. Moreover, the FSW process was found to be very sensitive to the change in the tool's rotational speed at increased traverse speeds [2.4]. In other studies [2.3,2.18], microstructural changes due to FSW were examined and compared using various process parameters. Different sets of process parameters were considered for steel FSW, categorised as slow, intermediate and fast speeds [2.3,2.18]. It was observed that FSW generated a very complex metallurgical system in which the slow and fast traverse speeds produced very refined and heterogeneous microstructures, respectively [2.3,2.18]. When a stress (up to 90 percent of the material's yield strength) was applied on the steel FS welds, an outstanding fatigue life was observed, with more than 10^5 cycles to fracture [2.16-2.18]. The results by Toumpis et al. [2.2-2.4] demonstrate that FSW will only become economically viable by increasing the tool life or decreasing the tool cost. Therefore, a significant research on extending the life of the tool and achieving higher traverse speeds is required for steel FSW to become industrially attractive.

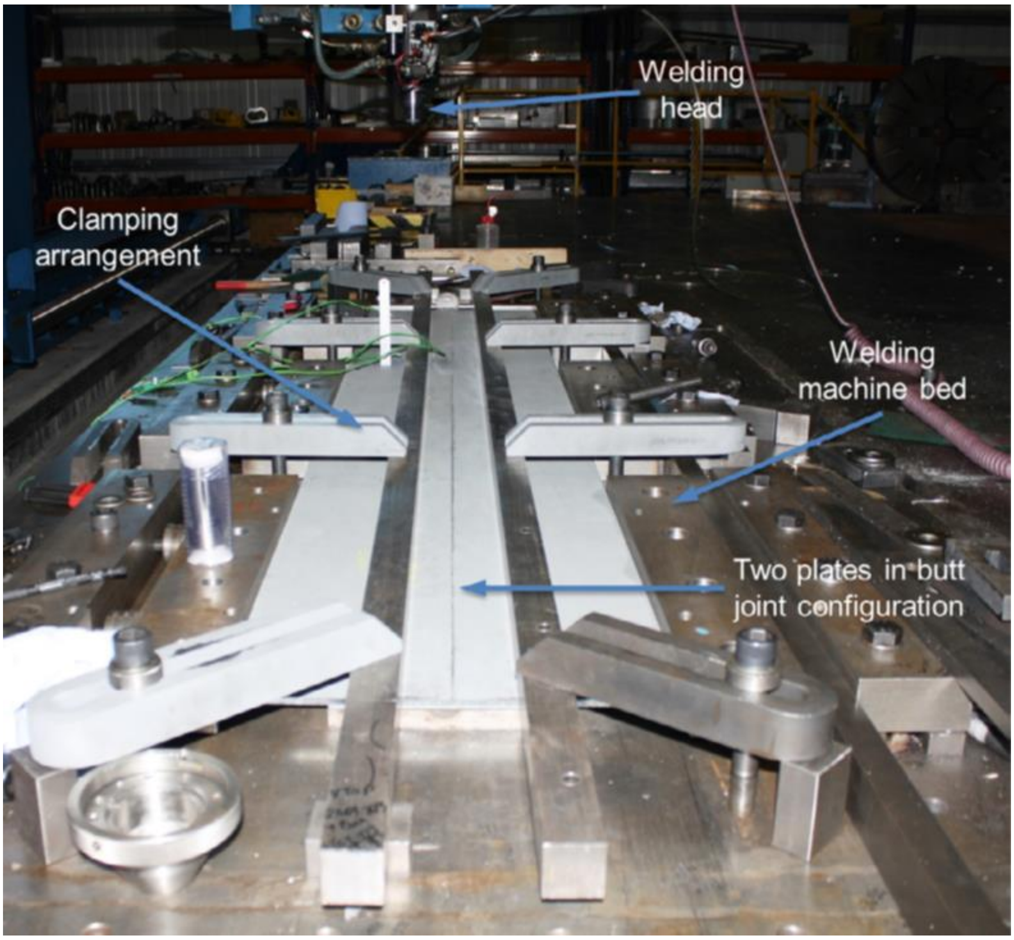

Figure 2.2: FSW experimental setup arranged by Toumpis et al. [2.3].

2.2. Numerical Modelling of the FSW process

2.2.1. Motivation for FSW simulation

The majority of the published research on steel FSW show the potential applicability of the process to produce efficient and better quality welds as compared to fusion welding processes. However, the tooling cost and limited life are still a problem for the widespread application of the process [2.2,2.22]. Since the equipment used for FSW is expensive [2.4,2.23] and the FSW thermomechanical features are difficult to calculate experimentally [2.24], this has led to numerically simulate the whole FSW for exploring techniques to increase the tool’s life and the traverse speed.

Numerical simulation is a cost-effective means of investigating and predicting different physical phenomena during FSW, which are not readily possible through the experimental procedures [2.22,2.25]. From a modelling perspective, it is important to capture the numerical results of FSW as close to the experimentally generated data as possible such as the temperature gradient, weld surface features and material flow in the workpiece. This allows an evaluation of diverse factors, for instance tool geometry and process parameters [2.22,2.26]. Numerical modelling should contain as many degrees of freedom in this regard as possible so that unnecessary constraints may be avoided to visually reproduce the actual process. This concerns in particular the modelling of all physical bodies and material properties. In an ideal case, the representation of FSW should therefore be based on the underlying physics itself, since simplified models can lead to partly unrealistic results [2.22,2.27,2.28]. Therefore, in the numerical simulation of steel FSW, both the tool and workpiece should be modelled as solid bodies, to reflect as a standard in the research and development of the process. However, this is currently such a great challenge in a thermomechanical simulation that it has not yet been modelled in any mechanical model for steel FSW. To better understand the FSW process, it is crucial to develop a consistent simulation methodology that can reflect the whole process presented in Chapter 1.

2.2.2. Developments in the numerical modelling of FSW

Publications on the modelling of FSW are not as much as the large number of publications on other topics of FSW [2.24]. Nevertheless, numerous researchers [2.25,2.29-2.51] have considered various types of FSW numerical models, with different approaches, goals and modelling techniques. Existing modelling publications have been reviewed below in terms of the approach to the challenges presented and the degree of fulfilment. Particular attention is paid to the applied mechanical formulations, any modelling restrictions and the material data used in the previous publications. The major focus is on the research based on the three-dimensional thermomechanically coupled models.

2.2.2.1. Thermal modelling

Since the early stage of the advancement of FSW, various thermal models have been developed based on the conventional thermal welding simulations using a virtual heat source [2.29-2.33,2.51]. These thermal simulations could estimate the temperature distributions in the workpiece, which led to evaluate the thermomechanically affected zone (TMAZ) and the heat affected zone (HAZ) profiles. Camilleri et al. [2.29] developed an FSW numerical model for DH36 steel by replacing the solid tool with a heat source. Thermal stresses in the workpiece were calculated, and it was found that the fast welding conditions could result in lower peak temperatures [2.29].

The numerical simulations based on the thermal modelling were beneficial in terms of the required thermal process knowledge, integration of experimental boundary conditions into the numerical model, and therefore initiation of numerical modelling in the early development of FSW. However, the information with regard to the weld joint, process forces and other significant factors cannot be assessed by thermal modelling without the influence of the mechanical phenomena. In addition, the calculations of the temperature profiles often become increasingly inaccurate with increasing temperature gradients due to the virtual heat input. This is the case when the heat input is not dominated by the shoulder or the heat transfer by the convection is higher than the heat transfer by the tool, such as in thick sheet welding or complex tool contouring. Nevertheless, thermal simulations are still used in application-oriented calculations [2.52] or for the isolated consideration of temperature-dependent phenomena [2.51,2.53].

2.2.2.2. Fluid modelling

The strong fluid-mechanical nature of the FSW process and various issues related to the material flow or complex tool geometries led to the numerical implementation of the process as fluid models. Several researchers [2.34-2.38,2.47] developed FSW models using an advanced computational fluid dynamics (CFD) algorithm to carefully observe the material behaviour during the process. A CFD model was developed for the FSW of DH36 steel by Al-Moussawi et al. [2.47], where the material flow in the workpiece was analysed by considering the solid workpiece as a highly viscous fluid body. It was concluded that for the slow (100 mm/min, 160 rpm) and medium (250 mm/min, 300 rpm) welding parameters, the maximum temperature was located under the tool shoulder, whereas for the fast (400 mm/min, 550 rpm) welding parameters, it existed on the workpiece surface just near to the tool shoulder periphery [2.47]. In addition, the minimum temperature was located at the probe tip, and the cooling rate was increased by increasing the traversing speed [2.47]. Since the CFD model cannot be used to simulate the stresses that are typically found in the weld joint, no information regarding the reaction forces on the tool and the workpiece are present in the CFD results. In addition to the rotating tool, the workpiece is provided with a linear translation in the discussed CFD model, whereas both the rotation and the translation is applied on the FSW tool in reality.

The cited CFD models use the typical fluid dynamics Eulerian formulation using the Navier-Stokes equations [2.54]. This allows a detailed description of the material flow around the tool. However, no separation of the material is possible in the models due to the forced boundary conditions. This prevents the visualisation of any void formation and other welding defects due to FSW. Nevertheless, this helps in allowing the user to model complex tool geometries without major numerical problems as the mesh moves along with the tool, as discussed by Colegrove et al. [2.38]. Since the tool is always considered as already plunged in these models, transient processes such as the plunge of the tool can hardly be depicted. As a result, the focus of the CFD simulations [2.34-2.38,2.47] inevitably lies on the traverse stage of the welding, which means that the material and process histories of other stages cannot be taken into account. This further restricts the replication of the physical phenomena of the FSW process, such as the plunge force [2.55]. Due to the CFD approach for instance, it is not possible to model FSW of two separate workpieces since they will be treated as viscous fluid bodies. All CFD models [2.34-2.38,2.47] therefore represent bead-on-plate welds along with the formation of weld joint surfaces. Finally, it should be mentioned that it is generally possible to take into account temperature-dependent material parameters such as density, specific heat or thermal conductivity in the context of CFD modelling, but it is currently rarely implemented [2.53].

2.2.2.3. Mechanical modelling

Xu et al. [2.48] simulated one of the first structural models of FSW. The presented model considers the two-dimensional material flow in an isolated XY plane of the weld, and is similar to the previously discussed CFD models due to the lack of void formation and visualisation of any weld defects. In the numerical modelling of FSW, only the traverse stage of the FSW process is taken into account, and the temperature values and boundary conditions are derived from the experimental data. For this reason, the model does not consider heat generation due to the friction and plastic deformation. Analogous mechanical models have been represented in other published works as well [2.39,2.41]. Modelling complex tool geometry features requires very fine elements to avoid any mesh distortions and convergence issues in the model. Consequently, the computational cost increases as well [2.26]. Similar to the CFD modelling described above, the contact between the tool and the workpiece is forced in the mechanical modelling, which is why any weld defect formation cannot be represented. In addition, it has become clear that high strain and strain rates, frictional contact, and other non-linear properties of the FSW process posed significant problems with the application of such conventional modelling techniques, mentioned above.

2.2.2.4. Thermomechanically coupled modelling

Although isolated thermal, fluid and mechanical modelling may explain some observed aspects of the FSW process, a holistic approach requires a fully coupled simulation methodology that includes the entire process with the transition between all different stages. This concerns, in particular, the process history during the plunge stage until the tool starts to traverse in the welding direction. Without the consideration of all stages, the simulation loses the physical effect during the process that can influence the later simulation stages, such as void formation. Since many interactions in FSW have yet not been sufficiently understood, only such numerical simplifications should be considered which are critical to the model. Various researchers simplify the numerical model to such an extent that the numerical proficiency of the model leads to deficient results [2.22,2.28]. Many thermomechanically coupled features such as temperature dependent material deformation, heat generation due to the frictional contact and potential defects in the workpiece are often overlooked by such numerical approaches. To date, two major coupled modelling approaches are present for the numerical modelling of FSW; Arbitrary Lagrangian Eulerian (ALE) approach and Coupled Eulerian Lagrangian (CEL) approach. These are discussed below in detail.

Arbitrary Lagrangian Eulerian approach

The Arbitrary Lagrangian Eulerian (ALE) approach has been used to make a fully developed FSW model with realistic boundary conditions, in which the viscoplastic flow and the heat transfer effects are modelled simultaneously in the system to predict the temperature and the stress distributions [2.27]. Since a publication by Schmidt et al. [2.42] in 2005, several FSW numerical models have been developed using the ALE approach [2.24,2.27,2.43,2.44,2.56]. Schmidt et al. [2.42] developed a local process model that represented the joining zone with adjacent surroundings. Both plates in the model were represented as one continuous workpiece [2.42]. The model was also initially provided with a hole that receives the tool during the simulation, which completely penetrates the workpiece. By these measures, strong mesh distortions in the model were avoided during the plunge stage [2.42]. However, similar to the CFD models, the plunge process could only be simulated to a limited extent, as the material flow under the welding tool could not be visualised. The FSW modelling by the ALE approach was thus able to provide the material deformation and temperature distributions as well as the velocity fields of the process.

Even with the use of the ALE approach, numerical modelling of FSW is very difficult due to the large distortions of the mesh [2.42]. This limits the modelling by the ALE approach mainly for the plunge stage of FSW or friction stir spot welding [2.43,2.57]. An exception is the publication of Guerdoux et al. [2.44], which uses an adaptive remeshing algorithm during the simulation to handle this problem. The temperatures sometimes reach higher values as compared to the respective experimental results [2.42,2.58]. It is worth noting that only aluminium FSW has been numerically modelled using the ALE approach.

Coupled Eulerian Lagrangian approach

When it comes to solving large displacement problems, a relatively new modelling approach named Coupled Eulerian Lagrangian (CEL) has demonstrated very promising results as compared to other simulation techniques [2.22,2.59]. As its name suggests, it principally includes two domains, Eulerian and Lagrangian. The Eulerian domain is calculated by spatial time derivatives while material time derivatives are used for the Lagrangian domain [2.60]. In the spatial time derivative, the motion of a body is represented by focussing on a fixed location of space while the body displaces as the time passes [2.61]. On the other side, the material time derivative is used for modelling solid bodies with various physical properties, and is based on the movement of the individual particles of the body through space and time [2.61]. Both sets of equations are related together, and are then calculated simultaneously. Stiffer bodies in the model are considered as Lagrangian elements while the bodies undertaking large deformations are discretised with Eulerian elements [2.60]. Initially, a part of the Eulerian domain is typically filled with material properties, while the rest of it is left empty and often regarded as a section referred to as a “void” [2.59]. This allows elements of the material to be displaced from their initial position into the “void” section if required.

Recently, the CEL approach has been used to successfully model FSW of aluminium with minimum assumptions (solid tool instead of virtual heat source and solid workpiece instead of viscous fluid body) in order to visualise more realistic results [2.62-2.66]. The only study involving the modelling of steel FSW using the CEL approach has been presented by Ahmad et al. [2.22]. Ahmad et al. [2.22] used the formulation of the CEL approach contained in Abaqus/Explicit to simulate all stages of FSW for structural steel DH36. The model consisted of a Lagrangian tool and an Eulerian workpiece. Although the CEL approach enables welding of two separate workpieces, single workpiece was used in the research to minimise the computational cost. The results were compared with previously published experimental investigations of temperature distributions, plastic strains and surface flash [2.22]. To date, the CEL approach appears to be the most appropriate modelling technique to simulate the FSW process, effectively.

2.2.3. Material data

In numerical modelling, appropriate material modelling is required for the accurate representation of FSW. This requires a characterisation that should include all the relevant properties of the material such as density, specific heat, coefficient of thermal expansion, thermal conductivity, yield stress, strain and strain rate. In both ALE and CEL approaches, Johnson Cook's (JC) material properties of aluminium have been used in the literature to model FSW [2.42,2.44,2.62,2.66].

The JC material model has shown remarkable results in machining processes for both low and high melting temperature alloys [2.67-2.70]. JC model calculates several constants for monitoring the material's behaviour. However, since FSW involves high strains and strain rates [2.71,2.72], the JC material properties predicts inaccurate strains and strain rates at high temperatures [2.73,2.74]. Moreover, when using the JC model, the welding process is initiated after the material temperature is raised to a theoretically calculated JC melting temperature that is different from the actual melting temperature of the material. For the case of aluminium, the JC model yields approximately realistic results as the JC melting temperature for aluminium lies in the range of 75-85% of its actual melting temperature [2.75]. This cannot be achieved in steel as the JC model gives an inaccurate melting temperature value (~1300°C – 1400°C) which is unrealistic since steel FSW can occur even below 1000°C [2.76].

These can be some of the main reasons that no research has been reported for the numerical modelling of steel FSW using JC material properties.

DH36 material properties have been developed through theoretical methods to simulate FSW [2.29,2.47,2.77,2.78]. The flow stress model, proposed by Sheppard and Wright [2.79], has been applied to identify the materials' deformation behaviour during the process [2.47,2.77]. The thermal properties were adopted through theoretical findings for low carbon manganese steel [2.47,2.77]. In a research by Nandan et al. [2.36], the simplified Hart's model [2.80] was used to calculate various properties of the material. Although, theoretical properties can reflect the behaviour of the material to an extent, it is vital to obtain the rate dependent properties of the material to improve the accuracy of the FSW modelling as this provides a better understanding towards the process.

To assist the numerical accuracy of the FSW models, temperature dependent material properties on a Gleeble 3800 thermomechanical testing system were experimentally generated for DH36 steel by Toumpis et al. [2.4,2.20]. A set of 58 uniaxial hot compression tests were performed for the temperature range between 700ºC and 1100ºC and the strain rate range between 10^{-3} s^{-1} and 10^{2} s^{-1} [2.4,2.20]. This showed that the development of the flow stresses in the material is influenced by the temperature and the rate of deformation [2.20]. It was observed that the flow stresses were increased with decreasing temperature and increasing strain rates [2.20]. The numerical modelling of steel FSW has been improved by the use of the experimentally generated material properties as compared to the previously applied theoretical data [2.20,2.22].

2.3. Auxiliary energy assisted FSW

As discussed in section 1.1.4, welding of high melting temperature alloys such as steel requires tools with even higher melting temperature, high temperature strength and wear resistance properties. During FSW, the tool experiences large stresses and fatigue loading, which lead to reduced life, hence increasing the process cost [2.71]. Moreover, increased traverse speed may cause tool wear, which in turn affects the weld quality resulting in surface and root flaws [2.81]. Recently, the use of auxiliary heat sources in parallel with FSW has proven to be an attractive solution to obtaining the optimised process parameters of FSW along with the reduced reaction forces on the tool [2.82]. The additional heat source softens the material prior to the welding process. This softening has the beneficial effect of reducing the stresses experienced by the tool. Numerous researchers [2.8,2.10,2.83-2.98] have used different types of assisted heat source to analyse the behaviour of the entire process. Following is a list of the notable auxiliary energies used with FSW [2.82]:

1. Electrically assisted FSW (EAFSW)
2. Induction assisted FSW (IAFSW)
3. Ultrasonic energy assisted FSW (UAFSW)
4. Arc assisted FSW (AAFSW)
5. Laser assisted FSW (LAFSW)

In EAFSW, an electric current is passed through the workpieces, which assists in the welding by resistance heating [2.82]. The electric current assists FSW by generating an electroplastic effect along with the Joule heating effect [2.95]. There are two typical setups for configuring the EAFSW, as shown in Figure 2.3 [2.10,2.94]. In the first setup, the electric current is passed through the tool, hence making the heating localised around the weld joint [2.10]. This type of configuration requires an electrically conductive tool and an insulation system between the tool and the FSW setup [2.82], as shown in Figure 2.3 (a). Santos et al. [2.10] carried out experiments on EAFSW of aluminium AA6082-T6 with a customised H13 steel tool. A copper rod was passed through the axis of the tool to constrain the electric current flow [2.10]. It was observed that the electric current increased the viscoplastic material flow, hence improving the mechanical performance of the FSW joints. However, this customisation cannot be easily applied for the steel EAFSW due to the high melting and strength tool materials.

In the other setup, an arrangement can be built for the electric current passing through the workpiece only [2.94], as seen in Figure 2.3 (b). Potluri et al. [2.94] demonstrated the feasibility of using electric heating in the FSW on aluminium. Direct current was passed through the workpiece to generate a temperature rise along with the material softening [2.94]. The traverse force was decreased up to 59% on average as compared to the conventional FSW [2.94]. In a different research [2.95], two dissimilar materials, aluminium alloy AA6061 and steel alloy TRIP 780, were joined together using EAFSW. It was reported that the electroplastic effect dominated the process when a rotational speed of 1200 rpm and offset distance of 1.03 mm were used as compared to 1800 rpm and 1.63 mm, respectively [2.95]. However, increased temperature through high current density can only be obtained in the weld zone by selecting a workpiece that is narrower along the width [2.82].

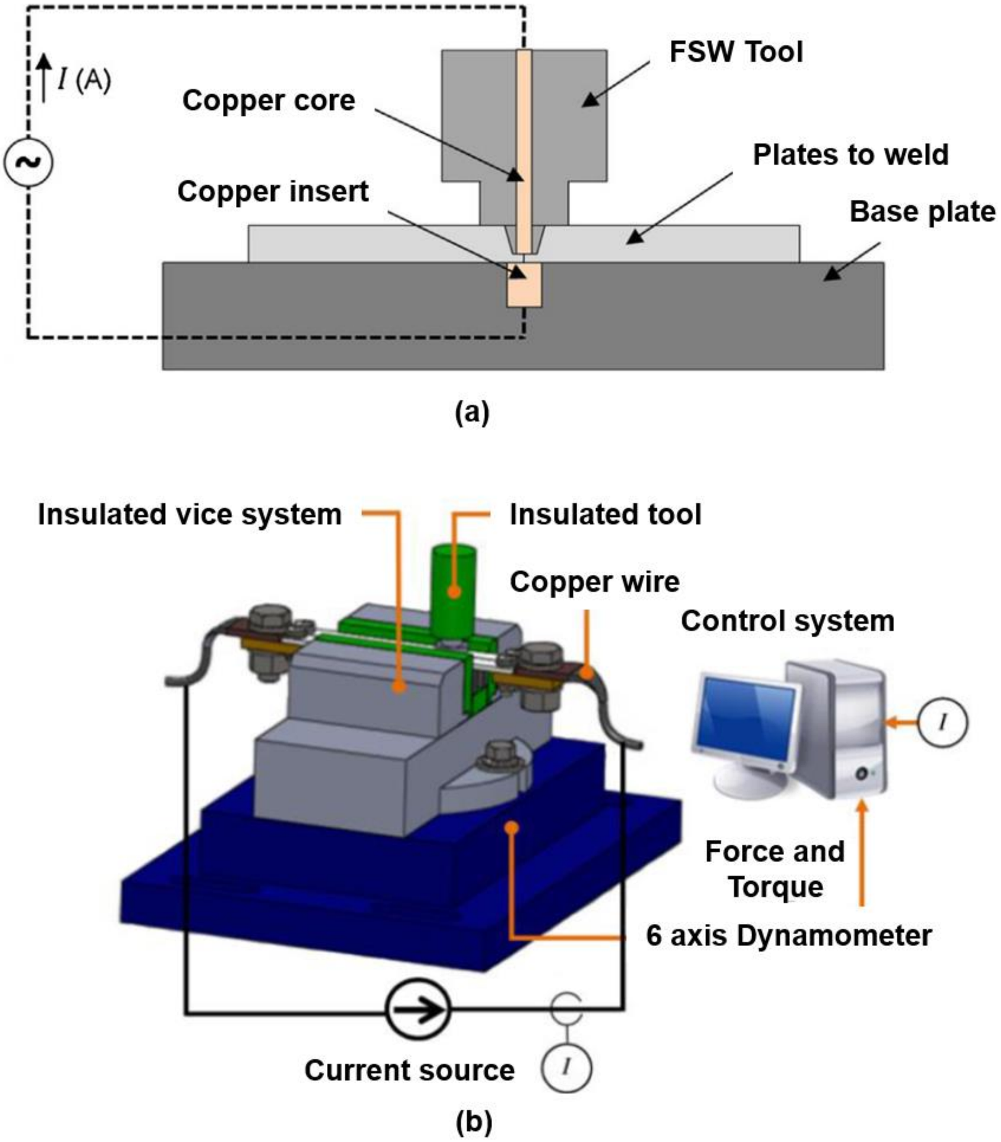

Figure 2.3: Configuration of the electricity in the EAFSW through: (a) the tool [2.10], (b) the workpiece [2.94].

Another type of auxiliary heating is induction heating (IAFSW) in which a varying electromagnetic field is setup around an electrically conductive workpiece, as shown in Figure 2.4. The workpiece is then heated by the electric current flow [2.96]. Alvarez et al. [2.93,2.97] performed IAFSW along with the induction heating of super duplex stainless steel. A pcBN tool with a convex scrolled shoulder of diameter 23.7 mm and a conical stepped spiral probe of length 5 mm was used to weld the steel workpieces

[2.93,2.97]. A decreased plunge force by 30% was observed, which extended the tool life due to the assisted induction heating [2.97].

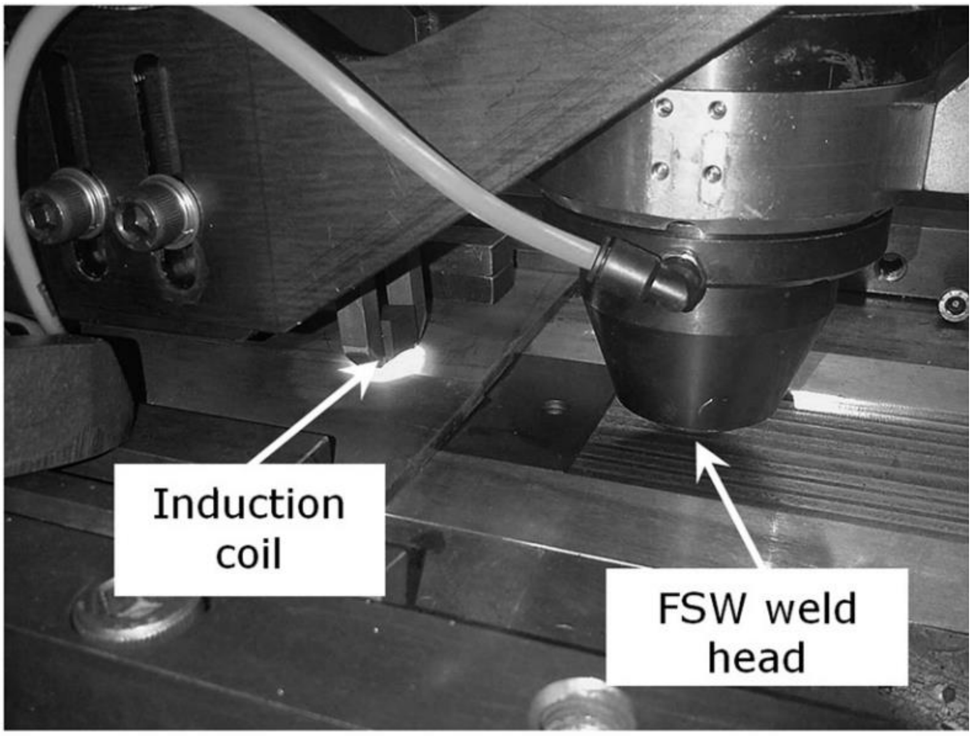

Figure 2.4: IAFSW experimental setup [2.93].

Similarly, up to 43% reduction in the axial force on the tool was achieved in another study when the workpiece was preheated by the induction heating [2.96]. The material flow was also increased by the use of the induction heating [2.96]. Despite its certain advantages, induction heating has many drawbacks for welding steel, such as the control of the current flow, inaccessibility of localised heating and spark generation [2.82].

In UAFSW, an ultrasonic energy source is combined with the FSW setup, as shown in Figure 2.5. The ultrasonic vibrations soften the material and reduce the stresses for additional plastic deformation during FSW. Shi et al. [2.91] investigated FSW on aluminium AA2023-T3 by inputting ultrasonic vibrations to the workpiece. A threaded conical tool probe of length 5.7 mm with a shoulder of diameter 15 mm was used [2.91]. It was found that the tool torque was reduced by about 10% with the preheating and the use of acoustic softening of the material [2.91]. In another research, aluminium AA2024-T4 was welded through the UAFSW such that the vibration tool head ‘Sonotrode’ was placed 20 mm ahead of the FSW tool [2.98]. Due to the ultrasonic vibrations, wider TMAZ and HAZ were achieved than the conventional FSW

[2.98]. The presence of weld defects was reportedly reduced by the use of UAFSW [2.98]. Despite of its potential advantages in welding, no developments have been reported for the UAFSW of steel and high melting temperature materials.

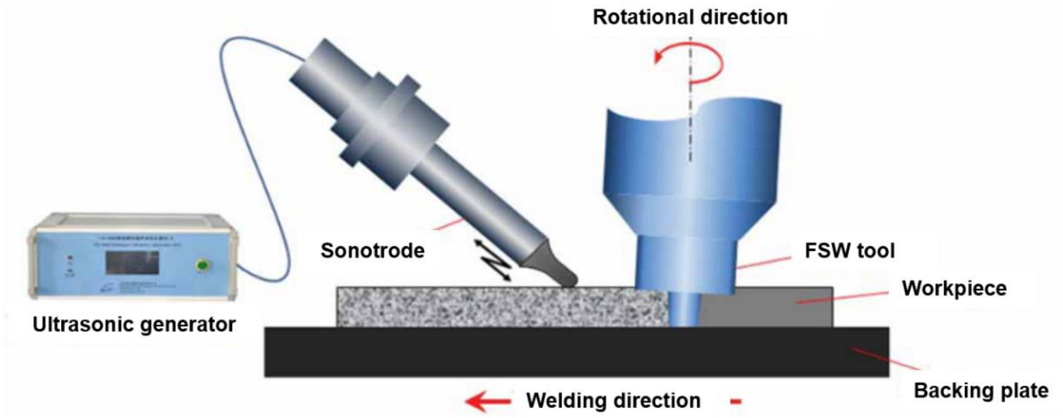

Figure 2.5: UAFSW experimental setup [2.91].

Similar to the fusion welding techniques, an arc source is integrated to the FSW setup to form an AAFSW, as shown in Figure 2.6. This arc can either be a plasma arc [2.83] or a tungsten inert gas (TIG) welding arc [2.84,2.99,2.100]. In the AAFSW of aluminium alloy AA1100 with pure copper, an H13 steel tool of shoulder diameter 18 mm and probe length 5.7 mm was used to weld both metals [2.83]. The application of the plasma arc as preheating in conjunction to FSW increased the tensile strength of the weld joint up to 83% of the aluminium base material [2.83]. In another AAFSW of aluminium AA6061-T6 with steel STS304, a WC-12% CO welding tool with a shoulder of diameter 18 mm and probe length 2.7 mm was implemented along with the TIG welding arc [2.100]. The TIG welding arc influenced the weld joint’s tensile strength up to 93% of the aluminium base material, when joining the aluminium alloy with the steel alloy [2.100]. An AAFSW of magnesium alloy AZ31B and mild steel SS400 was performed by using the similar tool WC-12% CO [2.99] as previous research [2.100]. It was concluded that the TIG welding arc resulted into maximising the weld joint’s tensile strength by 91% of the magnesium alloy base material as compared to the 86% of the magnesium alloy base material with the application of FSW only [2.99]. In all auxiliary assisted FSW, very little research has been reported for steel alloys. One reason for this can be the high cost and unavailablity of the FSW setup for steel and high melting temperature materials.

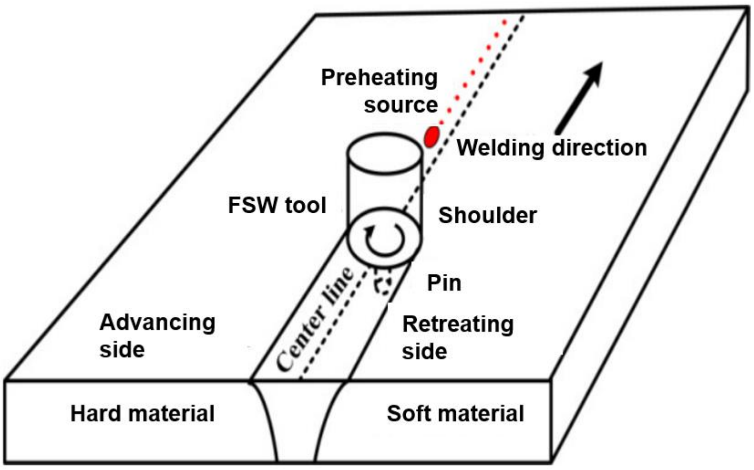

Figure 2.6: AAFSW experimental setup [2.83].

A relatively simpler, yet advanced version of conventional FSW is the laser assisted FSW (LAFSW), which is the most extensive modification applied to optimise the FSW process to date [2.8,2.85-2.87,2.92,2.97]. The experimental setup of LAFSW incorporates the FSW machine accompanied by a laser heat source. Since the maximum stresses on the tool mainly occur in the plunge stage [2.81,2.82], an area of the workpiece, where the tool is to be plunged, is heated by a laser before the plunge stage. This helps in significantly softening the material.

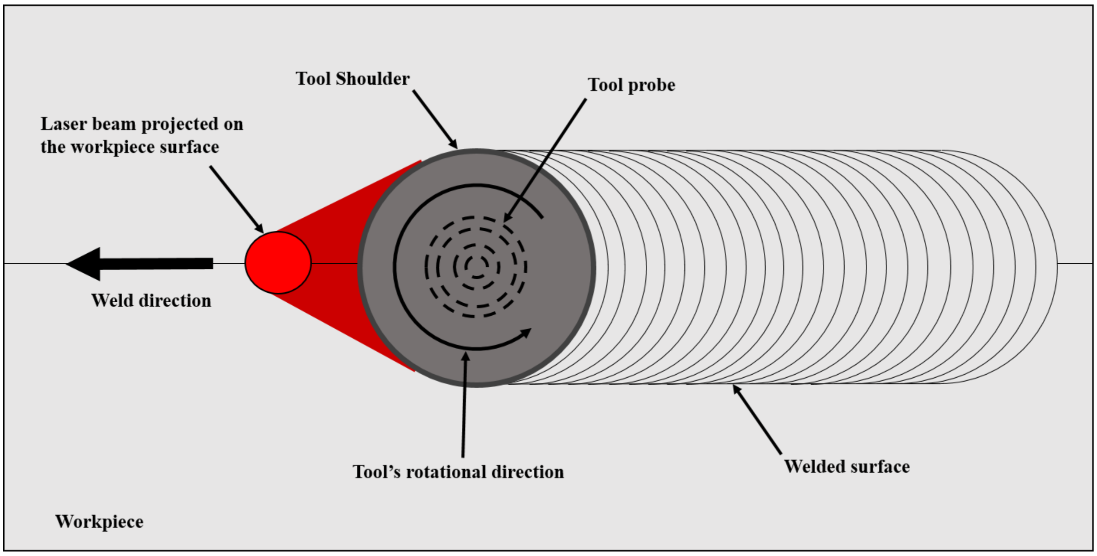

Figure 2.7: Schematic of LAFSW during the traverse stage.

After the tool is in the traverse stage, the laser keeps on preheating the workpiece before the tool passes from that area, as shown in Figure 2.7. This minimises the reaction forces on the tool, which in turn helps to extend the life of the tool [2.82].

2.3.1. Developments on the LAFSW process

Various experimental and modelling studies have been undertaken for the LAFSW of aluminium and other low melting temperature alloys. Casavola et al. [2.92] produced an experimental set up for the LAFSW of 6 mm thick aluminium AA5754 H111 and performed various tests by altering the laser power and distance between the laser and the FSW tool. It was concluded that a closer laser distance with the FSW tool was more suitable to produce a strong preheating effect on the workpiece than a far distance irrespective of the laser power [2.92]. No information has been provided regarding the tool material and geometrical specifications, as well as the influence of the laser heating on the tool itself. To reduce the welding forces on the FSW tool, a study was conducted by the application of laser preheating on friction stir lap welding on aluminium AA2024 [2.88]. The FSW tool was made of steel H13, with a concave shoulder of diameter 10 mm and probe length 1.42 mm [2.88]. It was found that increasing the average weld temperature and the size of the HAZ is not always desirable for the laser heat assistance in FSW due to the increased power consumption [2.88]. However, like the previously discussed thermal models, this numerical model substituted the tool as a moving heat source, accompanied by the laser heating of 150 W power [2.88].

Limited research has been published on the LAFSW of steel and other high melting temperature alloys. To optimise the process parameters, Sun et al. [2.86] successfully obtained an increased traverse speed (up to 800 mm/min) when joining S45C steel plates through LAFSW. The effects of offsetting the heat source from the weld centerline were explored with a WC-based alloy tool, which had a concaved shoulder diameter 15 mm and a probe length of 3.2 mm [2.86]. It was observed that the total heat input can be maximised by focusing the laser beam on the retreating side as compared to the advancing side [2.86]. Similar to Casavola et al. [2.92], Sun et al. [2.86] have not discussed the effects of the increased traverse speed on the FSW tool. In addition, the effect on the tool or the workpiece has not been explored upon increasing the traverse speed more than 800 mm/min.

Alvarez et al. [2.97] welded marine steel plates by using the laser preheating technique. The metal softening due to the laser heating resulted in 33% and 40% reduction in the axial forces on the tool during the plunge and traverse stages, respectively [2.97]. However, these reduced reaction forces were obtained at a maximum traverse speed of 225 mm/min with a rotational speed of 500 rpm. Moreover, there is no information provided regarding the distance between the laser heat source and the FSW tool. Therefore, an additional research must be carried out to confirm the heat source distance and the maximum traverse speed.

Numerical modelling of FSW has enabled to effectively analyse the LAFSW in terms of the cost and reproduction of the results. Daftardar [2.23] developed a thermal model of LAFSW in the CFD software Fluent, based on the FSW experiments by Zhu et al. [2.89]. The study demonstrated that less work is required by the tool when the preheating source is positioned in advance of the FSW tool [2.23]. The heat in the above thermal model was assumed to be generated through the friction between the tool shoulder and the workpiece only. Therefore, this model further requires consideration of welding factors to accurately replicate the experimental results.

To analyse the LAFSW of dissimilar metals, Ti-6Al-4V with stainless steel AISI 304L, Sundqvist et al. [2.90] developed a thermal pseudo mechanical model, which computed heat generation from the material’s yield stress. The forces on the tool shoulder and the probe were calculated through theoretical measures, and applied on the model [2.90]. A laser heat power of 600 W was applied through Nd: YAG-laser beam [2.90]. In the experimental setup, a pre-hole was machined for the FSW tool to reduce any wear during the plunge stage [2.90]. Therefore, the reaction forces on the tool during the plunge stage could not be accurately measured. The laser preheating significantly reduced the forces on the tool probe and shoulder during the traverse stage, and dropped the FSW heat generation [2.90]. These demonstrate LAFSW to be a substantial development for joining steel and other high melting temperature alloys.

2.4. Summary

Significant progress has been made on the implementation of FSW in industry for aluminium alloys. However, FSW of steel and other high temperature alloys is still the subject of considerable research, mainly because of the short life and high cost of the FSW tool. In this context, numerical modelling can provide cost-effective development of steel FSW. To date, none of the published numerical models is able to depict a real solid tool and workpiece geometry in the simulation of steel FSW. Simulation techniques for steel FSW in the literature mainly assume either the rotating tool as a moving heating source or the workpiece as a viscous fluid body.

This review has presented several modelling options for the simulation of steel FSW, specifically focused on thermal, fluid, mechanical and thermomechanically coupled models. In the simple thermal models, the rotating tool is replaced by a moving heat source. Therefore, the thermal models are incapable of producing material flow, process forces on the tool and other informative value with regard to the weld joint.

The predictions from the FSW fluid models show reasonable agreement with the experimentally measured data. Material flow visualisation is possible by using this technique. Boundary conditions play a critical role in determining the temperature profile. However, this modelling approach cannot represent two separate workpieces to be joined together, which prevents the formation of any weld joint surfaces. In addition, visualisation of any void formation and other welding defects is not possible due to no separation of the material during the process.

In the mechanical modelling of steel FSW, temperature values in the model are obtained from the experimental data, which prevents the model to consider heat generation due to the friction and the plastic deformation during the process. Complex tool geometry and material flow patterns around the tool are very difficult to achieve in the mechanical modelling of steel FSW. This is due to the mesh distortion and convergence problems at the complex contact interface in the model. Extremely fine elements would be required to capture the tool features, resulting in an unaffordable computational cost. Similar to the fluid models, defect formation cannot be represented due to the forced boundary conditions in the model.

A fully coupled thermomechanical model is a suitable option to accurately describe the weld formation during FSW with a solid, temperature and strain rate dependent material model. The Arbitrary Lagrangian Eulerian (ALE) approach adequately addresses some of the problems mentioned above. Both solid tool and workpiece assist in visualising the material flow in the workpiece, along with the calculation of process forces on the tool. However, it is not possible to model the mixing of two sheets. The imaging of a detailed weld flash and other weld defects in the workpiece is difficult as well. Even with the use of the ALE approach, the numerical modelling of FSW is very demanding due to the large mesh distortions and computational cost.

The Coupled Eulerian Lagrangian (CEL) approach is by far the most feasible technique to replicate steel FSW. Unlike any previous research in which either the workpiece is assumed as a high viscous body or the tool is modelled as a moving heating source, the CEL approach can be applied to model both the tool and the workpiece as solid bodies. Some of the exceptional traits of the CEL approach include lower mesh distortion, visualisation of the material flow, possibility of joining two separate workpieces together, calculation of process forces on the tool and the workpiece, and display of surface flash and other weld defects. To counter the computational cost, a parallelisation method can produce results more efficiently by utilising several processors, consecutively.

Recently, the use of auxiliary energies has been considered as a means of optimising the FSW process and reducing the forces on the tool. Application of prominent auxiliary energies such as induction heating, ultrasonic vibration, electric heating and laser heating has demonstrated remarkable results in steel FSW. Out of these, laser assisted FSW has been found to be the most extensive modification applied to optimise the FSW process to date. The incorporation of laser heating has increased the traverse speed up to 800 mm/min in steel FSW. In addition, a maximum of 33% and 40% reduction in the tool reaction forces have been observed during the plunge and traverse stages, respectively, in another research. However, optimised process parameters have still not been determined for the steel LAFSW to increase the productivity while minimising the reaction forces on the tool.

Therefore, to build on the state of art, a fully coupled thermomechanical model of FSW featuring low alloy steel will be presented in this thesis. The theoretical background of the whole model will be thoroughly discussed in the subsequent chapter. Later on, all stages of FSW (plunge, dwell and traverse) will be modelled with various process parameters and their results compared with the experimental work on the same grade of steel. Due to the limitations associated with the Johnson Cook model when employed in high melting temperature metals, experimentally generated temperature dependent properties of DH36 steel will be used in the presented models. In addition, laser assisted FSW will be numerically developed and analysed as a viable process amendment to maximise the existing traverse speed for joining steel. An appropriate distance between the heating source and the FSW tool during the traverse stage will be evaluated by modelling various process parameters.

2.5. References

[2.1] Lin S-B, Zhao Y-H, He Z-Q, Wu L. Modeling of friction stir welding process for tools design. Front Mater Sci 2011;5:236–45. doi:10.1007/s11706-011-0128-2.

[2.2] Toumpis A, Galloway A, Cater S, Molter L. A techno-economic evaluation of friction stir welding of DH36 steel. 10th Int. Symp. Frict. Stir Weld., Beijing, China: 2014.

[2.3] Toumpis A, Galloway A, Cater S, McPherson N. Development of a process envelope for friction stir welding of DH36 steel - A step change. Mater Des 2014;62:64–75. doi:10.1016/j.matdes.2014.04.066.

[2.4] Toumpis A, Galloway A, Cater S, Micallef D, Camilleri D, Poletz N, et al. Advances in friction stir welding of steel – project HILDA. Transp. Res. Arena, Paris, France: 2014.

[2.5] Cater S, Martin J, Galloway A, McPherson N. Comparison between Friction Stir and Submerged Arc Welding Applied to Joining DH36 and E36 Shipbuilding Steel. Frict Stir Weld Process VII 2013:49–58. doi:10.1007/978-3-319-48108-1_6.

[2.6] Thomas WM, Threadgill PL, Nicholas ED. Feasibility of friction stir welding steel. Sci Technol Weld Join 1999;4:365–72. doi:10.1179/136217199101538012.

[2.7] Colegrove PA. Modelling of friction stir welding. University of Cambridge, 2003.

[2.8] Song KH, Tsumura T, Nakata K. Development of Microstructure and Mechanical Properties in Laser-FSW Hybrid Welded Inconel 600. Mater Trans 2009;50:1832–7. doi:10.2320/matertrans.M2009058.

[2.9] Edwards P, Ramulu M. Peak temperatures during friction stir welding of Ti–6Al–4V. Sci Technol Weld Join 2010;15:468–72. doi:10.1179/136217110X12665778348425.

[2.10] Santos TG, Miranda RM, Vilaca P. Friction Stir Welding assisted by electrical Joule effect. J Mater Process Technol 2014;214:2127–33. doi:10.1016/j.jmatprotec.2014.03.012.

[2.11] Lienert TJ, Stellwag WL, JR, Grimmett BB, Warke RW. Friction Stir Welding Studies on Mild Steel. Weld J 2003:1–9.

[2.12] Ghosh M, Kumar K, Mishra RS. Process optimization for friction-stir-welded martensitic steel. Metall Mater Trans A Phys Metall Mater Sci 2012;43:1966–75. doi:10.1007/s11661-012-1084-x.

[2.13] Bilgin MB, Meran C. The effect of tool rotational and traverse speed on friction stir weldability of AISI 430 ferritic stainless steels. Mater Des 2012;33:376–83. doi:10.1016/j.matdes.2011.04.013.

[2.14] Reynolds AP, Tang W, Posada M, Deloach J. Friction stir welding of DH36 steel. Sci Technol Weld Join 2003;8:455–60. doi:10.1179/136217103225009125.

[2.15] McPherson NA, Galloway AM, Cater SR, Hambling SJ. Friction stir welding of thin DH36 steel plate. Sci Technol Weld Join 2013;18:441–50. doi:10.1179/1362171813Y.0000000122.

[2.16] Toumpis A, Galloway A, Polezhayeva H, Molter L. Fatigue Assessment of Friction Stir Welded DH36 Steel BT - Friction Stir Welding and Processing VIII. In: Mishra RS, Mahoney MW, Sato Y, Hovanski Y, editors., 2016, p. 11–9. doi:10.1007/978-3-319-48173-9_2.

[2.17] Toumpis A, Galloway A, Molter L, Polezhayeva H. Systematic investigation of the fatigue performance of a friction stir welded low alloy steel. Mater Des 2015;80:116–28. doi:10.1016/j.matdes.2015.04.046.

[2.18] Toumpis AI, Galloway AM, Camilleri D, Arbaoui L. Recent Developments in Steel Friction Stir Welding: Project HILDA. Proc. ASME 2015 Int. Mech. Eng. Congr. Expo., Houstan: 2015, p. 11. doi:10.1115/IMECE2015-51349.

[2.19] Toumpis A, Galloway A, Cater SR, Burling P, Stanhope C. Friction stir welding of steel for marine applications. 33rd Int. Conf. Ocean. Offshore Arct. Eng. OMAE 2014, California: 2014.

[2.20] Toumpis AI, Galloway AM, Arbaoui L, Poletz N. Thermomechanical deformation behaviour of DH36 steel during friction stir welding by experimental validation and modelling. Sci Technol Weld Join 2014;19:653–63. doi:10.1179/1362171814Y.0000000239.

[2.21] Tingey C, Galloway A, Toumpis A, Cater S. Effect of tool centreline deviation on the mechanical properties of friction stir welded DH36 steel. Mater Des 2015;65:896–906. doi:10.1016/j.matdes.2014.10.017.

[2.22] Ahmad B, Galloway A, Toumpis A. Advanced numerical modelling of friction stir welded low alloy steel. J Manuf Process 2018;34:625–36. doi:10.1016/j.jmapro.2018.07.003.

[2.23] Daftardar S. Laser Assisted Friction Stir Welding: Finite Volume Method and Metaheuristic Optimization. Louisiana State University, 2009.

[2.24] Lorrain O, Serri J, Favier V, Zahrouni H, El Hadrouz M. A Contribution to a Critical Review of Friction Stir Welding Numerical Simulation. J Mech Mater Struct 2009;4:351–69. doi:10.2140/jomms.2009.4.351.

[2.25] Camilleri D, Micallef D, Arbaoui L, Toumpis A, Galloway A. Numerical Modelling Techniques Applicable for the Prediction of Residual Stresses and Distortion due to Mild Steel DH36 Friction Stir Welding. 4th Int. Conf. Frict. Stir Welding, FSWP2015, Spain: 2015, p. 1–5.

[2.26] He X, Gu F, Ball A. A review of numerical analysis of friction stir welding. Prog Mater Sci 2014;65:1–66. doi:10.1016/j.pmatsci.2014.03.003.

[2.27] Assidi M, Fourment L, Guerdoux S, Nelson T. Friction model for friction stir welding process simulation: Calibrations from welding experiments. Int J Mach Tools Manuf 2010;50:143–55. doi:10.1016/j.ijmachtools.2009.11.008.

[2.28] Hoyos E, López D, Alvarez H. A phenomenologically based material flow model for friction stir welding. Mater Des 2016;111:321–30. doi:10.1016/j.matdes.2016.09.009.

[2.29] Camilleri D, Micallef D, Mollicone P. Thermal stresses and distortion developed in mild steel DH36 friction stir-welded plates: An experimental and numerical assessment. J Therm Stress 2015;38:485–508. doi:10.1080/01495739.2015.1015856.

[2.30] Chao YJ, Qi X, Tang W. Heat Transfer in Friction Stir Welding—Experimental and Numerical Studies. J Manuf Sci Eng 2003;125:138. doi:10.1115/1.1537741.

[2.31] Khandkar MZH, Khan JA, Reynolds AP. Prediction of temperature distribution and thermal history during friction stir welding: input torque based model. Sci Technol Weld Join 2003;8:165–74. doi:10.1179/136217103225010943.

[2.32] Selvamani ST, Umanath K, Palanikumar K. Heat Transfer Analysis during Friction Stir Welding of Al6061-T6 Alloy. Int J Eng Res Appl 2011;1:1453–60.

[2.33] Song M, Kovacevic R. Thermal modeling of friction stir welding in a moving coordinate system and its validation. Int J Mach Tools Manuf 2003;43:605–15. doi:10.1016/S0890-6955(03)00022-1.

[2.34] Colegrove PA, Shercliff HR. 3-Dimensional CFD modelling of flow round a threaded friction stir welding tool profile. J Mater Process Technol 2005;169:320–7. doi:10.1016/j.jmatprotec.2005.03.015.

[2.35] Kim D, Badarinarayan H, Kim JH, Kim C, Okamoto K, Wagoner RH, et al. Numerical simulation of friction stir butt welding process for AA5083-H18 sheets. Eur J Mech A/Solids 2010;29:204–15. doi:10.1016/j.euromechsol.2009.10.006.

[2.36] Nandan R, Roy GG, Debroy T. Numerical simulation of three-dimensional heat transfer and plastic flow during friction stir welding. Metall Mater Trans A 2006;37:1247–59. doi:10.1007/s11661-006-1076-9.

[2.37] Bastier A, Maitournam MH, Roger F, Dang Van K. Modelling of the residual state of friction stir welded plates. J Mater Process Technol 2008;200:25–37. doi:10.1016/j.jmatprotec.2007.10.083.

[2.38] Colegrove PA, Shercliff HR. Development of Trivex friction stir welding tool Part 2 – three-dimensional flow modelling. Sci Technol Weld Join 2004;9:352–61. doi:10.1179/136217104225021661.

[2.39] Chen C, Kovacevic R. Thermomechanical modelling and force analysis of friction stir welding by the finite element method. Proc Inst Mech Eng Part C-

Journal Mech Eng Sci 2004;218:509–19. doi:10.1243/095440604323052292.

[2.40] Gould JE, Feng Z. Heat flow model for friction stir welding of aluminum alloys. J Mater Process Manuf Sci 1998;7:185–94. doi:10.1106/648R-2CNE-2PD0-45L6.

[2.41] Li H, Liu D. Simplified Thermo-Mechanical Modeling of Friction Stir Welding with a Sequential FE Method. Int J Model Optim 2014;4:410–6. doi:10.7763/IJMO.2014.V4.409.

[2.42] Schmidt H, Hattel J. A local model for the thermomechanical conditions in friction stir welding. Model Simul Mater Sci Eng 2005;13:77–93. doi:10.1088/0965-0393/13/1/006.

[2.43] Mandal S, Rice J, Elmustafa AA. Experimental and numerical investigation of the plunge stage in friction stir welding. J Mater Process Technol 2008;203:411–9. doi:10.1016/j.jmatprotec.2007.10.067.

[2.44] Guerdoux S, Fourment L. A 3D numerical simulation of different phases of friction stir welding. Model Simul Mater Sci Eng 2009;17. doi:10.1088/0965-0393/17/7/075001.

[2.45] Schmidt H, Hattel J, Wert J. An analytical model for the heat generation in friction stir welding. Model Simul Mater Sci Eng 2004;12:143–57. doi:10.1088/0965-0393/12/1/013.

[2.46] Colligan KJ. Material Flow Behavior during Friction Stir Welding of Aluminum. Weld Journal, 1999;78:229.

[2.47] Al-Moussawi M, Smith A, Young AE, Cater S, Faraji M. Modelling of friction stir welding of DH36 steel. Int J Adv Manuf Technol 2017;92:341–60. doi:10.1007/s00170-017-0147-y.

[2.48] Xu S, Deng X, Reynolds AP, Seidel TU. Finite element simulation of material flow in friction stir welding. Sci Technol Weld Join 2001;6:191–3. doi:10.1179/136217101101538640.

[2.49] Seidel TU, Reynolds AP. Two-dimensional friction stir welding process model based on fluid mechanics. Sci Technol Weld Join 2003;8:175–83. doi:10.1179/136217103225010952.

[2.50] Schmidt HNB, Dickerson TL, Hattel JH. Material flow in butt friction stir welds in AA2024-T3. Acta Mater 2006;54:1199–209. doi:10.1016/j.actamat.2005.10.052.

[2.51] Zhang Z, Zhang Z, Zhang H. Numerical investigations of size effects on residual states of friction stir weld. Proc Inst Mech Eng Part B J Eng Manuf 2014;228:572–81. doi:10.1177/0954405413506191.

[2.52] Lu Y-F, Aoyagi Y. Temperature Rise and Heat Flux Induced by Laser Beam with Double-Gaussian Intensity Distribution. Jpn J Appl Phys 1995;34:3759–63.

[2.53] Simar A, Bréchet Y, De Meester B, Denquin A, Gallais C, Pardoen T. Integrated modeling of friction stir welding of 6xxx series Al alloys: Process, microstructure and properties. Prog Mater Sci 2012;57:95–183. doi:10.1016/j.pmatsci.2011.05.003.

[2.54] Chorin AJ. Numerical Solution of the Navier-Stokes Equations. Math Comput 1968;22:745–62. doi:10.2307/2004575.

[2.55] Neto DM, Neto P. Numerical modeling of friction stir welding process: A literature review. Int J Adv Manuf Technol 2013;65:115–26. doi:10.1007/s00170-012-4154-8.

[2.56] Grujicic M, He T, Arakere G, Yalavarthy H V, Yen C-F, Cheeseman BA. Fully coupled thermomechanical finite element analysis of material evolution during friction-stir welding of AA5083. J Eng Manuf 2010;224. doi:10.1243/09544054JEM1750.

[2.57] Awang M. Simulation of Friction Stir Spot Welding (FSSW) Process : Study of Friction Phenomena. West Virginia University, 2007.

[2.58] Li H. Coupled Thermo-Mechanical Modelling of Friction Stir Welding. University of Strathclyde, 2008.

[2.59] Ducobu F, Rivière-Lorphèvre E, Filippi E. Application of the Coupled Eulerian-Lagrangian (CEL) method to the modeling of orthogonal cutting. Eur J Mech A/Solids 2016;59:58–66. doi:10.1016/j.euromechsol.2016.03.008.

[2.60] Skrzat A. Application of coupled Eulerian-Lagrangian approach in metal forming simulations. Sci Lett Rzesz Univ Technol - Mech 2012;84:25–35.

doi:10.7862/rm.2012.9.

[2.61] Ivanova EA, Vilchevskaya EN, Müller WH. Time Derivatives in Material and Spatial Description—What Are the Differences and Why Do They Concern Us? BT - Advanced Methods of Continuum Mechanics for Materials and Structures. In: Naumenko K, Aßmus M, editors., Singapore: Springer Singapore; 2016, p. 3–28. doi:10.1007/978-981-10-0959-4_1.

[2.62] Al-Badour F, Merah N, Shuaib A, Bazoune A. Coupled Eulerian Lagrangian finite element modeling of friction stir welding processes. J Mater Process Technol 2013;213:1433–9. doi:10.1016/j.jmatprotec.2013.02.014.

[2.63] Zhu Z, Wang M, Zhang H, Zhang X, Yu T, Wu Z. A Finite Element Model to Simulate Defect Formation during Friction Stir Welding. Metals (Basel) 2017;7:256. doi:10.3390/met7070256.

[2.64] Hossfeld M. A fully coupled thermomechanical 3D model for all phases of friction stir welding. 11th Int. Symp. Frict. Stir Weld., Cambridge: 2016. doi:10.18419/opus-8845.

[2.65] Hossfeld M, Roos E. A new approach to modelling friction stir welding using the CEL method. Int. Conf. Adv. Manuf. Eng. Technol. NEWTECH, Stockholm: 2013, p. 179–90. doi:10.18419/opus-8825.

[2.66] Al-Badour F, Merah N, Shuaib A, Bazoune A. Thermo-mechanical finite element model of friction stir welding of dissimilar alloys. Int J Adv Manuf Technol 2014;72:607–17. doi:10.1007/s00170-014-5680-3.

[2.67] Umbrello D, M’Saoubi R, Outeiro JC. The influence of Johnson-Cook material constants on finite element simulation of machining of AISI 316L steel. Int J Mach Tools Manuf 2007;47:462–70. doi:10.1016/j.ijmachtools.2006.06.006.

[2.68] Daoud M, Chatelain JF, Bouzid A. Effect of rake angle-based Johnson-Cook material constants on the prediction of residual stresses and temperatures induced in Al2024-T3 machining. Int J Mech Sci 2017;122:392–404. doi:10.1016/j.ijmecsci.2017.01.020.

[2.69] Paturi UMR, Narala SKR, Kakustam S. Investigations on the effects of different constitutive models in finite element simulation of machining. Mater

Today Proc 2018;5:25295–302. doi:10.1016/j.matpr.2018.10.332.

[2.70] Zhang W, Wang X, Hu Y, Wang S. Predictive modelling of microstructure changes , micro-hardness and residual stress in machining of 304 austenitic stainless steel. Int J Mach Tools Manuf 2018;130–131:36–48. doi:10.1016/j.ijmachtools.2018.03.008.

[2.71] Çam G. Friction stir welded structural materials: beyond Al-alloys. Int Mater Rev 2011;56:1–48. doi:10.1179/095066010X12777205875750.

[2.72] Nandan R, Debroy T, Bhadeshia HKDH. Recent Advances in Friction Stir Welding – Process, Weldment Structure and Properties. Prog Mater Sci 2008;53:980–1023. doi:10.1016/j.pmatsci.2008.05.001.

[2.73] Banerjee B. The Mechanical Threshold Stress model for various tempers of AISI 4340 steel. Int J Solids Struct 2007;44:834–59. doi:10.1016/j.ijsolstr.2006.05.022.

[2.74] Song W, Ning J, Mao X, Tang H. A modified Johnson–Cook model for titanium matrix composites reinforced with titanium carbide particles at elevated temperatures. Mater Sci Eng A 2013;576:280–9. doi:10.1016/j.msea.2013.04.014.

[2.75] Yu M, Li WY, Li JL, Chao YJ. Modelling of entire friction stir welding process by explicit finite element method. Mater Sci Technol 2012;28:812–7. doi:10.1179/1743284711Y.0000000087.

[2.76] Micallef D, Camilleri D, Toumpis A, Galloway A, Arbaoui L. Local heat generation and material flow in friction stir welding of mild steel assemblies. Proc Inst Mech Eng Part L J Mater Des Appl 2015;230:586–602. doi:10.1177/1464420715583163.

[2.77] Al-Moussawi M, Smith A, Young AE, Cater S, Faraji M. An advanced numerical model of friction stir welding of DH36 steel. 11th Int. Symp. Frict. Stir Welding, TWI, Cambridge: 2016.

[2.78] Nandan R, Roy GG, Lienert TJ, DebRoy T. Numerical modelling of 3D plastic flow and heat transfer during friction stir welding of stainless steel. Sci Technol Weld Join 2006;11:526–37. doi:10.1179/174329306X107692.

[2.79] Sheppard T, Wright DS. Determination of flow stress: Part 1 constitutive equation for aluminium alloys at elevated temperatures. Met Technol 1979;6:215–23. doi:10.1179/030716979803276264.

[2.80] Hart EW. Constitutive relations for non elastic deformation. Nucl Eng Des 1978;46:179–85.

[2.81] Rai R, De A, Bhadeshia HKDH, DebRoy T. Review: friction stir welding tools. Sci Technol Weld Join 2011;16:325–42. doi:10.1179/1362171811Y.0000000023.

[2.82] Padhy GK, Wu CS, Gao S. Auxiliary energy assisted friction stir welding – status review. Sci Technol Weld Join 2015;20:1362171815Y.000. doi:10.1179/1362171815Y.0000000048.

[2.83] Yaduwanshi DK, Pal S, Bag S. Effect of Preheating on Mechanical Properties of Hybrid Friction Stir Welded Dissimilar Joint. 5th Int. 26th All India Manuf. Technol. Des. Res. Conf. (AIMTDR 2014), Guwahati: 2014.

[2.84] Bang HS, Bang HS, Song HJ, Joo SM. Joint properties of dissimilar Al6061-T6 aluminum alloy/Ti-6%Al-4%V titanium alloy by gas tungsten arc welding assisted hybrid friction stir welding. Mater Des 2013;51:544–51. doi:10.1016/j.matdes.2013.04.057.

[2.85] Campanelli SL, Casalino G, Casavola C, Moramarco V. Analysis and comparison of friction stir welding and laser assisted friction stir welding of aluminum alloy. Materials (Basel) 2013;6:5923–41. doi:10.3390/ma6125923.

[2.86] Sun YF, Konishi Y, Kamai M, Fujii H. Microstructure and mechanical properties of S45C steel prepared by laser-assisted friction stir welding. Mater Des 2013;47:842–9. doi:10.1016/j.matdes.2012.12.078.

[2.87] Chang WS, Rajesh SR, Chun CK, Kim HJ. Microstructure and Mechanical Properties of Hybrid Laser-Friction Stir Welding between AA6061-T6 Al Alloy and AZ31 Mg Alloy. J Mater Sci Technol 2011;27:199–204. doi:10.1016/S1005-0302(11)60049-2.

[2.88] Able N, Pfefferkorn F. Laser-assisted friction stir lap welding of aluminum. ASME Summer Heat Transf. Conf., San Francisco: 2005, p. 425–9. doi:10.1115/HT2005-72829.

[2.89] Zhu XK, Chao YJ. Numerical simulation of transient temperature and residual stresses in friction stir welding of 304L stainless steel. J Mater Process Technol 2004;146:263–72. doi:10.1016/j.jmatprotec.2003.10.025.

[2.90] Sundqvist J, Kim K, Bang H, Bang H, Kaplan AFH. Numerical simulation of laser preheating of friction stir welding of dissimilar metals 2017;1718. doi:10.1080/13621718.2017.1391936.

[2.91] Shi L, Wu CS, Sun Z. An integrated model for analysing the effects of ultrasonic vibration on tool torque and thermal processes in friction stir welding. Sci Technol Weld Join 2017;1718. doi:10.1080/13621718.2017.1399545.

[2.92] Casavola C, Cazzato A, Moramarco V. Thermographical Analysis of Friction Stir Welding and Laser Assisted Friction Stir Welding. XIII Youth Symp. Exp. Solid Mech., Decin, Czech Republic: 2014, p. 15–9.

[2.93] Álvarez AI, García M, Pena G, Sotelo J, Verdera D. Evaluation of an induction-assisted friction stir welding technique for super duplex stainless steels. Surf Interface Anal 2014;46:892–6. doi:10.1002/sia.5442.

[2.94] Potluri H, Jones JJ, Mears L. Comparison of Electrically-Assisted and Conventional Friction Stir Welding Processes by Feed Force and Torque. ASME 2013 Int. Manuf. Sci. Eng. Conf. Vol. 1 Process., Madison: 2013, p. 10. doi:10.1115/MSEC2013-1192.

[2.95] Liu X, Lan S, Ni J. Electrically assisted friction stir welding for joining Al 6061 to TRIP 780 steel. J Mater Process Technol 2015;219:112–23. doi:10.1016/j.jmatprotec.2014.12.002.

[2.96] Sinclair PC, Longhurst WR, Cox CD, Lammlein DH, Strauss AM, Cook GE. Heated friction stir welding: An experimental and theoretical investigation into how preheating influences process forces. Mater Manuf Process 2010;25:1283–91. doi:10.1080/10426914.2010.496122.

[2.97] Álvarez AI, Cid V, Pena G, Sotelo J, Verdera D. Assisted friction stir welding of carbon steel: Use of induction and laser as preheating techniques. Frict Stir Weld Process VII 2016:117–26. doi:10.1007/978-3-319-48108-1_13.

[2.98] Liu XC, Wu CS, Padhy GK. Improved weld macrosection, microstructure and mechanical properties of 2024Al-T4 butt joints in ultrasonic vibration enhanced friction stir welding. Sci Technol Weld Join 2015;20:345–52. doi:10.1179/1362171815Y.0000000021.

[2.99] Joo S. Joining of dissimilar AZ31B magnesium alloy and SS400 mild steel by hybrid gas tungsten arc friction stir welding. Met Mater Int 2013;19:1251–7. doi:10.1007/s12540-013-6016-9.

[2.100] Bang HS, Bang HS, Jeon GH, Oh IH, Ro CS. Gas tungsten arc welding assisted hybrid friction stir welding of dissimilar materials Al6061-T6 aluminum alloy and STS304 stainless steel. Mater Des 2012;37:48–55. doi:10.1016/j.matdes.2011.12.018.

3. Theoretical background of FSW numerical modelling

Understanding the theoretical background of the simulation process of friction stir welding (FSW) is significant to comprehend the model outcomes, more proficiently. This chapter provides a basis of the numerical modelling techniques commonly applied for the FSW process along with the justification about certain approaches used in this thesis. After that, the standard governing equations relating to the thermal, mechanical and thermomechanical principles are thoroughly discussed. Lastly, the fully coupled thermal structural method has been described, focussing on the theoretical insights for the development of the simulation methodology for the FSW process.

3.1. Overview of numerical modelling techniques

FSW is a thermomechanical process, which involves a direct influence of the thermal effects over the structural deformation of the material, and vice versa. For the simulation of FSW, there are four main elements involved, as shown in Figure 3.1.

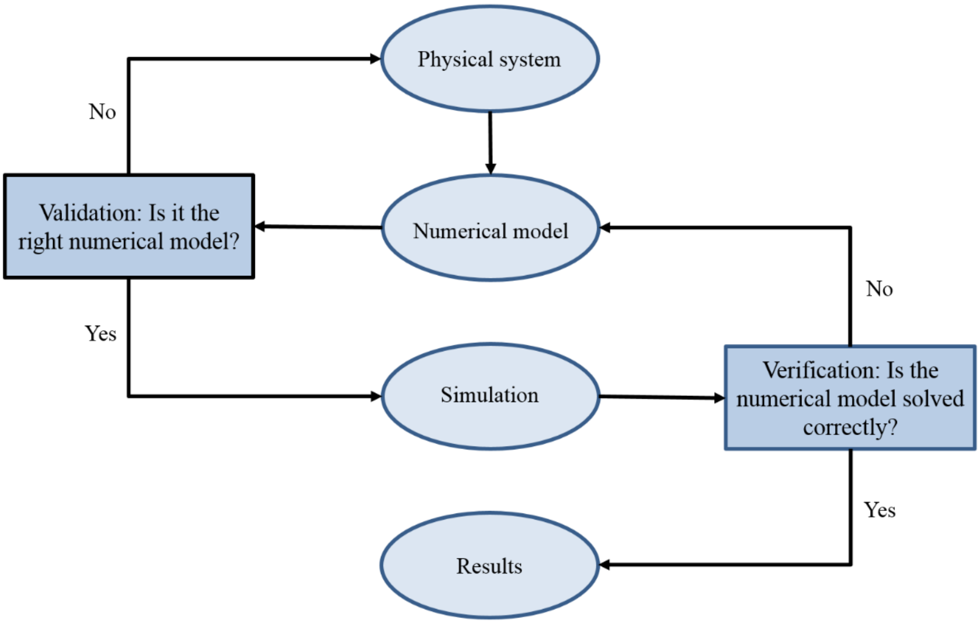

Figure 3.1: Flow chart of numerical modelling of the FSW process.

To transfer all parameters from the physical system to the numerical model, necessary information must be accurately derived through the experimental procedure. Major parameters to be included in the numerical model are typically model geometry, material properties, initial and boundary conditions. After the physical system and the numerical model are found to be in close alignment, a suitable simulation technique is then selected to obtain accurate results. There are several numerical methods to solve the FSW model as a differential equation problem. Numerical methods reduce the simplified model to an extent that is solvable through a finite number of numerical operations [3.1]. Some of them, which are widely used in engineering, are domain decomposition method, mesh free method, spectral method, finite difference method, finite volume method, and the finite element method.

I. Domain decomposition method

In this method, the computational domain is discretised into further subdomains, on which the boundary value problem is defined [3.2]. The computational domain can be sectioned in either intersecting or separate subdomains. The application of the parallel solution algorithm allows the domain decomposition method to be used in the framework of any other numerical methods involving partial differential equations discussed in the section 3.1. except mesh free method. This helps in obtaining the algebraic solution more efficiently when using the parallel computation.

II. Spectral method

Spectral method is a global technique, where various partial differential equations are solved using Fourier series. Unlike other methods, it does not rely only on the information obtained by the neighbouring nodes, but also from the entire domain. This technique is generally applied where time or space dependent solution is computed with long time integration [3.3].

III. Finite Difference Method (FDM)

The finite difference method is close to the numerical techniques, which are used to solve ordinary differential equations [3.2]. It approximates the derivatives by discretising the model domain in finite number of grid points. The model domain is discretised in the space and time, and the solution is then approximated by computing at the respective space and time points. Finite differences, either forward, central or backward, are then created between the consecutive nodes in the grid points based on the Taylor series.

IV. Finite Volume Method (FVM)

As the name suggests, the computational domain is decomposed into finite control volumes. Integral balance equations are formulated for every control volume as surface fluxes. Due to the balance principle, flux entering a control volume is equal to the one leaving the control volume, hence making the method conservative. The final solution of the discrete algebraic system is obtained by assembling all function values and derivatives on all control volume nodes. Due to the unstructured mesh formulation, this method is widely used in computational fluid dynamics (CFD) problems.

V. Finite Element Method (FEM)

The finite element method, also known as the finite element analysis, expresses the differential equations into a set of algebraic equations by discretising a large problem into smaller parts, also known as finite elements. Solutions obtained by solving the finite elements are then assembled as a larger set of equations, which models the whole problem. Various techniques are utilised to calculate the solution of the function by reducing the associated error function. These techniques are formed from a field of mathematical analysis known as ‘Calculus of variations’. Following are the different steps for obtaining a solution of a general continuum problem by finite element method [3.4]:

1. Discretisation of the model.
2. Selection of a proper interpolation or displacement model.
3. Derivation of the load factors and element stiffness matrices.
4. Assembly of element equations to obtain the equilibrium equations.
5. Solution for unknown displacements at the nodal points.
6. Calculation of element strains and stresses.

3.1.1. Formulations according to the Lagrangian and Eulerian approaches

The numerical solutions can be approximated by two different classical approaches: Lagrangian and Eulerian approaches. Both of them differ significantly from each other in the interpretation of the material flow.

3.1.1.1. Lagrangian approach

In the Lagrangian approach, the deformation results in the nodes displacing with the defined material, normally indicating their motion through a displacement vector from the original location, Figure 3.2. Each individual particle is tracked, and the temporal change in its property is recorded for the respective position with time [3.5]. This approach is typically used in the structural mechanics. Any material flow between two elements is not possible as the material and the element point always move and remain together. Due to this trait, the Lagrangian approach is particularly suitable for keeping the track record of the boundary conditions, surface tracking and traceability of the material displacement.

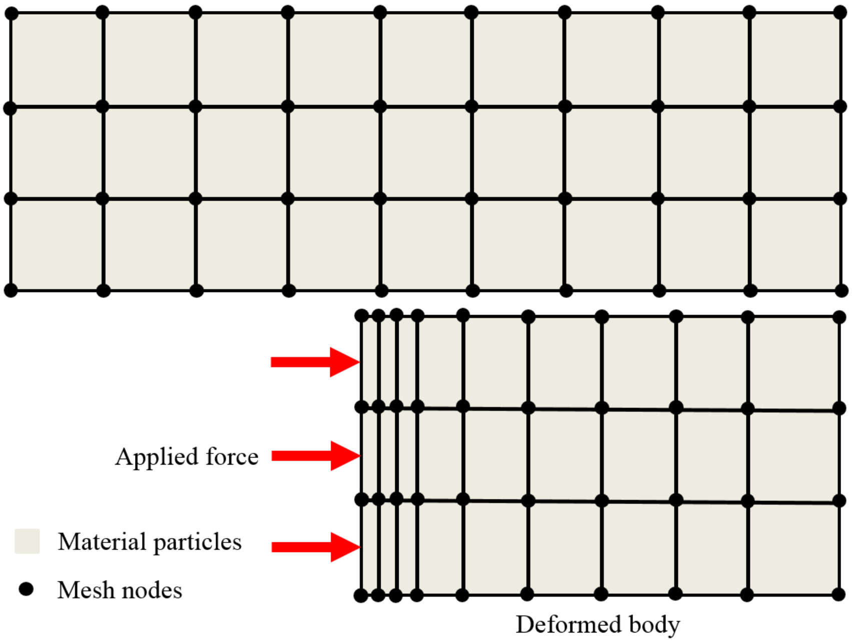

Figure 3.2: Material deformation and flow according to the Lagrangian approach.

However, the elements in the Lagrangian approach often become distorted due to large displacement in the nodes. Since the FSW process involves large deformations, a pure Lagrangian approach is not suitable for such numerical representation.

3.1.1.2. Eulerian approach

The element distortion problem does not arise when using the Eulerian approach, as it uses a fixed domain at all times, not following the underlying material, as shown in Figure 3.3. This permits the defined material to flow freely in the domain without distorting any element. Hence, the Eulerian approach is the basis for solving problems of fluid mechanics, commonly known as computational fluid dynamics (CFD) [3.6].

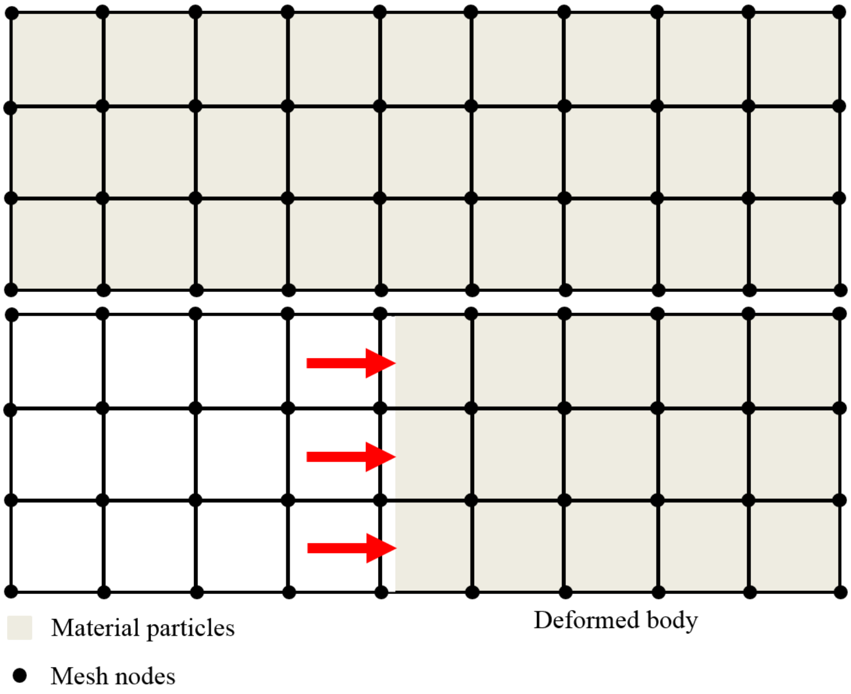

Figure 3.3: Material deformation and flow according to the Eulerian approach.

Despite of this advantage, certain limitations come with classic Eulerian approach as well. Using fixed domain consequently limits the implementation of constraints along with the tracking of surfaces and the traceability of the material displacement. There are many upgraded extensions of the Eulerian approach, such as the volume tracking or volume-of-fluid method [3.7,3.8]. Additional computational effort is required for using these extensions as the tracking and reconstruction of the surfaces are managed distinctly. In addition, as the boundary nodes, such as element integration points, do not coincide with the geometric boundary in this approach, this also affects the overall behaviour of the model. This is critical when applying any contact and frictional specifications in the model.

3.1.2. Combined approaches

Based on the above presented properties of the formulations according to Lagrangian and Eulerian approaches, combined formulations have been developed from these classical approaches, in order to solve the models with large deformation problems.

3.1.2.1. ALE Approach

A most common formulation developed by merging both classical approaches is known as the Arbitrary Lagrangian Eulerian (ALE) approach. ALE approach has been implemented in many commercial finite element tools [3.9-3.12]. By including the advantages of both Eulerian and Lagrangian approaches, ALE makes it possible for the nodes to either move in a Lagrangian way with continuum deformation or to remain stationary according to the Eulerian formulation, as shown in Figure 3.4. The independency of the domain movement makes it possible to visualise significantly large deformations than before. In addition, the solution accuracy becomes better than applying the corresponding Eulerian description.

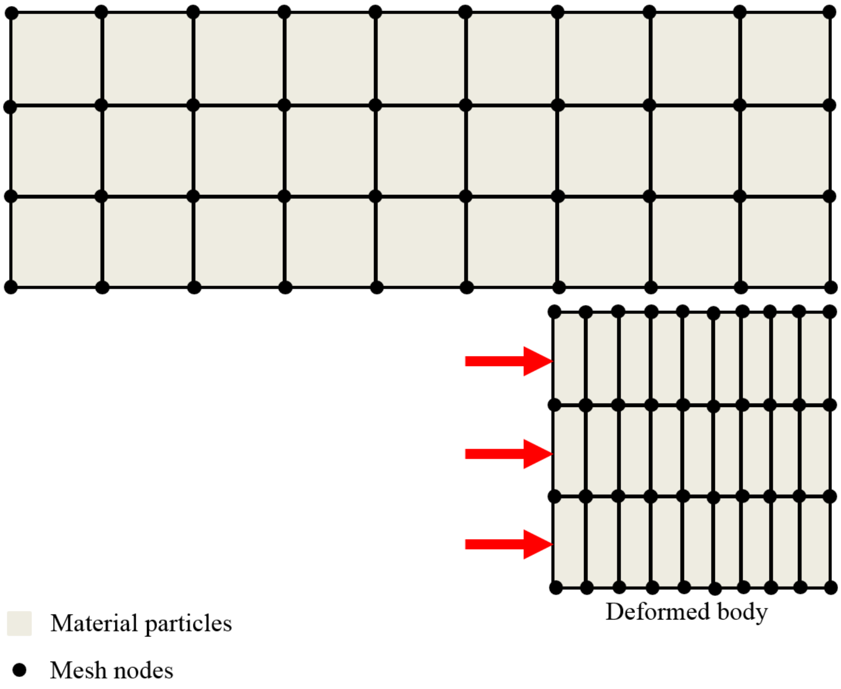

Figure 3.4: Material deformation and flow according to the ALE approach.

These qualities make ALE preferable for solving structural problems with large degrees of deformation. Although a direct topology change of the domain is not possible [3.13,3.14], but the possibilities of the adaptive meshing for the domain refinement brings promising results [3.11,3.15,3.16].

In general, ALE approach can be directly implemented [3.17], however, they are typically applied by splitting the method especially in commercial FE programs, for simplified modular use. The procedure starts by applying a Lagrangian time step, which is followed by a remapping or advection step for any distorted mesh, as listed below [3.14]:

1. Perform the Lagrangian time step.
2. Execute the advection step:
    a. Selection of nodes for movement.
    b. Movement of the edge nodes.
    c. Movement of the inner nodes.
    d. Calculation of the transfer of elemental variables.
    e. Calculation of the momentum transport and updating.

Since the computational cost for the ALE approach is raised about two to five times than a normal Lagrangian time step, this is usually not performed after each Lagrangian step. The ALE operator parameters, which are applied to simulate the steps as mentioned above, can usually be specified in commercial FE programs. However, as discussed in the section 2.3.2, detailed modelling features cannot be visualised. Furthermore, the ALE approach permits the use of a single computer processor only, hence increasing the computational cost.

3.1.2.2. CEL Approach

The approach, called as Coupled Eulerian Lagrangian (CEL), is very closely related to the extended Eulerian approach of partially filled elements. Noh [3.18] formulated this kind of coupling of Lagrangian and Eulerian bodies back in 1964, but apart from some special scientific implementations, this approach has found its way into the commercial FE packages in recent years only.

CEL approach uses a combination of overlapping and independent domains of Eulerian and Lagrangian formulations, whereby the interaction between the bodies of different formulations is possible in that overlapping area. If two differently formulated bodies come into each other's contact, the edge of the Lagrangian region is usually defined as the contact surface, at which all equations for the contact are solved [3.19]. In this case, the velocity of the covered edge of the element is calculated by the help of the normal velocity of the Lagrangian boundary similar to the Eulerian velocity in the same direction [3.20]. This helps in modelling large deformations without any mesh distortions, as shown in Figure 3.5. Similar to the Noh's original contact formulation, there are other extensions to this classical approach as well [3.19].

The contact methodology makes the CEL approach particularly interesting for solving highly dynamic, non-linear or problems with very large deformations. Unlike the classical Eulerian formulation, CEL enables the formation, fusion and tracking of free surfaces [3.19]. It is distinguishing because numerical diffusion problems are considered to be limited by appropriate domain designs or additional algorithms. There are currently only a few publications regarding the use of the CEL approach as compared to the ALE approach. However, there is a strong focus on highly dynamic problems with high degrees of deformation and complex contact situations, such as crash, ballistic and FSW process simulations [3.21-3.24].

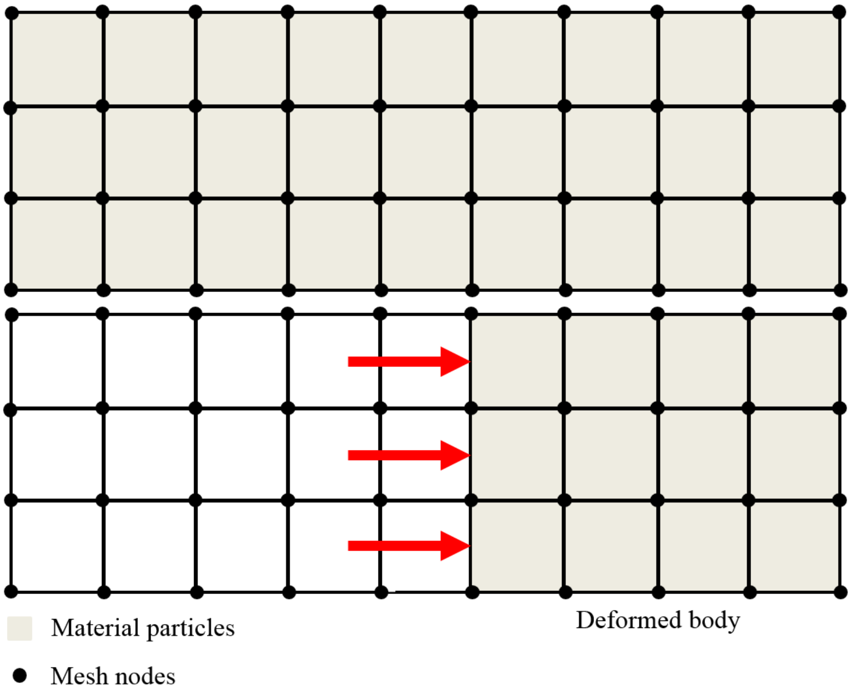

Figure 3.5: Material deformation and flow according to the CEL approach.

3.2. Governing equations

3.2.1. Thermal principles

Understanding the heat transfer basics assists in determination of the temperature distribution in the FSW model. The heat transfer during the FSW process describes the thermomechanical history of the model [3.25], and is calculated from the fundamental laws of thermodynamics. The first law of thermodynamics states that any heat input to the system from the surroundings is equal to the work done by the system on its surrounding [3.26]. The derivation of this law comes from the conservation of energy principle for the heat and thermodynamics processes [3.11]. Therefore, by the conservation of energy [3.27]:

$$E_{in} + E_{generated} = \Delta U + E_{out} \tag{3.1}$$

Where 'E' is the energy in joules (J), and 'ΔU' is the energy change, stored in kilowatt-hour (kWh). For one-dimensional heat conduction, heat transfer through a control volume (CV) is presented in Figure 3.6. The equation (3.1) then becomes:

$$q_x Adt + QAdxdt = \Delta U + q_{x+dx} Adt \tag{3.2}$$

'q_x' is the heat transferred into the CV from the surface area 'A' in kW/m^2, and 'q_{x+dx}' is the heat transferred out of the CV. 'Q' is the heat generation rate per unit volume, in kW/m^3.

The Fourier law of heat conduction defines the relation between the temperature gradient and the heat flux, equation (3.3).

$$q_x = -K_{xx} \frac{dT}{dx} \tag{3.3}$$

Where K_{xx} is the thermal conductivity of the material in the x direction, in kW/(m.°C), and T is the temperature, in °C. The equation (3.3) implies that the axial heat flux is proportional to the temperature gradient in the same direction. The minus sign in the equation (3.3) indicates the direction of the heat flow. Likewise, the equation for 'q_{x+dx}' becomes:

$$q_{x+dx} = -K_{xx} \frac{dT}{dx}\bigg|_{x+dx} \tag{3.4}$$

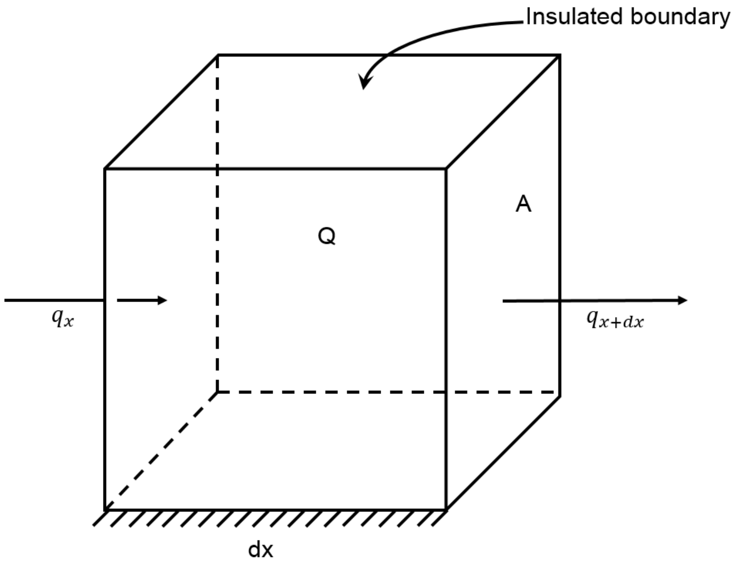

Figure 3.6: CV for one dimensional heat transfer [3.27].

The equation (3.4) is then solved by using the Taylor series of expansion.

$$q_{x+dx} = -\left[K_{xx}\frac{dT}{dx} + \frac{d}{dx}\left(K_{xx}\frac{dT}{dx}\right)dx\right] \tag{3.5}$$

The change in the stored energy is given in the equation (3.6).

$$\Delta\, U \;=\; \text{specific heat x mass x change in temperature} \tag{3.6}$$

$$= c\;(\rho.A\;dx)\;dt \tag{3.7}$$

Where 'c' is the specific heat, in kW.h/(kg.^{o}C), and 'ρ' is the density of the material, in kg/m^3. Substituting the equations (3.3), (3.5) and (3.7) into (3.2) give the one dimensional heat transfer equation (3.8).

$$\frac{\partial}{\partial x}\left(K_{xx}\frac{\partial T}{\partial x}\right) + Q = \;\rho c\frac{\partial T}{\partial t} \tag{3.8}$$

For the calculation of the three dimensional heat transfer, as shown in Figure 3.7, the equation (3.8) is extended for all three axial heat transfers (q_x, q_y and q_z in Figure 3.7) as:

$$\frac{\partial}{\partial x}\left(K_{xx}\frac{\partial T}{\partial x}\right) + \frac{\partial}{\partial y}\left(K_{yy}\frac{\partial T}{\partial y}\right) + \frac{\partial}{\partial z}\left(K_{zz}\frac{\partial T}{\partial z}\right) + Q = \;\rho c\frac{\partial T}{\partial t} \tag{3.9}$$

The 'Q' in the equation (3.9) is the volumetric heat source for the three dimensional model. Temperature dependent thermal conductivity and specific heat have been applied in the models. This requires the software to calculate the equation (3.9) with different values of 'K' and 'c' based on the varying temperature during FSW.

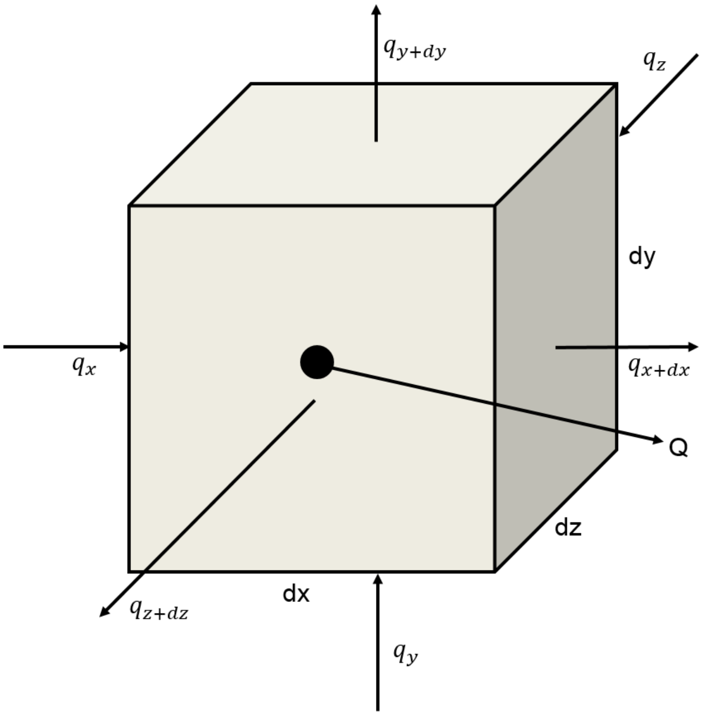

Figure 3.7: Heat transfer in a three dimensional element [3.27].

3.2.2. Mechanical fundamentals

The classic plasticity theory describes the material as either elastic or plastic. If a stress applied on the material is less than the yield point, the corresponding strain would be regarded as elastic. In this case, the material will return to its original shape. The elastic region is of two types; linear and nonlinear. Whereas in the plastic deformation, a permanent change in the material is observed after the loading and unloading of stress larger than the material's yield point. A nonlinear behavior of materials can be characterised by a unique stress-strain relationship, as shown in Figure 3.8. The linearity or nonlinearity of the elastic strain is assumed only below the yield stress of the material. The unloading of such stress determines as the elastic material follows the same pattern, and the plastic material trails a unique history dependant pattern [3.28]. Therefore, determination of the yield criteria is crucial for modelling accurate FSW phenomena.

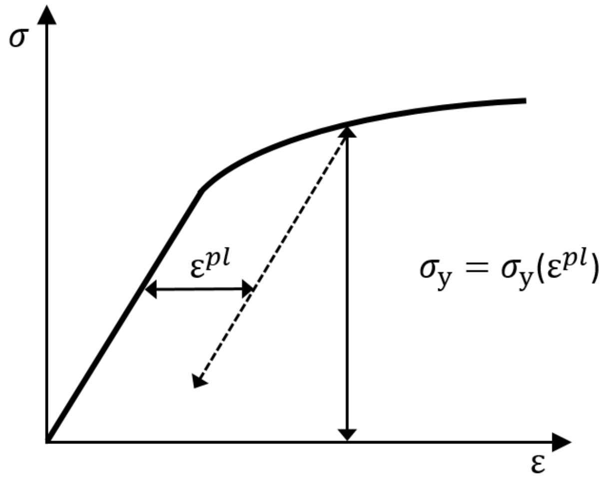

Figure 3.8: Uniaxial behaviour of the material at strain hardening plasticity [3.28].

3.2.2.1. Yield criteria

The yield of a ductile material is considered as independent to the equivalent pressure stress [3.11]. So the yield criterion is only dependant on the deviatoric stress tensor S [3.29]:

$$S = \sigma + p\,\mathrm{I} \tag{3.10}$$

$$p = -\frac{1}{3}\,trace\,(\sigma) \tag{3.11}$$

Where 'p' denotes the equivalent pressure. For an isotropic material, all functions can be represented as the deviatoric stress variants; J_1 , J_2 and J_3.

$$J_1 = 0 \tag{3.12}$$

$$J_2 = -(S_1S_2 + S_2S_3 + S_3S_1) \tag{3.13}$$

$$J_3 = -(S_1S_2S_3) \tag{3.14}$$

Hence, the yield surface is limited to dependent on only two variants; J_2, J_3. In addition, the metal often reacts as plastic in initial tension or compression loading. So following this, the second yield function of the stress tensor is $f(J_2) = constant$. Therefore, the von Mises yield criteria can be written by expressing the J_2 in terms of the stress as:

$$(\sigma_1 - \sigma_2)^2 + (\sigma_2 - \sigma_3)^2 + (\sigma_3 - \sigma_1)^2 = constant \tag{3.15}$$

The constant in the equation (3.15) is attributed as the equivalent stress '$\bar{\sigma}$'. When the loading on the material reaches the yield point, the equibalent stress becomes equal to the yield stress 'σ_y'. So rearranging the equation (3.15) gives:

$$\bar{\sigma} = \sqrt{\frac{(\sigma_1 - \sigma_2)^2 + (\sigma_2 - \sigma_3)^2 + (\sigma_3 - \sigma_1)^2}{2}} \tag{3.16}$$

Another yield criterion, Tresca yield, calculates the yield stress based on the maximum shear stress in the material. Figure 3.9 presents the three dimensional isotropic yield surfaces in the principal stress space. The Tresca yield criterion states that the maximum shear stress with in the model would be equal to the shear stress in a tensile specimen '$\frac{\bar{\sigma}}{2}$' [3.11]. This means that:

$$\bar{\sigma} = max[|\sigma_1 - \sigma_2|, |\sigma_2 - \sigma_3|, |\sigma_3 - \sigma_1|] \tag{3.17}$$

The Tresca yield criterion is often regarded as simple and conservative due to more reduced yield stresses as compared to the von Mises criterion. Mostly, von Mises criterion is applied in the commercial finite element analysis software for isotropic materials.

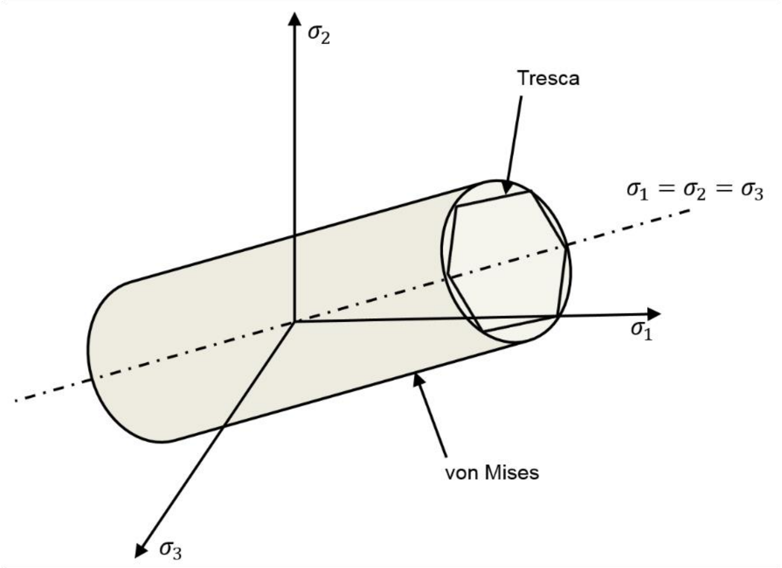

Figure 3.9: Isotropic yield surfaces in the principal stress space for von Mises and Tresca criteria (Adapted from [3.28]).

3.2.2.2. Flow rule

Von Mises suggested that the yield surface is linked to the behavior that defines the plastic strain increments [3.28]. The components of the plastic strain tensor, defined as $\underline{\varepsilon}^{pl}$, are given by:

$$\underline{\varepsilon}^{pl} = \dot{\lambda}\, F_{\underline{\sigma}} \tag{3.18}$$

$$F_{\underline{\sigma}} = \frac{\partial F}{\partial \underline{\sigma}} \tag{3.19}$$

where '$\dot{\lambda}$' is a constant of proportionality, not yet determined. It is often known as the 'plastic consistency' parameter. When the plastic deformation is continued, the $\dot{F} = 0$ and $\dot{\lambda} > 0$, whereas $\dot{\lambda} = 0$ and $\dot{F} \neq 0$ in the case of elastic loading/unloading. This leads to a basic constraint condition in Kuhn-Tucker form [3.28].

$$\dot{\lambda}\, F = 0 \tag{3.20}$$

The above rule is also known as the normality principle as the equation (3.18) can be used to estimate the plastic strain rate components to be normal to the yield surface in the space of nine stress and strain dimensions [3.28].

3.2.2.3. Strain hardening

The strain hardening principle guides the evolvement of the yield surface with the strain when yielding occurs. In an ideal plasticity, the plastic strain has no effect on the yield stress, and any stress greater than the yield stress will not be continued [3.11]. Therefore, the plastic flow occurs when the yield point of the material is achieved.

There are two kinds of hardening in Abaqus; Isotropic and Kinematic. In the isotropic hardening, the yield surface shape is identical whereas the size varies uniformly in all direction [3.11]. This shows that the general equation (3.16) does not change on the influence of the plastic straining except for the equivalent stress '$\bar{\sigma}$'.

Whereas, in the kinematic hardening, the yield surface is moved without any change in the shape and size of the surface. The plastic strain history and the centre of the yield surface is demonstrated with the help of a tensor. Kinematic hardening is mostly used to model the cyclic loading of metals [3.30].

3.2.2.4. Rate dependence

Many metals demonstrate an increase in their yield strength as increasing the strain rates. This becomes significant for certain metals when the strain rates are between 0.1 and 1 per second, and in high energy dynamic events or manufacturing process like FSW, where the strain rate ranges between 10 and 100 per seconds [3.31]. The yield stress '$\overline{\sigma}$' of the material normally depends on the work hardening. In the isotropic hardening models, the yield stress is normally presented as a function of an equivalent plastic strain '$\overline{\varepsilon}^{\mathrm{pl}}$', inelastic strain rate '$\dot{\varepsilon}^{\mathrm{pl}}$', temperature T and any other predefined field variables f_i [3.31].

$$\overline{\sigma} = \overline{\sigma}(\overline{\varepsilon}^{\mathrm{pl}}, \dot{\varepsilon}^{\mathrm{pl}}, \mathrm{T}) \tag{3.21}$$

3.2.3. Thermomechanical principles

3.2.3.1. Energy balance

The conservation of the energy is implied from the first law of thermodynamics. It states that the sum of the rate of kinetic and internal energy for a fixed body of material is equal to the sum of the rate of work done by the surface and body forces [3.29]. This can be presented as:

$$\frac{dE_U}{dt} + \frac{dE_K}{dt} = \frac{dE_W}{dt} + \frac{dQ}{dt} \tag{3.22}$$

Where 'E_U' corresponds to the internal energy of the system, 'E_K' is the kinetic energy, 'E_W' is the work done externally and by the body forces, and 'Q' is the heat input. All terms in the equation (3.22) are then defined as [3.29]:

$$\frac{dE_U}{dt} = \frac{d}{dt}\int_V \rho U dV = \int_0^t (\int_V \sigma : \dot{\varepsilon} dV)\, dt \tag{3.23}$$

Where 'U' is the internal energy density.

$$\frac{dE_K}{dt} = \frac{d}{dt}\int_V \frac{1}{2}\rho v.v dV = \int_V \rho g.v dV \tag{3.24}$$

$$\frac{dE_W}{dt} = \int_V \rho g.v dV + \int_S \sigma.n.v dS \tag{3.25}$$

And the time change in the heat input is expressed as:

$$\frac{dQ}{dt} = -\int_S q.ndS \tag{3.26}$$

Substituting the equations (3.23-3.26) into (3.23) gives:

$$\frac{d}{dt}\int_V \rho U dV + \int_V \rho g.vdV = \int_V \rho g.vdV + \int_S \sigma.n.vdS - \int_S q.ndS \tag{3.27}$$

$$\int_V \rho \frac{dU}{dt} dV = \int_S \sigma.n.vdS - \int_S q.ndS \tag{3.28}$$

Or

$$\int_V \rho \frac{dU}{dt} dV = \int_v \sigma : \dot{\varepsilon} dV - \int_v div(q) dV \tag{3.29}$$

The internal energy can further be divided into two parts for convenience [3.29]:

$$\int_0^t (\int_V \sigma : \dot{\varepsilon} dV)\, dt = \int_0^t [\int_V (\sigma^c + \sigma^d) : \dot{\varepsilon} dV] dt \tag{3.30}$$

$$= \int_0^t (\int_V \sigma^c : \dot{\varepsilon} dV) dt + \int_0^t (\int_V \sigma^d : \dot{\varepsilon} dV) dt \tag{3.31}$$

$$= E_I + E_V \tag{3.32}$$

Where 'σ^c is the stress derived from the constitutive equations specified by the user, and 'σ^d' is the viscous stress, defined for the bulk viscosity, material damping, and dashpots. 'E_I' is the remaining energy, which can be called as the internal energy, whereas 'E_V' is the energy dissipated by viscous effects. The strain decomposition '$\dot{\varepsilon}$' can be presented as:

$$\dot{\varepsilon} = \dot{\varepsilon}^{el} + \dot{\varepsilon}^{pl} + \dot{\varepsilon}^{cr} \tag{3.33}$$

Where '$\dot{\varepsilon}^{el}$' is the elastic strain rate, '$\dot{\varepsilon}^{pl}$' is the plastic strain rate, and '$\dot{\varepsilon}^{cr}$' is the creep strain rate. So the internal energy, 'E_I', can be expressed as:

$$E_I = \int_0^t (\int_V \sigma^c : \dot{\varepsilon} dV) dt \tag{3.34}$$

$$= \int_0^t (\int_V \sigma^c : \dot{\varepsilon}^{el} dV) dt + \int_0^t (\int_V \sigma^c : \dot{\varepsilon}^{pl} dV) dt + \int_0^t (\int_V \sigma^c : \dot{\varepsilon}^{cr} dV) dt \tag{3.35}$$

$$= E_S + E_P + E_C \tag{3.36}$$

Where 'E_S' is the recoverable elastic strain, 'E_P' is the energy dissipated by plasticity, and 'E_C' is the energy dissipated by time dependent deformation, which can be the creep, swelling and viscoelasticity.

3.2.3.2. The second law of thermodynamics

The second law of thermodynamics states that it is impossible for a self-acting system to transfer the heat from a colder body to a hotter body, without any external influence [3.26]. This can also be defined as "the entropy of an isolated system will have a tendency to increase over the time, when not in equilibrium, hence attaining a maximum value of equilibrium" [3.11]. It is expressed in the equation (3.37) [3.26].

$$\frac{dS_{en}}{dt} \geq \frac{1}{T}\frac{dQ}{dt} \tag{3.37}$$

Where '$\frac{dS_{en}}{dt}$' is the rate of change of the entropy of the system with time. The total entropy of a domain Ω can be presented as:

$$S_{en} = \int_{\Omega} \rho s_{en}\, dV \tag{3.38}$$

The 's_{en}' denotes the density of the entropy for the whole system. With substitutions in the equation (3.37), a Clausius-Duhem inequality equation is achieved [3.11]:

$$\rho \frac{ds_{en}}{dt} + \frac{div(q)}{T} - \frac{q.\nabla T}{T^2} \geq 0 \tag{3.39}$$

As the equation (3.29) can be expressed for any subdomain in the body as [3.11]:

$$\rho \frac{dU}{dt} = \sigma : \dot{\varepsilon} - div(q) \tag{3.40}$$

Therefore, substituting equation (3.40) into (3.39) gives:

$$\rho \left(T \frac{ds_{en}}{dt} - \frac{dU}{dt} \right) \sigma : \dot{\varepsilon} - \frac{q.\nabla T}{T^2} \geq 0 \tag{3.41}$$

The free energy 'Ψ' is defined as:

$$\Psi = \mathrm{U} - \mathrm{T} s_{en} \tag{3.42}$$

Or

$$\frac{d\Psi}{dt} = \frac{d\mathrm{U}}{dt} - \ s_{en}\frac{d\mathrm{T}}{dt} - T\frac{ds_{en}}{dt} \tag{3.43}$$

So combining the equations (3.41) and (3.43) gives the second form of the Clausius-Duhem inequality [3.11]:

$$\rho\left(\frac{d\Psi}{dt} + s_{en}\frac{d\mathrm{T}}{dt}\right) + \ \sigma : \dot{\varepsilon} - \frac{q.\nabla T}{T^2} \geq \ 0 \tag{3.44}$$

3.2.3.3. Heat equation for plastic or viscoplastic materials

The evolution of the system is developed by the above-mentioned state functions, such as the internal energy, entropy and the free energy. These state functions do not depend upon the state paths, and are characterised by the state and internal variables. The internal and state variables define the behavior in the physical occurrences, for example, phase change proportion, the dislocation density, microstructural changes and the plastic strains. The free energy ‘Ψ’ equation (3.43) can be used together with the first law of thermodynamics equation (3.40), as presented in the equation (3.45) [3.11].

$$\rho\left(\frac{d\Psi}{dt} + s_{en}\frac{d\mathrm{T}}{dt} + T\frac{ds_{en}}{dt}\right) - \sigma : \dot{\varepsilon} + div(q) = 0 \tag{3.45}$$

As the free energy is considered dependent only on the elastic strain, internal variables ‘$\dot{\alpha}$’ and temperature for elasto-viscoplasticity and elasto-plasticity, the equation becomes:

$$\frac{d\Psi}{dt} = \frac{\delta\Psi}{\delta\varepsilon^{el}} : \dot{\varepsilon} + \frac{\delta\Psi}{\delta\alpha} : \dot{\alpha} + \frac{\delta\Psi}{\delta T} : \dot{T} \tag{3.46}$$

Any thermodynamic forces A_α related to the internal variable can be presented as:

$$A_\alpha = \ \rho\frac{\delta\Psi}{\delta\alpha} \tag{3.47}$$

Substitution of the equation (3.46) into the Clausius-Duhem inequality gives:

$$\left(\sigma - \ \rho\frac{\delta\Psi}{\delta\varepsilon^{el}}\right) : \dot{\varepsilon} + \sigma : \dot{\varepsilon}^{pl} - A_\alpha : \dot{\alpha} - \rho\left(\frac{\delta\Psi}{\delta T} + s_{en}\right)\frac{d\mathrm{T}}{dt} - \frac{q.\nabla T}{T} \geq \ 0 \tag{3.48}$$

And

$$\sigma - \ \rho\frac{\delta\Psi}{\delta\varepsilon^{el}} = 0 \tag{3.49}$$

$$\frac{\delta\Psi}{\delta T}+s_{en}=0 \tag{3.50}$$

So insertion of equation (3.46), (3.49) and (3.50) simplifies the equation (3.48) to:

$$\left(\rho T\frac{ds_{en}}{dt}\right)+\sigma:\dot{\varepsilon}^{pl}-A_{\alpha}:\dot{\alpha}+div(q)=0 \tag{3.51}$$

Or

$$\frac{ds_{en}}{dt}=\frac{\delta\Psi}{\delta\varepsilon^{el}}:\dot{\varepsilon}+\frac{\delta\Psi}{\delta\alpha}:\dot{\alpha}+\frac{\delta\Psi}{\delta T}\dot{T} \tag{3.52}$$

$$=-\frac{1}{\rho}\frac{\delta\alpha}{\delta T}:\dot{\varepsilon}-\frac{1}{\rho}\frac{\delta A_{\alpha}}{\delta T}:\dot{\alpha}+\frac{1}{\rho}\frac{\delta s_{en}}{\delta T}\dot{T} \tag{3.53}$$

As the specific heat 'c' is defined as:

$$c=T\frac{\delta s_{en}}{\delta T} \tag{3.54}$$

The heat equation can be derived from substituting the equation (3.53) into (3.51):

$$\rho c\frac{d\mathrm{T}}{dt}=\sigma:\dot{\varepsilon}^{pl}-A_{\alpha}:\dot{\alpha}+div(K_{k}\nabla T)+T\left(\frac{\delta\alpha}{\delta T}:\dot{\varepsilon}^{el}+\frac{\delta A_{\alpha}}{\delta T}:\dot{\alpha}\right) \tag{3.55}$$

Since the effect of the internal state variables is considered negligible to the plastic dissipation energy, the equation (3.55) is simplified by removing the last term on the right hand side. Therefore, the heat equation for the plastic or viscoplastic material deformation is presented as:

$$\rho c\frac{d\mathrm{T}}{dt}=\sigma:\dot{\varepsilon}^{pl}+div(K_{k}\nabla T) \tag{3.56}$$

3.3. Fully coupled thermal structural analysis

The FSW process involves highly complex thermomechanical interactions [3.32,3.33]. The stress solution in the workpiece is dependent on the temperature distribution, and vice versa. Therefore, a fully coupled thermal stress analysis is required to calculate the thermal and the structural response of the model, simultaneously. The body force at a node 'f' can be expressed as [3.29]:

$$f=F-\rho\ddot{u} \tag{3.57}$$

Where 'F' is an externally prescribed body force, and '$\ddot{u}$' is the acceleration of that node. The material's structural response in the virtual work equation is:

$$\int_V f.\delta v dV = \int_V F.\delta v dV - \int_V \rho\ddot{u}.\delta v dV \tag{3.58}$$

The second term in the equation (3.58), known as d'Alembert force, can be presented in terms of the reference volume and density as:

$$\int_{V_o} \rho_o \ddot{u}.\delta v dV_o \tag{3.59}$$

And $u = N^N u^N$, so that $\ddot{u} = N^N \ddot{u}^N$, where '$N^N$' is the shape function. Therefore, the equation (3.59) becomes:

$$\left(\int_{V_o} \rho_o N^N.N^M dV_o\right)\ddot{u}^M \tag{3.60}$$

This is the consistent mass matrix multiplied with the accelerations of the nodal variables. The finite element approximations to equilibrium is:

$$M^{NM}\ddot{u}^M + I^N - P^N = 0 \tag{3.61}$$

Where M^{NM}, I^N and P^N are consistent mass matrix, internal force vector and the external force vector, respectively [3.29].

$$M^{NM} = \int_{V_o} \rho_o N^N.N^M dV_o \tag{3.62}$$

$$I^N = \int_{V_o} \beta^N : \sigma dV_o \tag{3.63}$$

$$P^N = \int_S N^N.tdS + \int_V N^N.FdV \tag{3.64}$$

The terms 'matrix' and 'vector' contributes to the matrices and vectors in the space of nodal variables 'u^N'. For the thermal response, the discretised heat equation (3.9) in the matrix form for three dimensional element becomes [3.11]:

$$C\dot{T} + K_T T = S_T \tag{3.65}$$

Where

$K_T = K_k + H_c$ Conductivity and boundary convection matrix

$S_T = S_B + S_h{+}S_Q$	Heat source vector containing all thermal sources
$C = \int_V N^N N.\rho c dV$	Heat capacity matrix
$K_k = \int_V B^T K B dV$	Conductivity matrix
$H_c = \int_S N^T h_{fc} dS$	Boundary convection matrix, 'h_{fc}' is the convective film coefficient
$S_B = \int_S N q_B dS$	Boundary heat flux vector, 'q_B' is boundary heat flux
$S_h = \int_S N^T h_f T dS$	Boundary convection vector
$S_Q = \int_V N^T \sigma : \dot{\varepsilon}^{pl} dV$	Heat generation vector

To solve the above-mentioned structural and thermal equations, there are two categories of dynamic integration operators; Implicit and Explicit. Explicit scheme finds the values for the dynamic variables based on the already known quantities. Whereas in the implicit scheme, the dependent variables are calculated by a set of already known quantities along with a matrix or iterative technique.

3.3.1. Implicit scheme

For the nonlinear problems, a solution is obtained by performing several iterations in the implicit scheme on each time increment. Each iteration includes a correction factor 'c_i', to the incremental displacement 'Δu' from the equation (3.66) [3.11].

$$\widehat{K} c_i = F - f - \rho \ddot{u} \qquad (3.66)$$

Where '$\widehat{K}$' is the effective stiffness matrix, obtained from the linear combination of the tangent stiffness matrices. Since the thermal and structural solutions should be obtained in the coupled thermal structural analysis as concurrently rather than serially, the nonlinear coupled behavior of the FSW process can be solved by the 'Newton's method' [3.11]. As the Abaqus software neglects the initial effects for the coupled thermal stress analysis, the mass matrix is regarded as zero, and the remaining terms are represented as 'P_M'.

$$\begin{bmatrix} \frac{\delta P_M}{\delta u} & \frac{\delta P_M}{\delta T} \\ \frac{\delta P_H}{\delta u} & \frac{\delta P_H}{\delta T} \end{bmatrix} \begin{bmatrix} c_M \\ c_H \end{bmatrix} = \begin{bmatrix} R_M \\ R_H \end{bmatrix} \tag{3.67}$$

Where '$\frac{\delta P_M}{\delta T}$' is the mechanical coupling on the temperature distribution, and '$\frac{\delta P_H}{\delta T}$' is the thermal coupling on the mechanical formulation. 'c_M' and 'c_H' are the corrections for the incremental displacement and temperature, respectively. 'R_M' and 'R_H' are the respective mechanical and thermal residual vectors. Implicit scheme includes larger time increments as compared to the explicit scheme, but the computational cost for obtaining the solution in each increment is relatively higher than the explicit scheme.

3.3.2. Explicit scheme

The explicit scheme calculates the values for the dynamic variables at '$t + \Delta t$' based on the available values at the time 't'. It is based on the application of an explicit integration rule along with the use of lumped element mass matrices [3.29]. Due to the unavailability of the model's inertial effects when using the implicit analysis, explicit analysis is applied to model a fully coupled thermomechanical FSW model.

The structural solution response is obtained by integrating the equation (3.57) with the application of the explicit central difference integration rule [3.34]. A lumped mass matrix is also applied together with the explicit integration rule in equation (3.68):

$$\mathrm{N}_{(\mathrm{i}+\frac{1}{2})} = \dot{\mathrm{u}}^{\mathrm{N}}_{(\mathrm{i}-\frac{1}{2})} + \frac{\Delta \mathrm{t}_{(\mathrm{i}+1)} + \Delta \mathrm{t}_{(\mathrm{i})}}{2} \ddot{\mathrm{u}}^{\mathrm{N}}_{(\mathrm{i})} \tag{3.68}$$

$$\mathrm{u}^{\mathrm{N}}_{(\mathrm{i}+1)} = \mathrm{u}^{\mathrm{N}}_{(\mathrm{i})} + \Delta \mathrm{t}_{(\mathrm{i}+1)} \dot{\mathrm{u}}^{\mathrm{N}}_{(\mathrm{i}+\frac{1}{2})} \tag{3.69}$$

Here, 'u^{N}' represents either a displacement or rotational component with 'i' number of increments in the explicit dynamic step, and 'N' is a node under consideration. The kinetic state uses known values of '$\dot{\mathrm{u}}^{\mathrm{N}}_{(\mathrm{i}-\frac{1}{2})}$' and '$\ddot{\mathrm{u}}^{\mathrm{N}}_{(\mathrm{i})}$' from the previous increment. The heat transfer in the model is achieved through integrating the equation (3.65) and applying the explicit forward difference time integration rule [3.35]:

$$\mathrm{T}^{\mathrm{N}}_{(\mathrm{i}+1)} = \mathrm{T}^{\mathrm{N}}_{(\mathrm{i})} + \Delta \mathrm{t}_{(\mathrm{i}+1)} \mathrm{T}^{\mathrm{N}}_{(\mathrm{i})} \tag{3.70}$$

Where 'T^{N}' refers to the temperature at a specific node 'N' with 'i' number of increments in the explicit dynamic step, and '$\dot{\mathrm{T}}_{(\mathrm{i})}^{\mathrm{N}}$' denotes the current temperature value as calculated from the previous increment. For the beginning of the increment, its value is computed by:

$$\dot{\mathrm{T}}_{(\mathrm{i})}^{\mathrm{N}} = (\mathrm{C}^{\mathrm{NJ}})^{-1}(\mathrm{P}_{(\mathrm{i})}^{\mathrm{J}} - \mathrm{F}_{(\mathrm{i})}^{\mathrm{J}}) \tag{3.71}$$

Where, C^{NJ} is the lumped capacitance matrix, P^{J} is the applied nodal source and F^{J} is the internal flux vector.

In an explicit analysis, the equations are solved for the acceleration rather than the displacement like implicit analysis. This allows bypassing the inversion of the body's stiffness matrix, therefore only inverting the mass matrix, hence increasing the computational efficiency of the whole model. However, the solution is generally very unstable, which requires smaller time steps for the accurate results.

3.4. References

[3.1] Szabo B, Babuska I. Finite element analysis. New York: Wiley; 1991.

[3.2] Quarteroni A. Domain decomposition methods. Numer. Model. Differ. Probl., Milano: Springer Milan; 2014, p. 527–84. doi:10.1007/978-88-470-5522-3_18.

[3.3] Gottlieb D, Gottlieb S. Spectral methods. Scholarpedia 2009;4:7504. doi:10.4249/scholarpedia.7504.

[3.4] Rao SS. The Finite Element Method in Engineering. 3rd ed. Elsevier Science & Technology; 1998.

[3.5] Mishra RS, De PS, Kumar N. Fundamentals of the Friction Stir Process. Frict. Stir Weld. Process., 2014, p. 13–58. doi:10.1007/978-3-319-07043-8_2.

[3.6] Al-Moussawi M, Smith A, Young AE, Cater S, Faraji M. An advanced numerical model of friction stir welding of DH36 steel. 11th Int. Symp. Frict. Stir Welding, TWI, Cambridge: 2016.

[3.7] Hirt CW, Nichols BD. Volume of Fluid (VOF) Method for the Dynamics of Free Boundaries. J Comput Phys 1981;39:201–25. doi:10.1016/0021-9991(81)90145-5.

[3.8] Rider WJ, Kothe DB. Reconstructing Volume Tracking. J Comput Phys 1998;141:112–52. doi:10.1006/jcph.1998.5906.

[3.9] Guerdoux S, Fourment L, Miles M, Sorensen C. Numerical Simulation of the Friction Stir Welding Process Using both Lagrangian and Arbitrary Lagrangian Eulerian Formulations. Aip Conf Proc 2004;712:1259–64. doi:10.1063/1.1766702.

[3.10] Schmidt H, Hattel J. A local model for the thermomechanical conditions in friction stir welding. Model Simul Mater Sci Eng 2005;13:77–93. doi:10.1088/0965-0393/13/1/006.

[3.11] Li H. Coupled Thermo-Mechanical Modelling of Friction Stir Welding. University of Strathclyde, 2008.

[3.12] Dialami N, Chiumenti M, Cervera M, Saracibar CAD. Challenges in Thermo-mechanical Analysis of Friction Stir Welding Processes. Arch. Comput. Methods Eng., vol. 24, 2017, p. 189–225. doi:10.1007/s11831-015-9163-y.

[3.13] Donea J, Huerta A, Ponthot J-P, Rodriguez-Ferran A. Arbitrary Lagrangian-Eulerian Methods. Encycl. Comput. Mech., 2004, p. 1–25. doi:10.1002/0470091355.ecm009.

[3.14] Hallquist JO. LS-DYNA® Theory Manual. 2006.

[3.15] Parvizian F, Kayser T, Hortig C, Svendsen B. Thermomechanical modeling and simulation of aluminum alloy behavior during extrusion and cooling. J Mater Process Technol 2009;209:876–83. doi:10.1016/j.jmatprotec.2008.02.076.

[3.16] Anderson RW, Elliott NS, Pember RB. An arbitrary Lagrangian-Eulerian method with adaptive mesh refinement for the solution of the Euler equations. J Comput Phys 2004;199:598–617. doi:10.1016/j.jcp.2004.02.021.

[3.17] Hirt CW, Amsden AA, Cook JL. An Arbitrary Lagrangian-Eulerian Computing Method for All Flow Speeds. J Comput Phys 1974;14:227–53. doi:10.1016/0021-9991(74)90051-5.

[3.18] Noh WF. CEL: A time dependent, two space dimensional, Coupled Eulerian Lagrange code. 1963.

[3.19] Brown KH, Burns SP, Christon MA. Coupled Eulerian-Lagrangian Methods for Earth Penetrating Weapon Applications 2002. doi:10.2172/808588.

[3.20] Benson DJ. Computational methods in Lagrangian and Eulerian hydrocodes. Comput Methods Appl Mech Eng 1992;99:235–394. doi:10.1016/0045-7825(92)90042-I.

[3.21] Mougeotte C, Carlucci P, Recchia S, Ji H. Novel Approach to Conducting Blast Load Analyses Using Abaqus/Explicit-CEL. 2010.

[3.22] Smojver I, Ivančević D. Bird strike damage analysis in aircraft structures using Abaqus/Explicit and coupled Eulerian Lagrangian approach. Compos Sci Technol 2011;71:489–98. doi:10.1016/j.compscitech.2010.12.024.

[3.23] Al-Badour F, Merah N, Shuaib A, Bazoune A. Coupled Eulerian Lagrangian finite element modeling of friction stir welding processes. J Mater Process Technol 2013;213:1433–9. doi:10.1016/j.jmatprotec.2013.02.014.

[3.24] Hossfeld M. A fully coupled thermomechanical 3D model for all phases of friction stir welding. 11th Int. Symp. Frict. Stir Weld., Cambridge: 2016. doi:10.18419/opus-8845.

[3.25] Simar A, Bréchet Y, De Meester B, Denquin A, Gallais C, Pardoen T. Integrated modeling of friction stir welding of 6xxx series Al alloys: Process, microstructure and properties. Prog Mater Sci 2012;57:95–183. doi:10.1016/j.pmatsci.2011.05.003.

[3.26] Rajput RK. Engineering Thermodynamics. 2007.

[3.27] Logan DL. A first course in the finite element method. 6th ed. Boston, MA : Cengage Learning; 2016.

[3.28] Zienkiewicz OC, Taylor RL. The finite element method Volume 2: Solid Mechanics. 5th ed. Boston : Butterworth-Heinemann; 2000.

[3.29] Abaqus theory manual. 2007.

[3.30] Simulia 6.14. Abaqus Documentation. 23.2.1 Classical Metal Plasticity. 2014.

[3.31] Simulia 6.14. Abaqus Documentation. 23.2.3 Rate-Dependent Yield. 2014.

[3.32] Hossfeld M, Roos E. A new approach to modelling friction stir welding using the CEL method. Int. Conf. Adv. Manuf. Eng. Technol. NEWTECH, Stockholm: 2013, p. 179–90. doi:10.18419/opus-8825.

[3.33] Meshram AD, Yarasu RB. Finite Element Modeling of Friction Stir Welding-Thermal Analysis. Int J Sci Res Dev 2014;3:784–7.

[3.34] Simulia 6.14. Abaqus Documentation. 6.3.3 Explicit Dynamic Analysis. 2014.

[3.35] Simulia 6.14. Abaqus Documentation. 6.5.3 Fully Coupled Thermal-stress Analysis. 2014.

4. FSW thermomechanical model

This chapter describes the thermomechanical modelling of the friction stir welding (FSW) process on structural steel. The model geometries, boundary conditions, configurations and process parameters along with materials properties will be thoroughly discussed. Unlike any previously published research on the modelling of the FSW process, in which either the workpiece is assumed as a highly viscous body or the tool is modelled as a moving heat source, the Coupled Eulerian Lagrangian (CEL) approach has been applied to model the FSW process on steel. All stages of the FSW process (plunge, dwell and traverse) have been modelled in the present work for diverse process parameters and their results compared with previous experimental work on the same grade of steel. Real time temperature dependent material properties have been applied in the present model, as discussed in section 2.2.3. The majority of the numerical results will be discussed and validated by the experimental results obtained by Toumpis et al. [4.1] on the same grade of steel and process conditions.

4.1. Model description

A three-dimensional finite element model has been developed and solved, using Abaqus/Explicit V2017. The CEL approach has been applied to predict the temperature distribution, plastic strain and the material flow in the workpiece, and the reaction forces on the tool along with the visualisation of the flash produced on the workpiece surface during the FSW process. Since the FSW tool has negligible deformation as compared to the workpiece during the welding, the workpiece was modelled as an Eulerian body while the tool was modelled as a Lagrangian body (Figure 4.1). The tool Lagrangian domain was meshed with 6072 thermally coupled 8-node brick elements C3D8RT while the workpiece Eulerian domain was meshed with 25192 thermally coupled 8-node Eulerian elements EC3D8RT. The Eulerian body included two regions, ‘full’ and ‘void’. The outer region ‘void’ contained no initial DH36 material properties while the inner region ‘full’ was assigned with the DH36 workpiece material properties. Parts of the numerical results have been validated by previously published experimental results. The experimental results have been produced by using a FSW pcBN tool and 6 mm thick DH36 workpiece [4.1]. A number of macrographs from these experiments have been published in earlier work [4.1] and are also used herein.

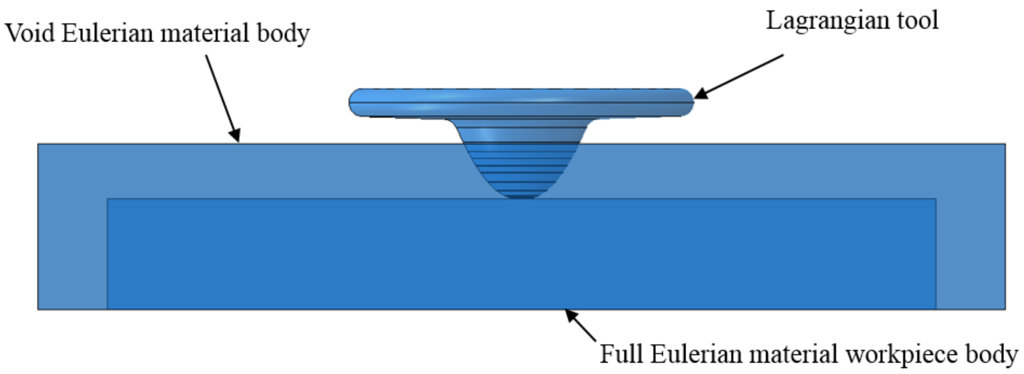

Figure 4.1: Illustration of the CEL approach with the material assignment.

4.1.1. Material properties

To understand the FSW process, consideration of the workpiece material's behaviour under stress, primarily at a range of temperatures and strain rates is crucial to improve the numerical results as compared to the experimental data [4.2]. As an increase in temperature changes the material properties, using such material properties that are independently calculated from the temperature will give inaccurate results. The commonly applied Johnson Cook's (JC) material model for aluminium FSW could not be applied for steel modelling, as discussed in section 2.2.3. Therefore, the current FSW model contains temperature dependent material properties of the workpiece to predict results that are more accurate. All of the DH36 properties were experimentally derived by the same research group [4.2-4.4]. The chemical composition of DH36 studied previously [4.1] is presented in Table 4.1.

Table 4.1: Chemical composition of DH36, wt.% [4.1].

C	Mn	Si	P	S	Al	Nb	N	Fe
0.11	1.48	0.37	0.014	0.004	0.02	0.02	0.002	<97.98

Temperature dependent material properties such as the coefficient of thermal expansion, thermal conductivity and specific heat capacity were used from previous literature [4.4] to acquire realistic results, and are shown in Table 4.2. The spike in the specific heat capacity at 700°C is associated with the characteristic phase change within the steel alloy. This typical behaviour is a result of the dual phase microstructure of ferrite and austenite that evolves at that temperature. Density was kept constant at 7830 $\mathrm{kg.m^{-3}}$ since changing the temperature has a negligible effect on density.

Table 4.2: Temperature dependent properties of DH36 steel [4.4].

Temperature ($^\circ\mathrm{C}$)	Coefficient of thermal expansion ($\mathrm{K^{-1}}$)	Thermal conductivity (W/(m.K))	Specific heat capacity (J/(kg.K))
25	9.80 x 10^{-6}	31.943	306.44
100	1.13 x 10^{-5}	37.043	375.99
200	1.26 x 10^{-5}	36.615	405.02
300	1.34 x 10^{-5}	32.594	403.96
400	1.41 x 10^{-5}	28.961	407.74
500	1.47 x 10^{-5}	25.298	415.54
600	1.50 x 10^{-5}	21.973	440.6
700	1.51 x 10^{-5}	18.874	520.8
800	1.36 x 10^{-5}	21.15	499.16
900	1.21 x 10^{-5}	10.21	216.01
1000	1.31 x 10^{-5}	8.061	167.1
1100	1.39 x 10^{-5}	6.53	128.13
1200	1.45 x 10^{-5}	3.517	67.149

To observe the viscoplastic behaviour of DH36, thermoplastic properties such as yield stress, strain and strain rates were fed into the model. Stress and strain was recorded over different temperature and strain rate points. The yield stress $\overline{\sigma}$ of DH36 steel's is dependent on the plastic deformation which has been represented as a function of equivalent plastic strain $\overline{\varepsilon}^{\mathrm{pl}}$, inelastic strain rate $\dot{\varepsilon}^{\mathrm{pl}}$ and temperature T for this specific model as shown in equation (4.1) [4.5].

$$\overline{\sigma} = \overline{\sigma}(\overline{\varepsilon}^{\mathrm{pl}}, \dot{\varepsilon}^{\mathrm{pl}}, \mathrm{T}) \tag{4.1}$$

The strain rate and temperature dependent flow stress of the workpiece (DH36) was obtained from previous work [4.2], in which 58 uniaxial compression tests were performed on a Gleeble 3800 thermomechanical testing system. Stress and strain was experimentally measured with a wide range of strain rates from $10^{-2}\ s^{-1}$ to 100 s^{-1} and temperature change from 700°C to 1100°C. It was reported that material flow below 700°C and with a low strain rate was found to be essentially insignificant [4.2]. A typical true stress versus strain curve is shown in Figure 4.2 as a function of strain rates of 0.1, 1, 10 and 50 s^{-1} at 900°C.

Yield strength values were calculated by an approach known as '0.2% offset yield strength' from the graphs extracted from previous experimental data [4.2] with different temperature and strain rates, and are listed in Table 4.3. Young's modulus values were calculated for all stress-strain curves by taking the slope of the line in the elastic region. All material data was acquired from a previous research project named HILDA (High Integrity Low Distortion Assembly) [4.2-4.4]. Material's thermal conductivity, specific heat capacity and density were used for the pcBN tool and are shown in Table 4.4 [4.6].

Table 4.3: Temperature dependent yield stress, strain and strain rates of DH36 steel [4.2].

Temperature (℃)	Strain rate (s^{-1})	Yield Stress (MPa)	Strain
700	0.001	93	0.022
700	0.01	116	0.016
750	0.001	63	0.01
750	0.01	94	0.017
800	0.01	95	0.017
800	0.1	105	0.021
850	0.01	84	0.02
850	0.1	92	0.019
850	1	105	0.018
900	0.1	87	0.022
900	1	87	0.012
900	10	107	0.013
900	50	109	0.012
950	1	81	0.016
950	10	95	0.014

950	50	108	0.012
950	100	110	0.016
1000	10	91	0.014
1000	50	95	0.011
1000	100	103	0.014
1100	10	64	0.01
1100	50	60	0.006
1100	100	77	0.012

Table 4.4: Material properties of the pcBN tool [4.6].

Thermal conductivity (W/(m.K))	Coefficient of thermal expansion (10E-6 /°C)	Density (kg.m³)	Specific heat capacity (J/(kg.K))	Young’s modulus (N/m²)
150	4.7	4370	750	7.50E+11

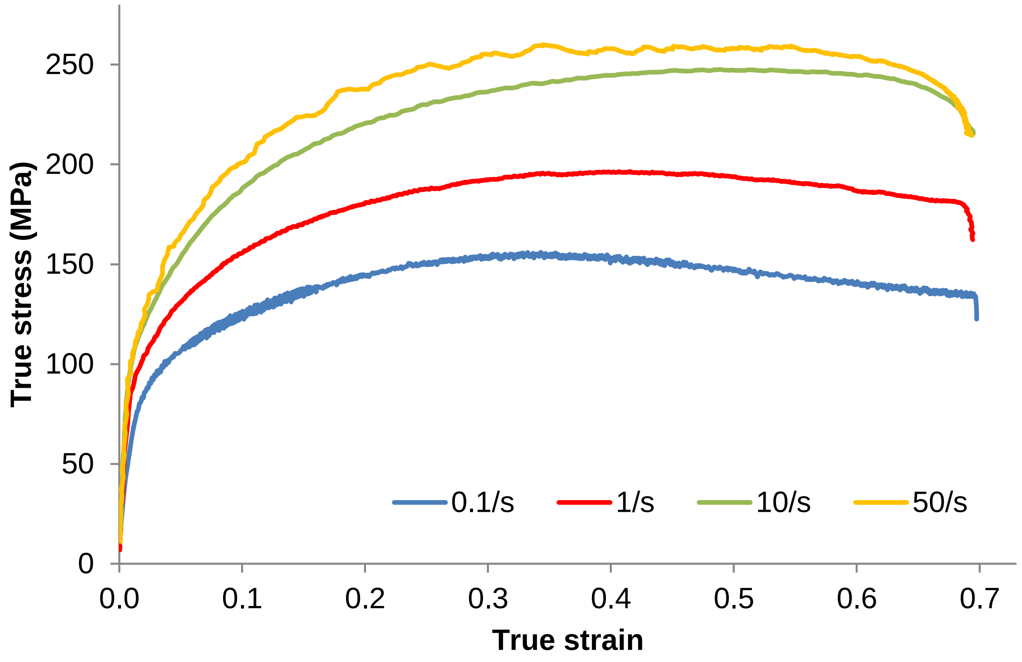

Figure 4.2: True stress vs strain curve at 900°C [4.2].

4.1.2. Model geometry

The geometrical dimensions of the FSW tool for steel have been taken from the relevant technical literature [4.1,4.6]. The tool's dimensions are shown in Figure 4.3. It is made up of three parts, i.e. pcBN probe and shoulder, tungsten carbide shank and two steel collars which hold the shank and shoulder to avoid any horizontal or vertical movement.

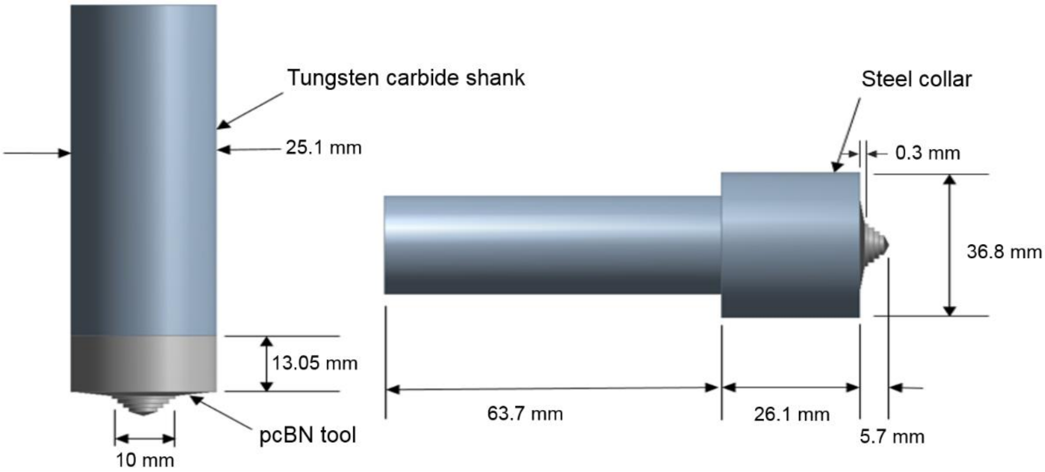

Figure 4.3: FSW tool geometrical dimensions [4.1,4.6].

To reduce the computational time, the tool was simplified by ignoring the spiral threads on the shoulder and probe while keeping the overall dimensions the same, as shown in Figure 4.4. The workpiece modelled in this study was an 8 mm thick DH36 plate with 100 mm length and 60 mm width. The length and width of the welded workpiece from the experiments, with which the numerical results are compared, were 2000 mm and 400 mm respectively [4.1].

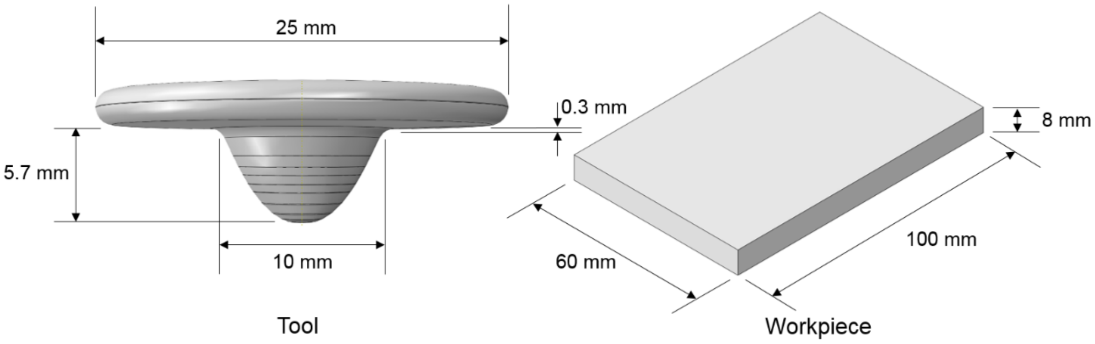

Figure 4.4: Simplified tool and workpiece geometrical dimensions.

4.1.3. Process parameters

Numerous process parameters of FSW were modelled; however, two diverse but indicative sets of process parameters have been discussed in this chapter. The two selected models represent the two extremes in terms of traverse and rotational speed thereby allowing for a distinct comparison of results. Table 4.5 presents different properties for each stage of the model. The model simulation included three stages: plunge, dwell and traverse.

Table 4.5: Process parameters for models used in the study.

	Plunge stage		Dwell stage	Traverse stage	
	Rotational speed (rpm)	Feed rate in downward direction (mm/min)	Rotational speed (rpm)	Rotational speed (rpm)	Traverse speed (mm/min)
Slow weld model	700	100	400	200	120
Fast weld model	800	100	700	700	500

The position control method has been applied in the current model to achieve an accurate tool probe depth and to maintain consistency with the previous experimental work [4.1]. When the tool reached its maximum depth, it was maintained as rotating at the required rotational speed for 4 seconds to generate enough heat. Once the surrounding material was softened enough, the tool was traversed, thereby welding the workpiece with the provided traverse and rotational speed.

4.1.4. Boundary conditions

The coefficient of friction is a significant factor in calculating the heat generation between two surfaces. Several researchers have estimated different values for various material interactions under specific conditions [4.7-4.9]. Nandan et al. [4.7] computed the friction coefficient by considering the relative velocity between the tungsten based rotating tool and 304 stainless steel workpiece and used a value of

0.4. Furthermore, Ambroziak et al. [4.8] determined the friction coefficient ‘μ’ for steel S235 from the equation (4.2):

$$\mu = \frac{M_t}{r.P_t} \tag{4.2}$$

Where M_t refers to the friction torque in Nm, P_t is the ‘pressure force’ in N and r is the radius of the cylindrical welded specimen, considered as 8 mm in the study [4.8]. It was concluded that the friction coefficient was maximised in the low temperature range and was stabilised at 0.3 after reaching above 400°C. The value of the friction coefficient slightly decreased with increasing temperature [4.8]. Moreover, it was also concluded by Assidi et al. [4.9] that an accurate calibration could be obtained by setting the value of μ as 0.3. As a consequence, a constant friction coefficient value of 0.3 has been used in this study for both weld models. An ‘all with self’ setting has been applied in Abaqus through ‘general contact’ configuration.

The heat transfer between the contact surfaces is assumed to be defined by:

$$q = h(\theta_A - \theta_B) + (\varepsilon\alpha(\theta_A{}^4 - \theta_B{}^4)) \tag{4.3}$$

Where q is the heat flux per unit area in $W.m^{-2}$, h is the convective coefficient in $W.m^{-2}.K$, ε is the emissivity coefficient, α is the Stefan-Boltzmann Constant (5.6703 x 10^{-8} $W.m^{-2}.K^{-4}$) and θ is the temperature value from point A on one surface to point B on the other. Radiative heat transfer has been compensated by increasing the conductivity on the workpiece surfaces to avoid complexities in the model. Therefore, the top and side surfaces of the workpiece have been assigned an increased convective film coefficient of 10 $W.m^{-2}.K^{-1}$. Al-Moussawi et al. [4.10] used a computational fluid dynamics (CFD) model to represent material flow in DH36 steel. It was suggested that a convective film coefficient value of 2000 ($W.m^{-2}.K^{-1}$) on the bottom surface of the workpiece was suitable to achieve realistic results [4.12]. Hence, the same value has been applied on the bottom surface of the workpiece in the present study to represent the influence of the backing plate. The initial temperature of the workpiece has been kept as 25°C.

Structural and thermal boundary conditions have been applied on the model. The workpiece has been fully constrained from the bottom surface for the entire process. Gap conductance has been applied to minimise the mesh irregularity effects on the contact surfaces between the tool and the workpiece.

4.1.5. Heat generation

For the thermomechanically coupled surface interactions, the frictional energy dissipation rate in the model is calculated through the following expression [4.11]:

$$\dot{P}_{fr} = \tau . \dot{\gamma} \tag{4.4}$$

Where τ represents the frictional stress and $\dot{\gamma}$ is the slip rate between two surfaces. The total amount the heat energy released on each surface is given by

$$q_A = f\eta\dot{P}_{fr} \tag{4.5}$$

$$q_B = (1 - f)\eta\dot{P}_{fr} \tag{4.6}$$

Where η is the fraction of dissipated energy converted into heat, f is the amount of heat distributed into the surface of the contact pair which is the workpiece for this model and q_A represents the heat flux into the workpiece, while q_B denotes the heat flux into the tool. All energy generated by friction was converted into heat while 90% of the converted heat was assumed to be transferred into the workpiece [4.12].

4.1.6. Meshing

Mesh plays an important role in the numerical modelling. A coarser mesh can give inaccurate results whereas a finer mesh can significantly increase the computational cost of the simulation.

4.1.6.1 Element type

The element library of the Abaqus/Explicit offers only one element type for 3D linear geometric order; EC3D8RT. It is an 8-node thermally coupled linear Eulerian brick element which has temperature and displacement nodal variables at all eight nodes. To decrease the computational time, a reduced integration scheme has been used. Instead of using all nodes in the element, this scheme incorporates a single point in the centroid of the element to form the element stiffness. Therefore, the Eulerian workpiece is modelled with the thermally coupled element type EC3D8RT. The geometry of the EC3D8RT has been shown in Figure 4.5 along with the nodal and integration point locations.

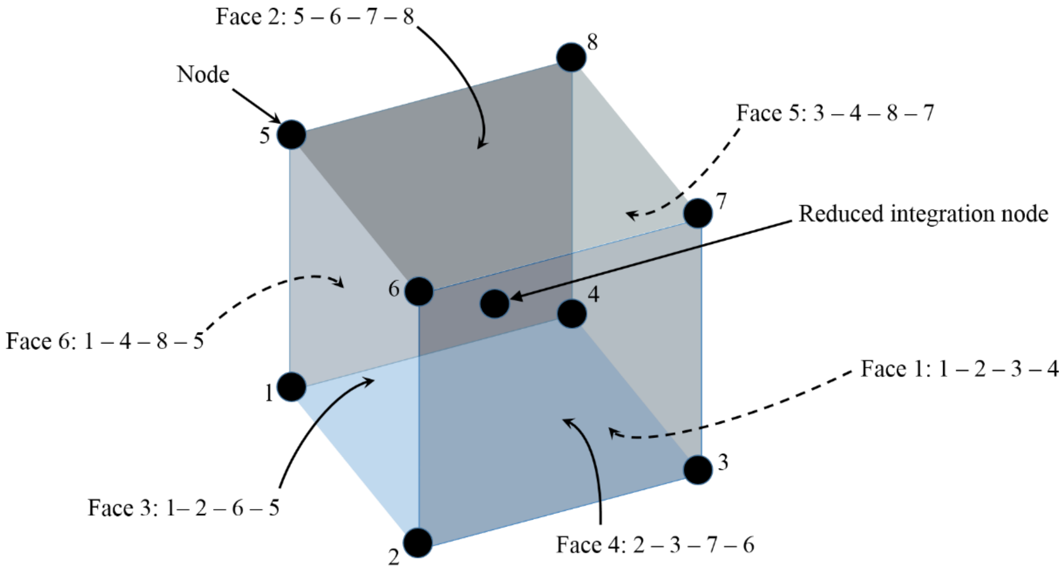

Figure 4.5: Element type EC3D8RT geometry.

Since the tool is modelled as a Lagrangian part, the element type C3D8RT has been used. This element is similar to the Eulerian element in nature, discussed in section 2.2.2.4, as it also consists of an 8-node thermally coupled linear brick element. In addition, it also includes a trilinear displacement and temperature method due to the complex geometry of the tool. Since the current study is restricted for the results relating to the workpiece only, the tool has been assumed as a rigid body and all surfaces of the tool have been constrained as isothermal. Note that this option is provided for the coupled thermal-stress analysis only.

4.1.6.2. Mesh size

In the CEL approach, the mesh dimensions do not critically change as the material can move easily in the mesh due to the coupled Eulerian-Lagrangian technique. Therefore, an adaptive mesh domain was not used for any specific localised region in the workpiece near the tool.

Initially, an element size of 3 mm was selected to reduce the numerical calculations, hence decreasing the simulation time. However, due to the inconsistency between the tool and workpiece's mesh, the mesh size was decreased to 1.5 mm to achieve a uniform contact between tool and workpiece surfaces as shown in Figure 4.6.

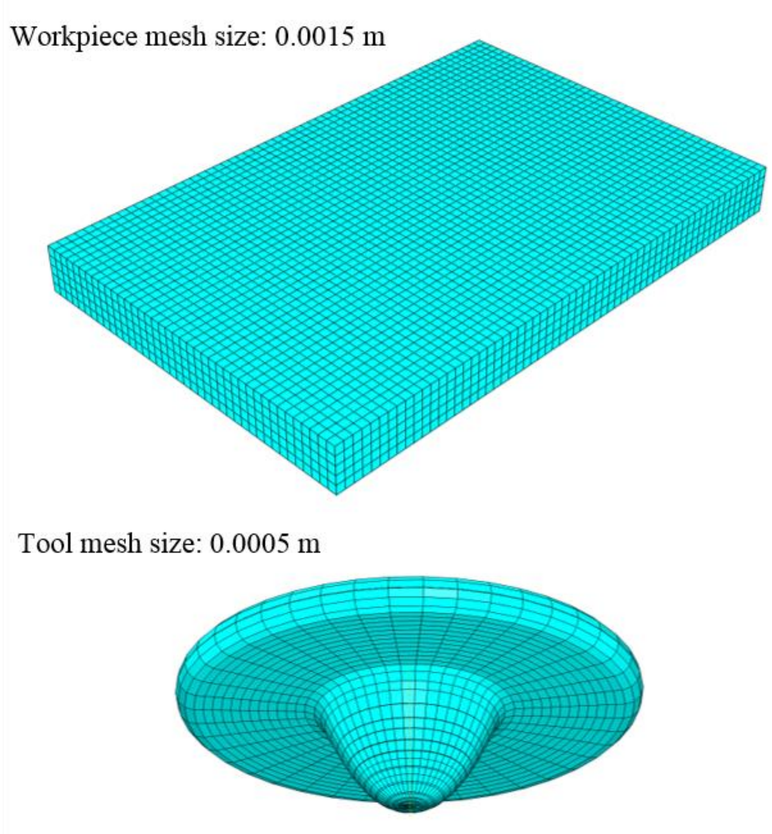

Figure 4.6: Element sizes of the workpiece and the tool used in all models.

4.1.7. Material movement

In the CEL approach, the Eulerian implementation is based on the volume-of-fluid (VOF) method. This methodology describes the tracking of the material as it moves through the mesh within each element [4.13]. By using this approach, the material movement inside the mesh can be traced through naming a set of nodes in the workpiece. These sets are primarily known as tracer particles in Abaqus. Tracer particles can be used to obtain an output at specific material points that may not correspond to a fixed location in the mesh if an Eulerian mesh is used. Tracer particles follow the material motion throughout an analysis regardless of the mesh motion, which makes them ideal for use with the CEL approach, hence assisting in tracking the material flow during the FSW process. Both nodal and element outputs can be obtained at tracer particles. For the CEL analysis, the output for the tracer particles can be implemented in Abaqus with version 2016 and later.

The initial location of each tracer particle coincides with the mesh node, often known as the ‘parent node’. These parent nodes are then grouped into a tracer set. In the

Eulerian analysis, the parent nodes are grouped into the same tracer set, as the connected elements must belong to the same Eulerian section. Four sets of tracer particles have been defined in the workpiece to observe the material movement behaviour during the plunge, dwell and traverse stages. Figure 4.7 demonstrates the initial locations of both tracer sets in the workpiece.

There are two types of outputs which can be obtained for tracer particles:

1. Field output

2. History output

In the field output, only displacement can be requested in the results whereas in the history output, velocity and acceleration can also be obtained along with the displacement on the applied integration point.

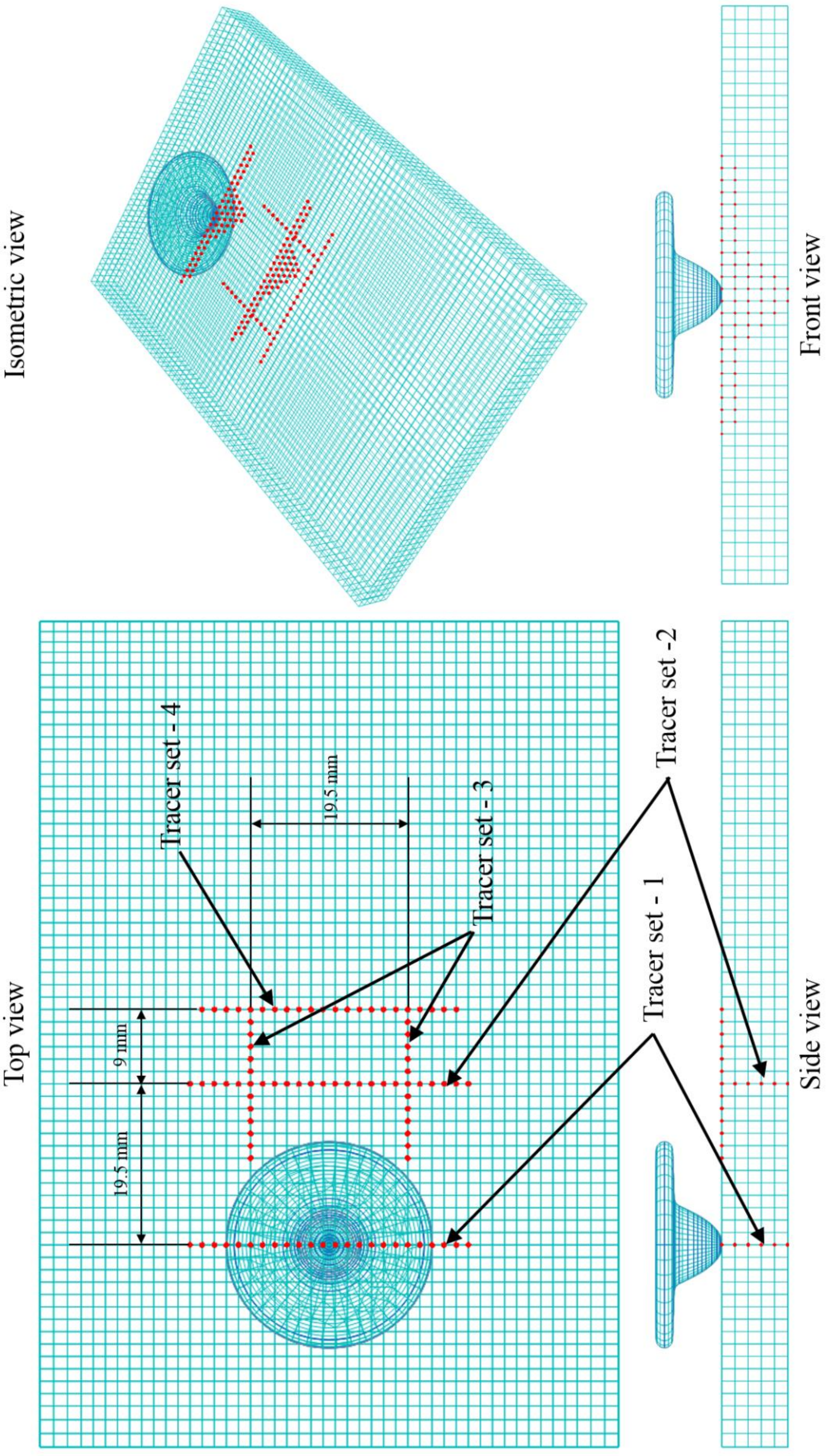

Figure 4.7: Initial locations of the tracer particle sets in both models.

4.1.8. Additional analysis options

4.1.8.1. Bulk viscosity

In the case of high-speed dynamic simulations such as the FSW process, unrequired vibrations are often present in the numerical analysis. These vibrations, also known as the ringing effect, can be avoided by including a parameter known as the bulk viscosity. Bulk viscosity introduces damping in the model linked with the volumetric straining. Abaqus/Explicit offers two forms of bulk viscosity [4.14]:

1. Linear bulk viscosity
2. Quadratic bulk viscosity

The linear bulk viscosity is present in all elements by default, which suppresses the ringing effect in the highest element frequency, also known as the truncation frequency damping [4.14]. It generates a bulk viscosity pressure 'p_{bv}', which is directly proportional to the volumetric strain rate $\dot{\varepsilon}_{vol}$ expressed in the following equation:

$$p_{bv1} = b_1 \rho c_d L_e \dot{\varepsilon}_{vol} \tag{4.7}$$

Where b_1 is a damping coefficient, ρ is the density of the material (set as 7830 $\mathrm{kg.m^{-3}}$ in the current study), c_d refers to the dilatational wave speed in the current step increment, L_e is the element's characteristic length (1.5 mm for the workpiece in all models).

The second form of bulk viscosity is calculated by including volume strain rate as in the quadratic expression:

$$p_{bv2} = \rho (b_2 L_e \dot{\varepsilon}_{vol})^2 \tag{4.8}$$

Where b_2 is the second damping coefficient. When under extremely high velocity gradients, the quadratic bulk viscosity pressure avoids elements to collapse. Quadratic bulk viscosity is activated only if the volumetric strain rate is compressive.

The bulk viscosity pressures are not used directly in the material point stresses, as they are not taken as a part of the constitutive response of the material. Therefore, a fraction of critical damping ξ is considered in the dilatational mode, instead of the bulk viscosity pressures, and is expressed as:

$$\xi = b_1 - b_2{}^2 \frac{L_e}{c_d} min(0, \dot{\varepsilon}_{vol}) \tag{4.9}$$

A default value of $b_1 = 0.06$ and $b_2 = 1.2$ have been used in the current models. These values neutralise the ringing effect in the FSW model, hence providing accurate numerical results.

4.1.8.2. Stable increment estimator

In Abaqus/Explicit, every simulation problem is solved as a wave propagation between the neighbouring elements. A stable time increment is a minimum time for the wave to travel across any element in the model. The stable time increment defined as 'Δt' can be expressed as [4.14]:

$$\Delta t = \frac{L_{min}}{c_d} \tag{4.10}$$

Where, 'L_{min}' refers to the characteristic length in the mesh and 'c_d' is the dilatational wave speed. In order to decrease the stable time increment, 'L_{min}' can be decreased by decreasing the element dimensions or 'c_d' can be increased by increasing the material stiffness and decreasing the material's compressibility or density.

There are two types of time incrementation in Abaqus/Explicit [4.14]:

1. Fixed time incrementation.
2. Automatic time incrementation

In the fixed time incrementation, a constant time increment is used for the entire analysis. However, in the automatic time incrementation, there are further two types [4.14]:

1. Element by element time increment estimator
2. Global time increment estimator

In the first type, the dilatational wave speed is used to estimate the smallest time increment based on the coupled thermal-mechanical solution responses independently in each element of the FSW model. In the global time increment estimator, the analysis starts with the help of element by element estimation method and is, later on, switched to the global time increment estimator once the algorithm finds the accuracy of the global estimation method in an acceptable range. Since all elements of the workpiece have been kept as same, global time increment estimator has been used for all models to keep a moderate stable time for all increments.

4.1.8.3. Hourglass control

In the element type window, Abaqus offers an option of hourglass control for the particular elements. Due to the usage of reduced integration in both the Eulerian workpiece and Lagrangian tool, as discussed in section 4.1.6.2, the elements EC3D8RT and C3D8RT have only one integration point. The use of reduced integration saves a lot of computational time but on the other side, provides an occurrence of zero energy modes known as hourglass modes. These modes have no stiffness, and their deformations are called hourglass deformations. The use of one integration point allows the elements to distort so that the strains calculated at the integration point are all zero. The hourglass modes often lead to an uncontrolled mesh distortion in the analysis due to no stresses resisting these deformations.

The hourglass control is applied on the model so that the distortion can be avoided without any additional constraint on the element's physical response. This is typically achieved by adding stiffness to the hourglassing element, which resists the element's distortion and suppresses the velocity of the hourglass mode. In Abaqus/Explicit, there are three approaches available to damp the hourglass mode [4.15]:

1. Integral viscoelastic approach
2. Kelvin visco elastic approach
3. Enhanced hourglass control approach

As the sudden dynamic loading is more probable in the initial stage of the analysis step, an additional resistance is applied to hourglass forces in the integral viscoelastic approach. It is a very intensive hourglass control method. However, it is not supported for the Eulerian element EC3D8RT used in the current analysis, therefore, this approach cannot be used in the current models.

In the Kelvin visco elastic approach, a force 'Q' is used to conjugate the hourglass mode magnitude 'q'. The 'Q' can be defined as [4.15]:

$$Q = s[(1-\alpha)Kq + \alpha C\frac{dq}{dt}] \tag{4.11}$$

Where s is a scaling factor, K is the linear stiffness and C is the linear damping. 'α' corresponds to the blending weight factor to scale the stiffness and viscous parameters. The value of α can be set between zero and one. If it is zero, the hourglass control approach becomes a pure stiffness form, which is normally recommended for both transient dynamic and quasi-static analyses [4.15]. When it equals one, the same approach is reduced to the pure viscous form only, which is the default form for Eulerian EC3D8RT elements with reduced integration [4.15]. A combination of both stiffness and viscous contributions can be attained by specifying the blending weight factor between 0.0 and 1.0.

The enhanced hourglass control approach refines the pure stiffness method where the value of 'α' is zero. The stiffness coefficients are calculated by an enhanced assumed strain method, which provides an increased hourglass resistance for nonlinear materials. However, although normally beneficial, this approach often provides a high stiffness response for the model including plastic yielding materials under bending.

In all hourglass control approaches, the pure viscous form ($\alpha = 1$) of the Kelvin visco elastic approach is generally classified as the most computationally efficient and is very effective for high-speed dynamic analyses. Therefore, the pure viscous form was chosen and used for all FSW models in the current study.

4.1.8.4. CEL options

In the CEL approach, the preferred Lagrangian and Eulerian parts are coupled through a volume fraction tool. The volume fraction tool helps in creating a discrete field, which accounts for overlapping between two part instances (Eulerian part and the reference Lagrangian part). The discrete field can be used to assign initial material properties to each Eulerian element overlaying the reference part elements.

As illustrated in Figure 4.1, two geometries were created, and the smaller one was placed into the larger one. The larger geometry is referred as the Eulerian part, whereas the inner one is characterised as the Lagrangian reference part. The initial material is kept in the reference part. Hence, the workpiece is initially regarded as the 'Full Eulerian Material workpiece body', and any deformation can be visualised as long as it is inside the 'Void Eulerian material body' region. Only Eulerian part instance is meshed, and the reference part can later be suppressed in the assembly module.

In the step section, a predefined field ‘Material assignment’ was created to assign the above discrete volume fraction to the specific region (workpiece in the current case). A ‘medium accuracy’ was maintained by the software between the Eulerian and Lagrangian reference part interface.

4.1.8.5. Parallelisation method

For analyses with a large number of increments, the computational time of the simulation is a major concern. Therefore, parallel execution assists in reducing the run time of the analysis and producing such results that do not depend on the number of computer processors used for the analysis.

For Abaqus/Explicit, there are two types of parallelisation methods available [4.16]:

1. Domain level decomposition
2. Loop level decomposition

In the domain level decomposition method, the software automatically discretises the model into a given number of topological domains (based on the number of processors). Domains are then assigned to the available processors. Due to the analysis being carried out independently in each domain, the information is passed between the domains in each increment where the domains share common boundaries. This method is generally recommended for very large analyses. Figure 4.8 demonstrates an example of the domain level decomposition method using the FSW model simulated in the current research.

In the loop level decomposition method, low-level loops are parallelised to increase the computational efficiency of the analysis. All processors repeatedly calculate each increment for a single domain. Simulation operations involving elements, nodes and contact pairs account for the majority of the low-level routines. A comparison was made between the run times of a simpler model using both parallelisation methods individually. It was observed that the domain level decomposition method was proved computationally efficient than the other one for the current model. Therefore, 60 domains were created on the High Performance Computing (HPC) facility by Archie-WeSt hosted by the University of Strathclyde. Five nodes were used to solve each simulation where each node included 12 x Dual Intel Xeon X5650 2.66 GHz processors.

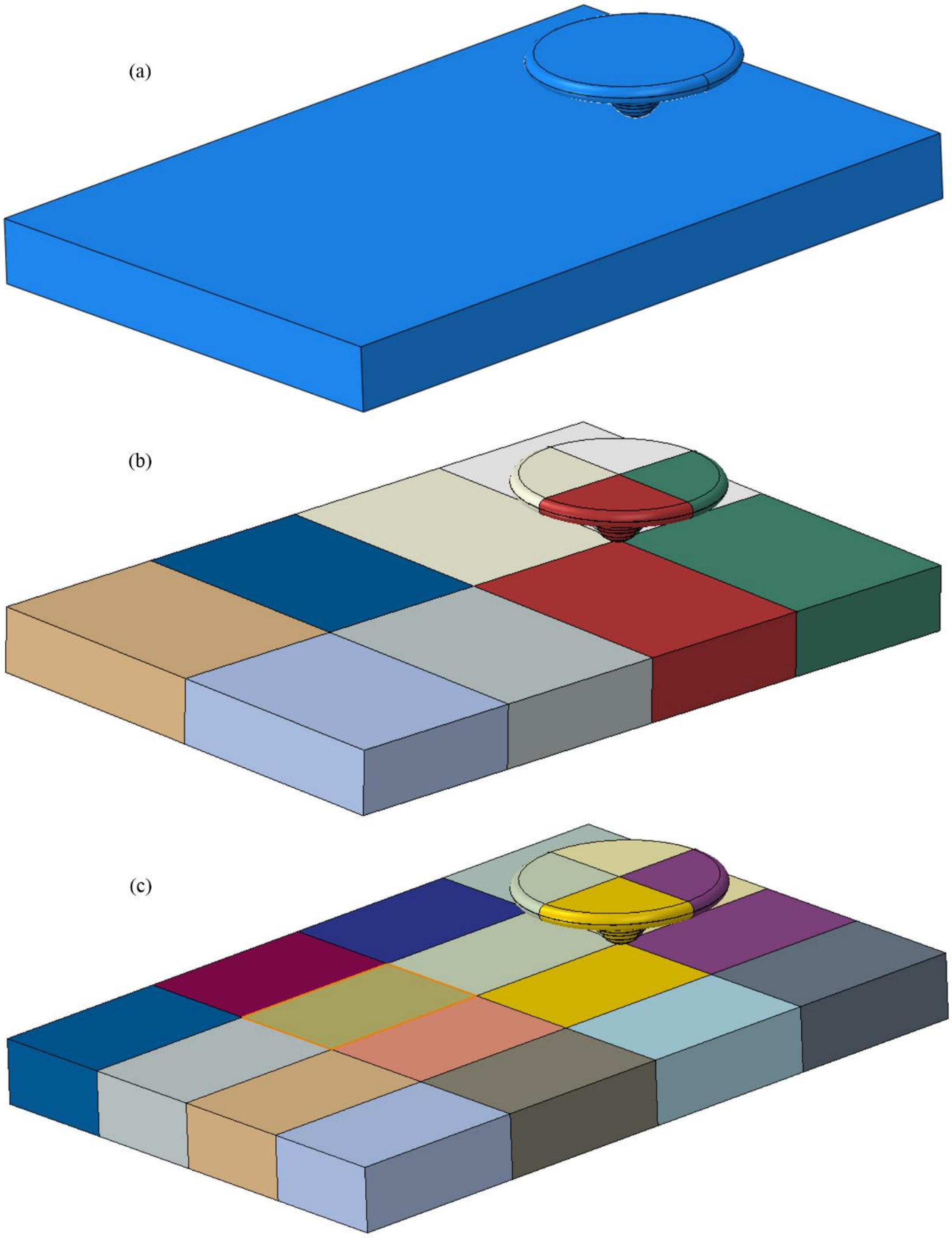

Figure 4.8: Domain level decomposition with (a) Single domain (b) Eight domains (c) Sixteen domains.

4.1.8.6. Precision Level

In Abaqus/Explicit, there are two types of mathematical executions: single and double. The single precision mathematics solves less significant digits and generally saves computational memory and time, whereas the double precision mathematics provides more accurate results as it solves more significant digits and is therefore less prone to round off errors. Since the current FSW models contain more than 30,000 elements, the double precision execution has been applied to all models to reduce errors.

4.1.8.7. Computational efficiency

There are two primary techniques for artificially reducing the computational time for simulations in Abaqus:

1. Mass scaling
2. Time scaling

Mass scaling is an approach for speeding up the analysis by increasing the stable time increment size in each step. The density of the material is artificially increased to a factor of 'f^2', which increases the stable time increment by a factor of 'f'. In an Eulerian domain, the material flows through the mesh instead of moving with the specified set of nodes. So, the mass scaling technique cannot be used in the current model, as changing the mass of the Eulerian elements will keep on adding and subtracting the material from the model that is not viable. In addition, the thermal solution response in a fully coupled thermal stress analysis is not affected by the mass scaling as per Abaqus documentation [4.17].

In the time scaling technique, load rates in the analysis are artificially raised to speed up the process. All process parameters, i.e. tool plunge and traverse speed along with the rotation are increased to a constant factor whereas the time-period of each step is reduced with the same factor. However, due to the material's temperature rate dependent properties, it was observed that accurate thermal results were not obtained. Therefore, adequate changes were made by artificially increasing the thermal conductivity of the material and convective coefficients for a reasonable heat transfer process. Li [4.18] simulated an FSW thermomechanical model for aluminium AA2024-T3. It was reported that reasonable results were obtained with 100 times increased rotational and translational speeds when the thermal conductivity, top convective coefficient and bottom convective coefficient of the workpiece were increased up to 200, 100 and 20 times, respectively [4.18]. Therefore, similar ratios were applied to all models except the bottom convective coefficient of the workpiece being scaled to 10 times the original value due to the steel workpiece. This configuration of time scaling was only applied to run the model in a computer with 16.0 GB ram and 8-cores processor computer of 3.6 GHz each to look up for any error possibilities without spending additional time. Once the model presented results with increased process parameters, necessary changes (normal process parameters and material properties) were made for the realistic results and the model was then run on the HPC as discussed previously.

4.2. Results and discussion

Although a wide variety of models has been assessed as part of this research, two characteristic models are discussed in this chapter (as classified in Table 4.5). To compare the results, the remaining features such as tool and workpiece materials and geometries, frictional contact, heat transfer coefficient, etc. are kept identical for both models. Temperature distribution, plastic strain, flash generation and potential flaws have been computed for the workpiece.

4.2.1. Plunge stage

Figure 4.9 displays the temperature contours in the plan and cross-sectional views of the slow and fast weld models for the plunge stage. Since the feed rate in the downward direction has been set as constant (100 mm/min) for both models, the comparison of results in the plunge stage is solely based on the rotational speed of the tool. The temperature in the plunge stage for the fast weld model is slightly higher than that of the slow weld one due to the high rotational speed in the former model. The thermomechanically affected zone (TMAZ) was identified as the region with maximum equivalent plastic strain (mainly near the tool and workpiece interface shown in Figure 4.10), as illustrated in a previous research [4.2]. For the slow weld model, the thermomechanically affected zone (TMAZ) lies above 770°C and the heat affected zone (HAZ) is in the temperature range of 370°C to 750°C, whereas, for the fast weld model, the maximum temperature in the TMAZ is 889°C and the HAZ is between 330°C to 889°C. Note that the cross-sectional views in Figure. 4.9 to 4.17, i.e. those that present numerical and/or experimental results, have been set on the same scale whilst the top views have been truncated to assist with the interpretation.

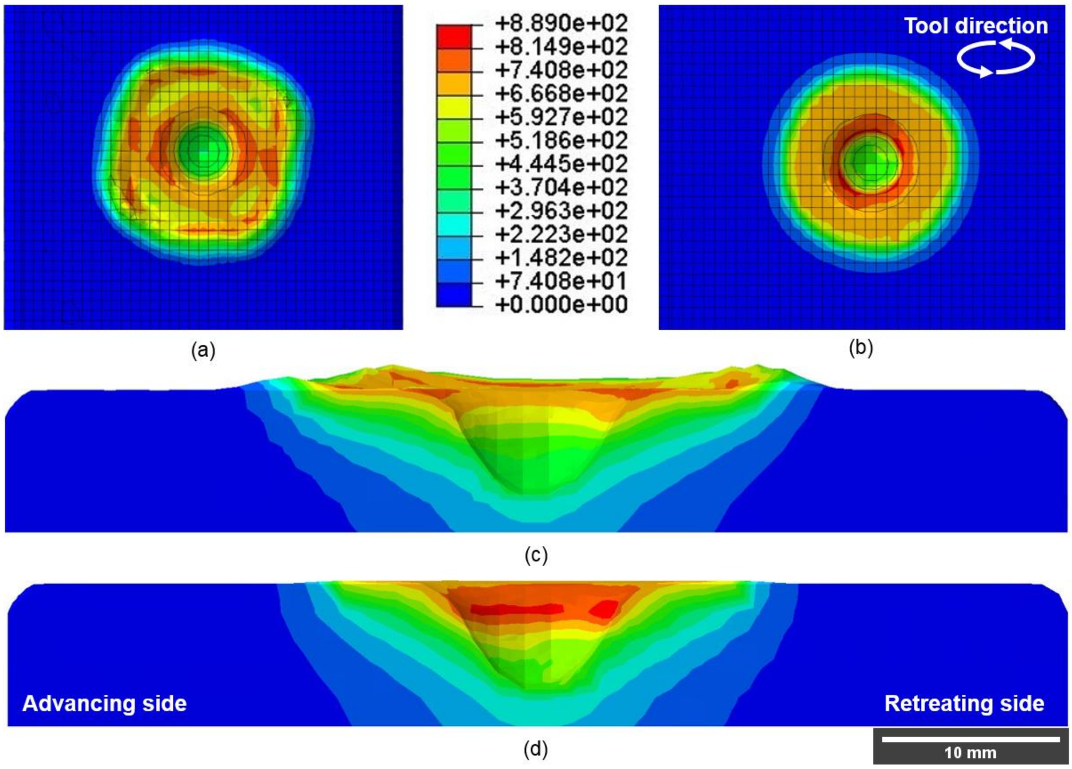

Figure 4.9: Temperature distribution in °C at the end of the plunge stage; (a) Top view of the slow weld model, (b) Top view of the fast weld model, (c) Cross sectional view of the slow weld model and (d) Cross sectional view of the fast weld model.

As FSW results in a very high plastic deformation, the elastic strain can be considered as negligible relative to the plastic strain [4.2]. The plastic strain profile has been discussed in this section to understand the deformation during all FSW stages by visualising top and cross sectional views of the weld. Figure 4.10 exhibits the equivalent plastic strain distribution in the top and cross sectional view of the slow and fast weld models for the plunge stage. The maximum plastic strain has been recorded in the slow weld model (Figure 4.10a&c). In the fast weld model (Figure 4.10b&d), the increased rotational speed gave rise to the heat generation that promoted less friction between the tool and the workpiece due to the slip effect between them. The same phenomenon has also been reported by Dubourg et al. [4.19]. Consequently, reduced plastic strain was observed in the fast weld model as compared to the slow weld model. Thus, the slow weld model exhibits a larger plastic strain area than the fast weld model as seen in both top and cross sectional views (Figure 4.10).

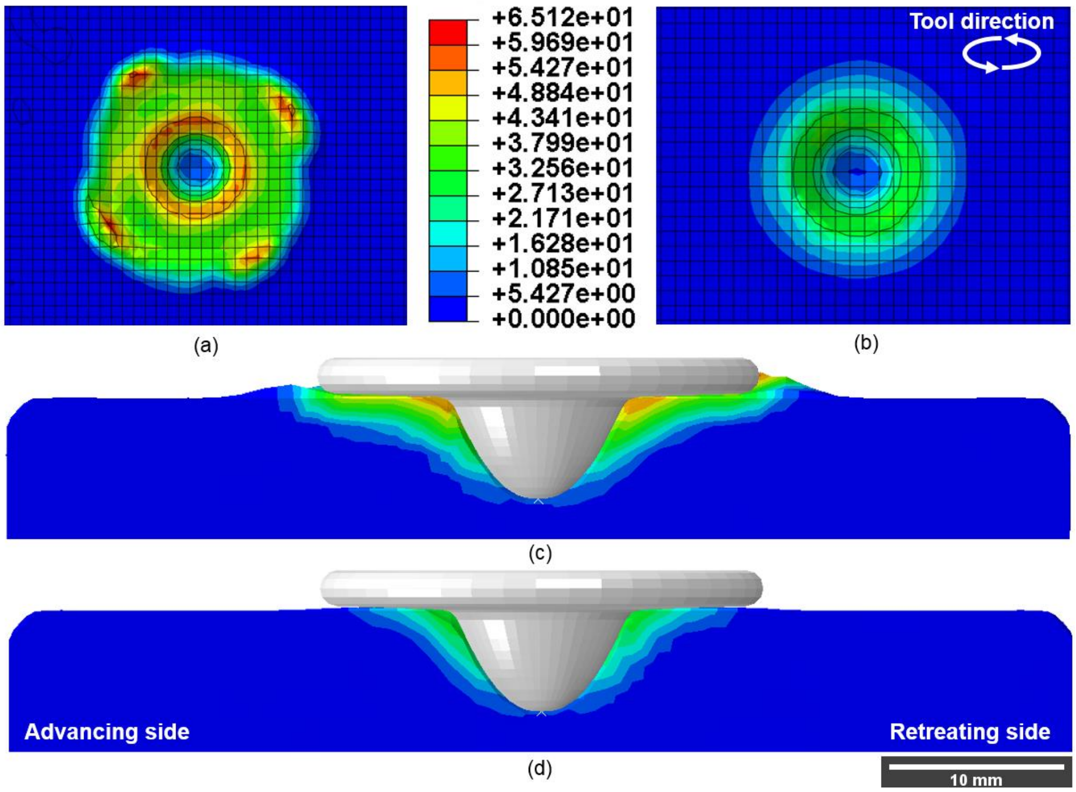

Figure 4.10: Equivalent plastic strain distribution at the end of the plunge stage; (a) Top view of the slow weld model, (b) Top view of the fast weld model, (c) Cross sectional view of the slow weld model and (d) Cross sectional view of the fast weld model.

4.2.2. Dwell stage

In the dwell stage, the temperature distribution in the slow weld model (Figure 4.11a&c) covers a larger area than the fast one (Figure 4.11b&d). As seen in Table 4.2, the thermal conductivity of the material decreases with increasing temperature. This results in a reduction of the heat transfer in the workpiece. In contrast, temperature values are higher in the fast weld model with a difference of 91°C. The maximum temperature in the slow weld model reached 993.7°C on the shoulder-workpiece interface, and in the fast weld model at 1084°C in the same region. The high heat generation rate and the temperature values in the fast weld model are due to the increased rotational speed that increases the relative velocity between the tool and the workpiece, as discussed by Nandan et al. [4.7] and Colegrove et al. [4.20]. The temperature profile tended to spread towards the sides and bottom of the workpiece. This demonstrates that the dwell time for the fast weld model can be reduced since it has more tendency to heat the surrounding material in less time.

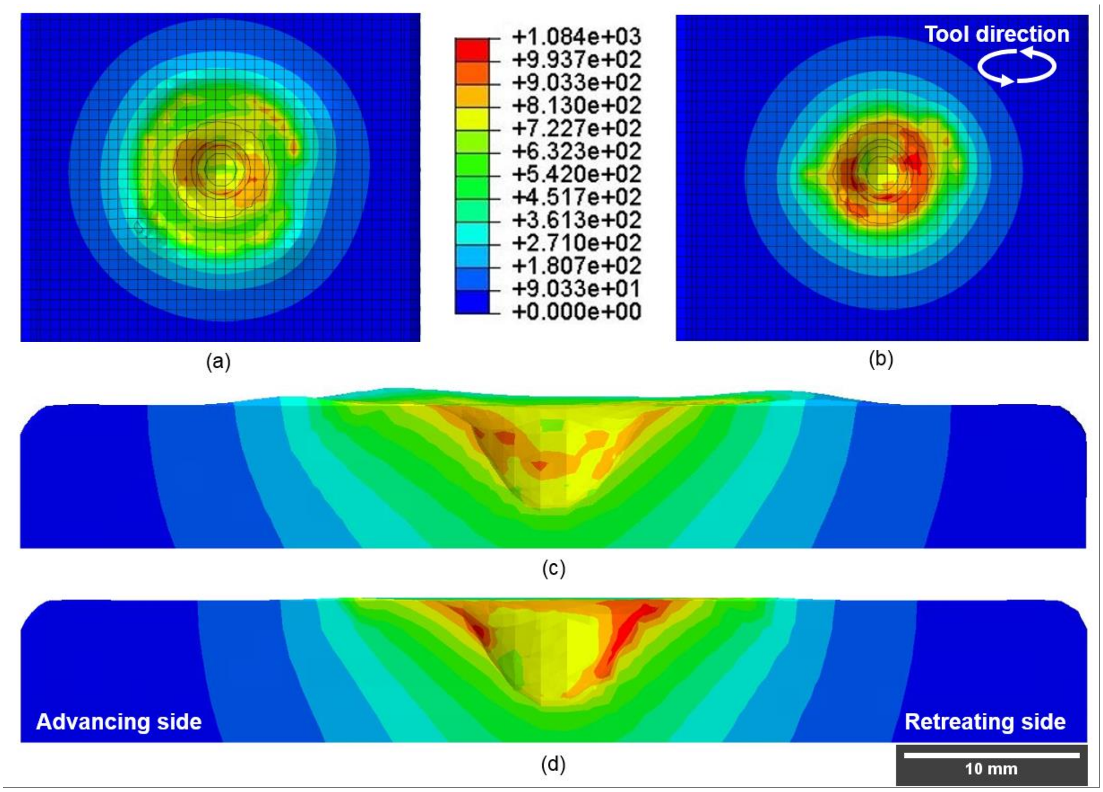

Figure 4.11: Temperature distribution in °C at the end of the dwell stage; (a) Isometric view of the slow weld model, (b) isometric view of the fast weld model, (c) cross sectional view of the slow weld model and (d) cross sectional view of the fast weld model.

As in the plunge stage, the plastic strain in the dwell stage is greater in the slow weld model (Figure 4.12a&c) compared to the fast weld (Figure 4.12b&d). A maximum strain of 64.22 is achieved on the surface of the slow weld model (Figure 4.12a) due to the excessive flash generation. Both models tend to present symmetrical plastic strain distribution across the vertical axis of the tool. Reduced plastic strain is observed in the bottom tip of the tool probe in both models, which could result in potential defects due to incomplete stirring before the tool traverses.

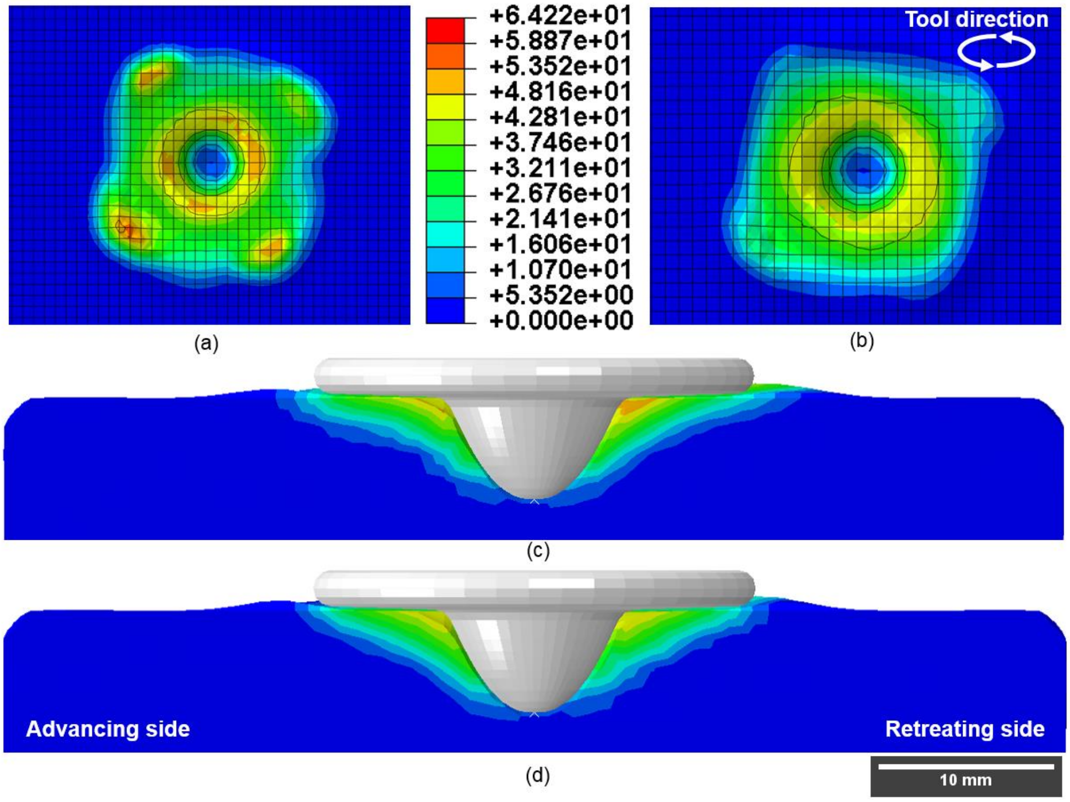

Figure 4.12: Equivalent plastic strain distribution at the end of the dwell stage; (a) Top view of the slow weld model, (b) Top view of the fast weld model, (c) Cross sectional view of the slow weld model and (d) Cross sectional view of the fast weld model.

4.2.3. Traverse stage

The numerical results produced for both models have been compared with the experimental work of a prior publication [4.1] as shown in Figure 4.13. The HAZ in the slow weld is larger as compared to the corresponding region in the fast weld since more heat per unit length was transferred to the workpiece by the slower movement of the tool. The maximum temperature reached in the slow weld model is 964°C and in the fast weld model is 1157°C. The maximum temperature values were located just next to the shoulder interface for both models, also mentioned by Selvamani et al. [4.21] as well. The HAZ is in the range of 578°C to 771°C for the slow weld model and 674°C to 867°C for the fast weld model. Temperature values were higher in the advancing side than the retreating side for both models, which is in accordance with the findings of Jweeg et al. [4.22]. However, the heat per unit length was larger in the slow weld model than the fast weld model. The decreased traverse speed in the slow weld model resulted in an overall temperature rise during the welding. Similar results have been reported by several other researchers [4.23-4.25]. The temperature profile on the workpiece's surface in the fast weld model is much narrower than the one in the slow weld model. The decreased traversing speed of the tool resulted in expanding the heat dissipation across the workpiece, whereas the fast traversing speed restricted the heat in the TMAZ, along with a narrow HAZ. The fast weld model is creating the same asymmetry between advancing and retreating side as in the actual welding. This was reported by Micallef et al. [4.4] as well for the case of high speed welds. The fast weld parameters are potentially desirable with regard to increased productivity with acceptable quality welds on an industrial scale, while the slow weld parameters can be beneficial for producing excellent quality and symmetrical welds. Similar results have been discussed by Toumpis et al. [4.1] as well.

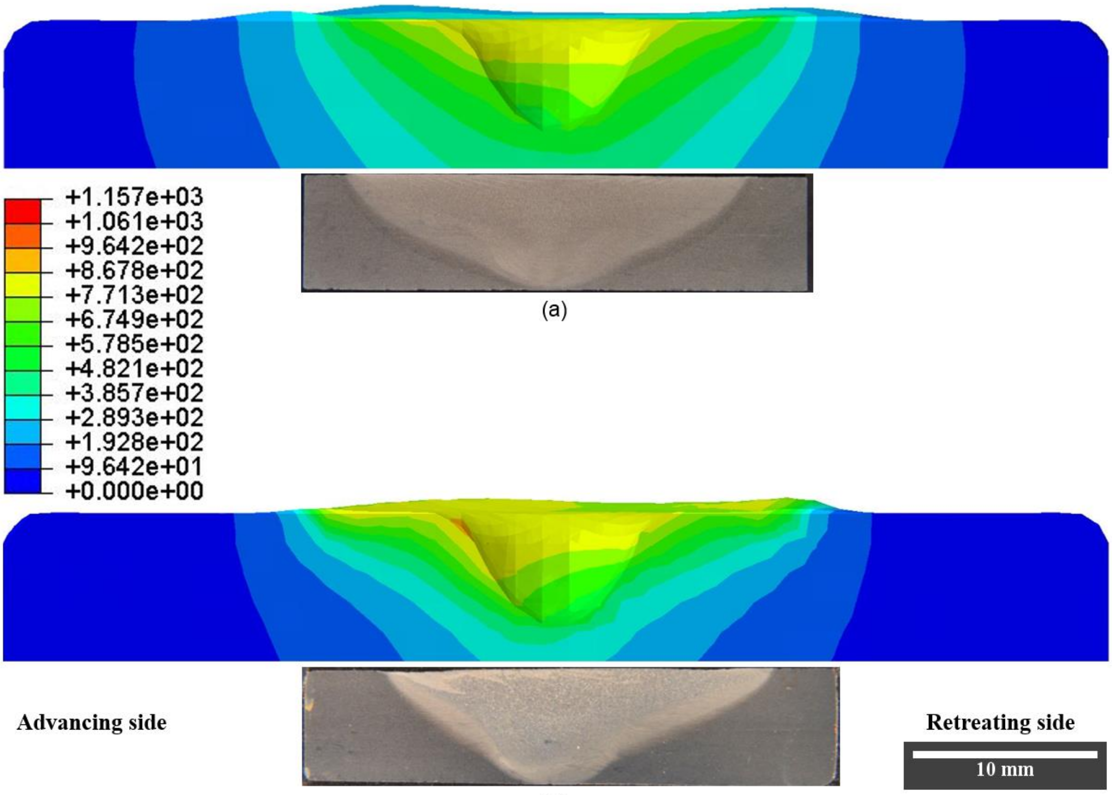

(a)

(b)

Figure 4.13: Qualitative analysis at the traverse stage; Numerical and experimental cross sectional views of the (a) Slow weld model (b) Fast weld model. Temperature distribution in ^{o}C in the numerical results. Macrographs from [4.1].

To observe the thermal cycles during the FSW process, the temperature change over time has been recorded for six nodal points in the workpiece. Three of them are located on the retreating side, and the rest are on the advancing side as shown in Figure 4.14. The points recording the temperature values are on a cross-sectional area at the distance of 13.5 mm from the tool's initial plunge position.

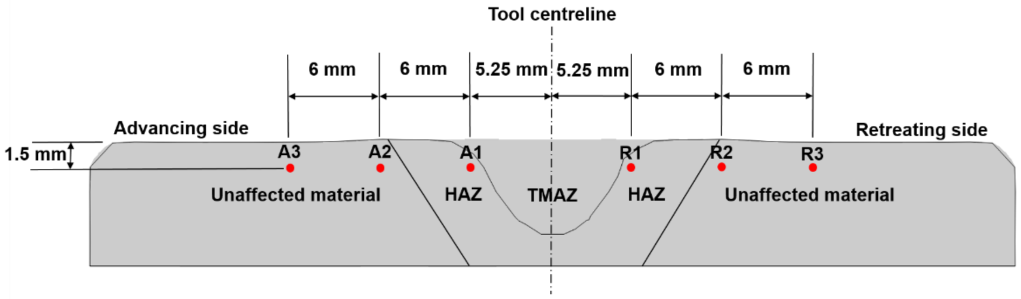

Figure 4.14: Location of nodal points on the workpiece for monitoring temperature changes with respect to time.

The thermal cycles for the slow and fast weld models at specified nodal points are shown in Figure 4.15 and 4.16, respectively. The nodal points A1 and R1 lie in the HAZ whereas A2, A3, R2 and R3 lie in the unaffected parent material. The plunge, dwell and traverse stages start from 0, 3.56 and 7.56 seconds, respectively. It is observed that the temperature profiles over time of the nodes in the advancing side are higher than the respective nodes in the retreating side. In addition, an abrupt decrease in the heating and cooling rates can be visualised from the nodes closer to the tool centreline than the ones far from it. A similar pattern of results has been reported by Nandan et al. [4.7].

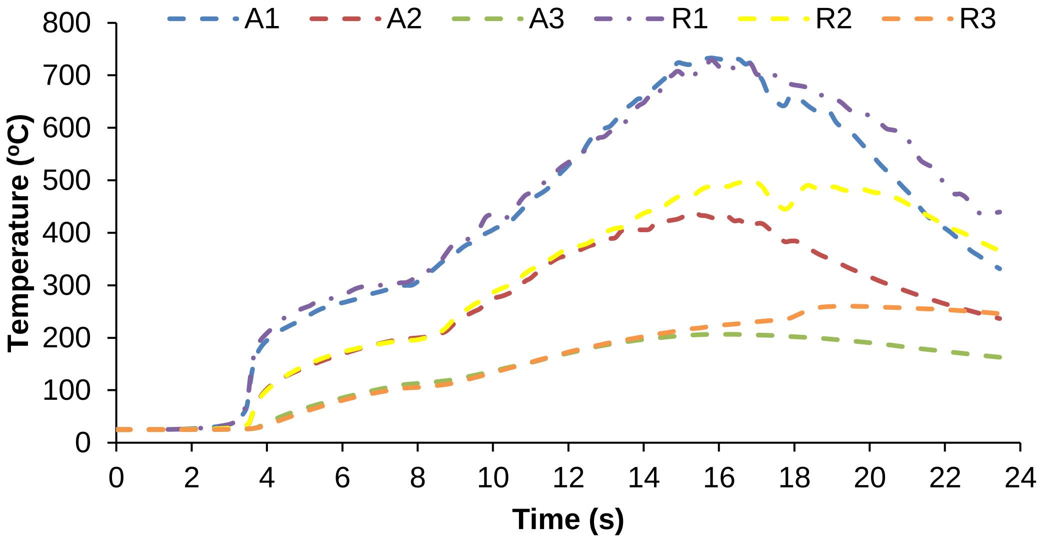

Figure 4.15: Thermal cycle for the slow weld model.

In the slow weld model, the temperature profile for all respective nodes in the advancing and the retreating sides appears to follow the same slopes during heating. During the cooling phase, the nodes on the retreating side tend to have a slower rate than the ones on the advancing side. In the CEL approach, the material moves independently to the mesh in the Eulerian region, and the temperature profile is recorded for the given nodal point irrespective of the material movement as shown in Figure 4.14. Therefore, the irregular temperature profiles can be related to the independent movement of flash material above the nodal points A1, A2, R1 and R2. Unlike the slow weld model, the temperature values are smooth in the fast weld model (Figure 4.16). The respective nodes on the advancing and retreating sides follow the similar trend during both heating and cooling phases. However, the nodes far from the tool centreline (A3 and R3) keep on heating even after the tool has traversed while a cooling effect can be seen in other nodes.

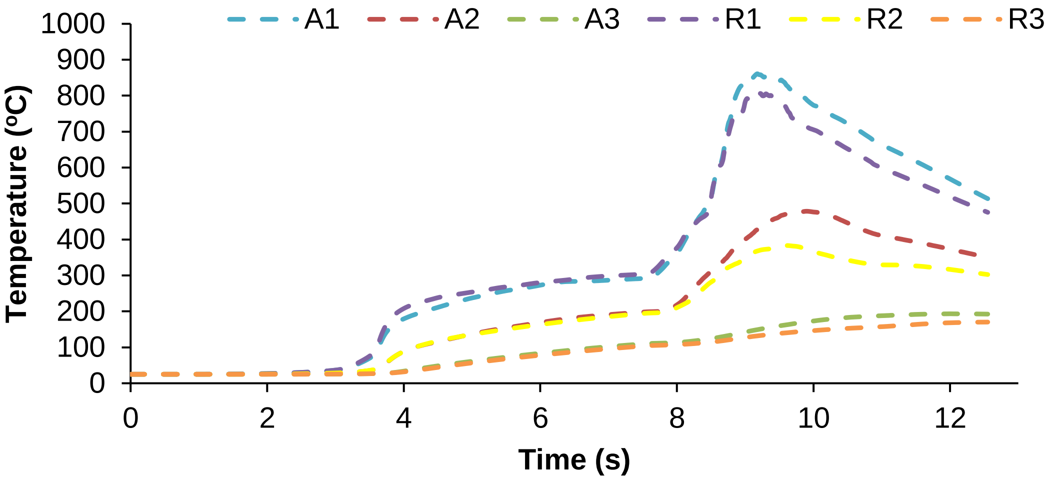

Figure 4.16: Thermal cycle for the fast weld model.

It is shown in Figure 4.17 that the plastic strain distribution is not symmetrical across the vertical axis for both models. The advancing side in Figure 4.17c&d has a higher average plastic strain than the retreating side of each weld. The plastic strain region is extensive near the tool probe and shoulder interface. In comparison to the surface near to the shoulder, the area towards the tool probe experienced reduced plastic strain. Moreover, the plastic strain in the slow weld model is higher than the fast weld strain. The demonstrates that the plastic strain in the TMAZ is inversely related to the traverse speed, also reported by Reynolds et al. [4.26].

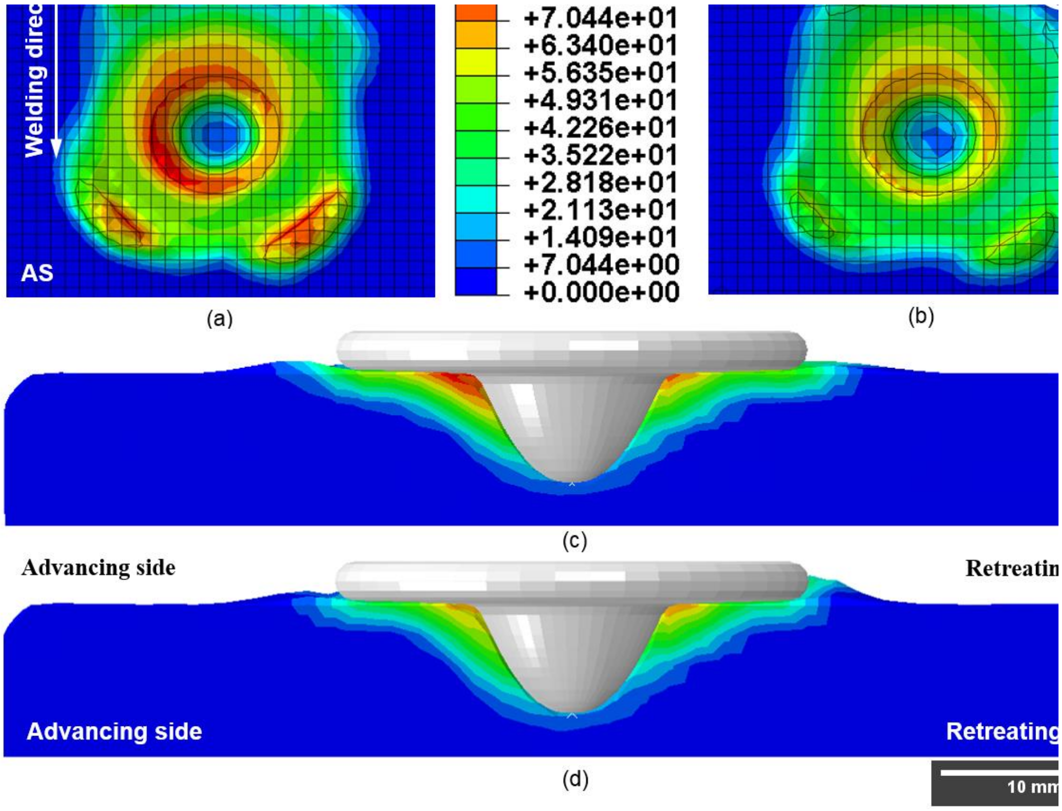

Figure 4.17: Equivalent plastic strain distribution at the Traverse stage; (a) Top view of the slow weld model, (b) Top view of the fast weld model, (c) Cross sectional view of the slow weld model and (d) Cross sectional view of the fast weld model.

4.2.4. Tool reaction forces

A significant purpose of numerical modelling of FSW is to predict the reaction forces on the tool so that the tool life may be extended. The short life of the tool for steel FSW is mainly due to high temperatures and maximum stresses [4.27-4.29]. Several studies have shown that the maximum stresses are experienced by the tool probe during the FSW process [4.1,4.27,4.29]. Therefore, the reaction forces have been compared on the tip of the tool probe for both models as shown in Figure 4.18. The total time for the FSW process including plunge, dwell and traverse stage is 23.4 seconds for the slow weld model and 12.8 seconds for the fast weld model. This is due to the modelling of an identical 100 mm long workpiece for different traverse speeds in slow and fast weld models.

The reaction force on the tool probe tip was gradually increased at the start of the FSW process due to the downward movement in the plunge stage. The first linear increment between 0 and 3 seconds is due to the gradual plunge of the probe area into the workpiece. The reaction force on the tool probe tip drastically increased with a steeper slope after the tool was fully penetrated in the workpiece. A high peak of ~110 kN and 120 kN can be observed for the fast and slow weld model, respectively, when the shoulder is in complete contact with the workpiece. Increasing the tool's rotational speed decreases the magnitude of the reaction force on the tool probe [4.25,4.30], which can also be seen during the plunge and the dwell stage in Figure 4.18. However, as the traverse speed has a direct relation with the reaction force [4.25,4.30], the fast weld model has relatively high reaction forces on the tool probe tip than the slow weld model.

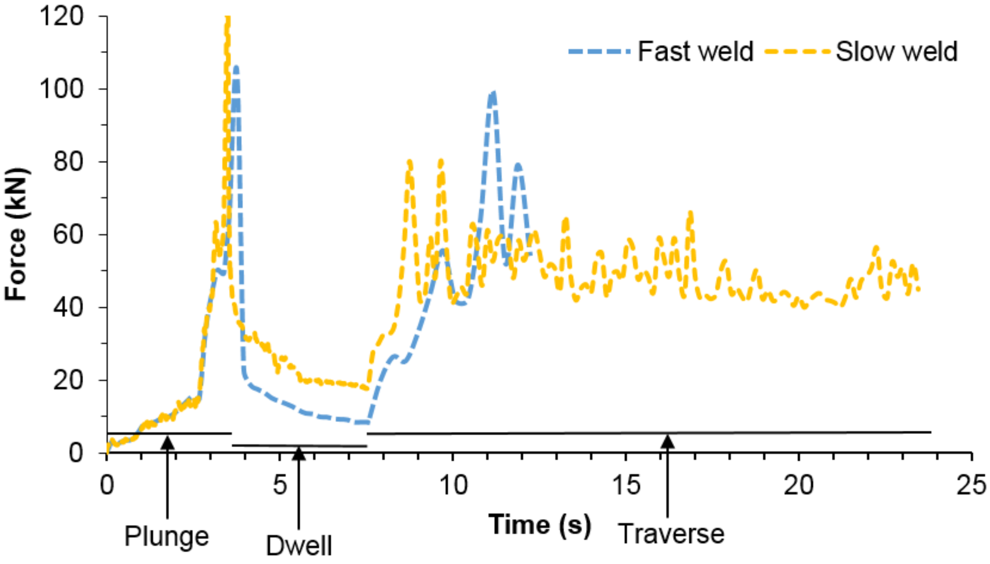

Figure 4.18: Resultant reaction force comparison on the tool tip in both models.

Since there was no translational movement of the tool during the dwell stage, the reaction forces abruptly dropped in both slow and fast weld models. As discussed in section 4.2.2, the temperature profile in the fast weld model was relatively higher than the slow weld model during the dwell stage. This temperature rise resulted in reducing the tool reaction forces in the fast weld model, falling steadily to 10 kN. On the other hand, an average value of 20 kN was achieved during the dwell stage in the slow weld model.

The tool reaction forces during the traverse stage were mainly due to the translational velocity of the tool in the X-axis and the rotational velocity along the Y-axis. At the start of the traverse stage, the reaction forces linearly increased for both models (time = 7.5 – 9.8 seconds in Figure 4.18). This is due to the preheated surface around the tool during the dwell stage. When the tool reached the edge of the dwell's preheated zone, the reaction forces for both the fast and slow welds started stabilising with the mean values of 65 kN and 45 kN each. The unsteady values of reaction forces may be contributed to the smaller dimensions of the workpiece model as compared to the original values as the length and width ratios of the original workpiece to the model are 20:1 and 6.66:1, respectively. The tool dimensions have been set as original values. In addition, since there was no movement allowed to the bottom surface of the workpiece, the tool may have experienced more perturbation due to this surface constraint.

Figure 4.19 shows the resolved components of reaction forces in x, y and z-axis for the slow weld model. The axial reaction force in the vertically downward (Y) direction is shown by the yellow dotted line, while red and blue lines represent the transverse (Z) and the longitudinal (X) directions, respectively. It can be seen that the RF-Y is dominant throughout the whole process.

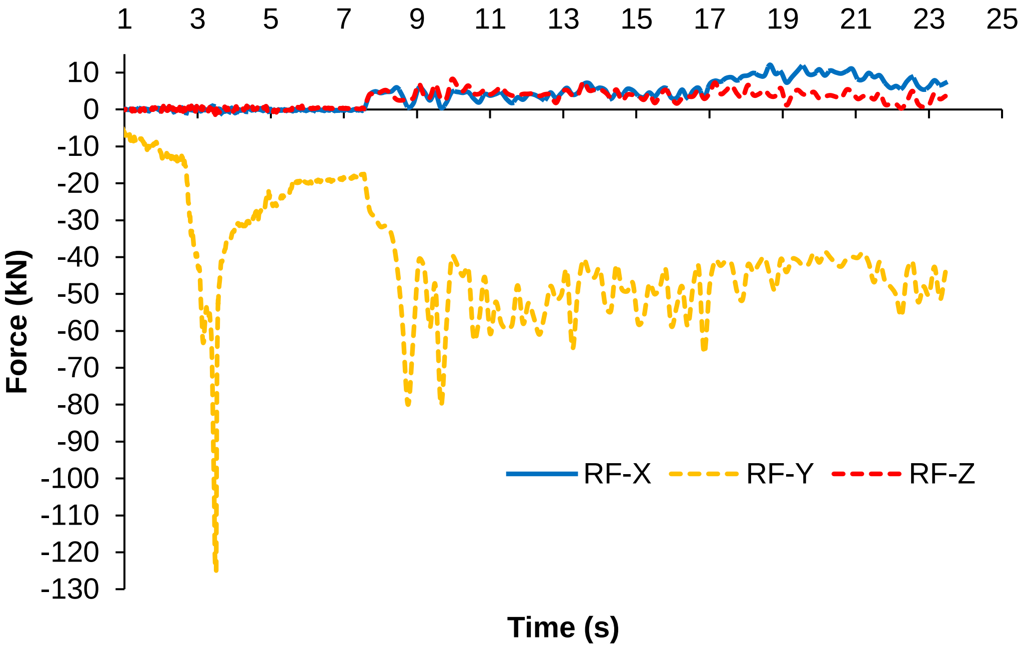

Figure 4.19: Reaction force components for the slow weld model.

Similarly, the reaction force components for the fast weld model are displayed in Figure 4.20. The reaction force distribution follows the same pattern as in Figure 4.19 with different values showing that the tool is prone to experience maximum reaction forces in the plunge stage, also derived from the previous experimental work [4.1]. It is observed that the tool reaction forces during the plunge and the dwell stage are comparatively lower in the fast weld model than the slow weld model. This indicates that the tool damage may be prevented by preheating the workpiece prior to the tool plunge.

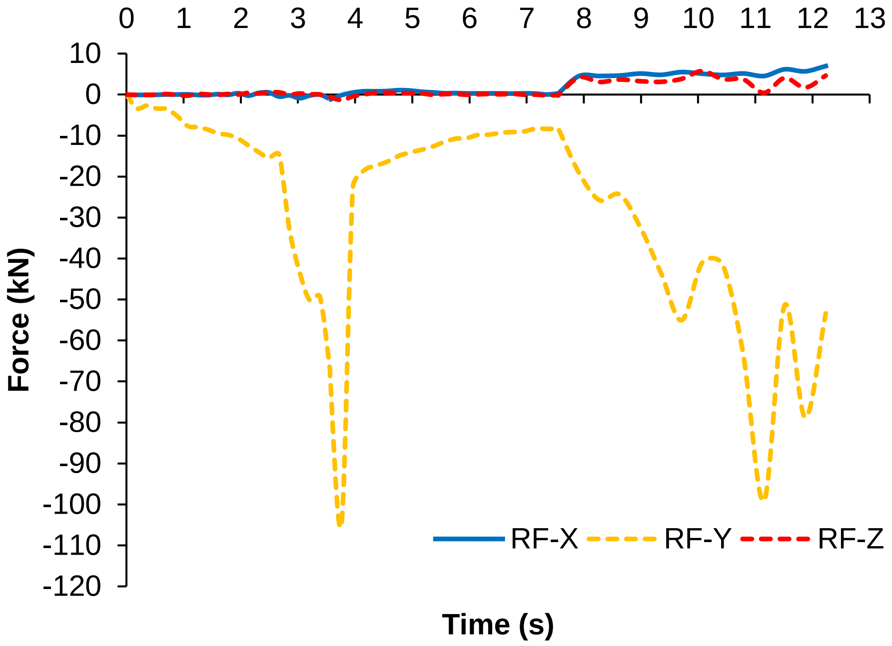

Figure 4.20: Reaction force model for the fast weld model.

4.2.5. Material movement

Material flow during the FSW is critical for obtaining defect free welds [4.31]. Visualising the material flow during the welding process is of great significance as it provides a better understanding of the material deformation inside the workpiece. This section discusses the material movement by visualising the tracer particles present in the workpiece, as discussed in section 4.1.7. The initial positions for all tracer sets have been shown previously in Figure 4.7.

The material flow in the FSW process is influenced by the plunge force, tool traverse and the rotational direction of the tool that stirs the material [4.32]. During the plunge stage, the rotating tool penetrates inside the workpiece material [4.33]. Figure 4.21 and 4.22 represent the top view of the material flow in the workpiece for both models during the plunge stage by the help of Tracer set – 1. The general direction of the material flow during the FSW process is similar to the tool's rotational direction [4.34].

As the temperature rises in the plunge region, the tracer particles exhibiting the material flow start swirling in the anticlockwise direction as seen in Figure 4.21 and 4.22. The lower rotational speed in the slow weld model has tended to establish a strong frictional contact on the tool-workpiece interface, hence enabling the material movement to flow more efficiently than the fast weld model. A streamline comparison for both models through a single tracer particle in the plunge stage has been shown in Figure 4.23.

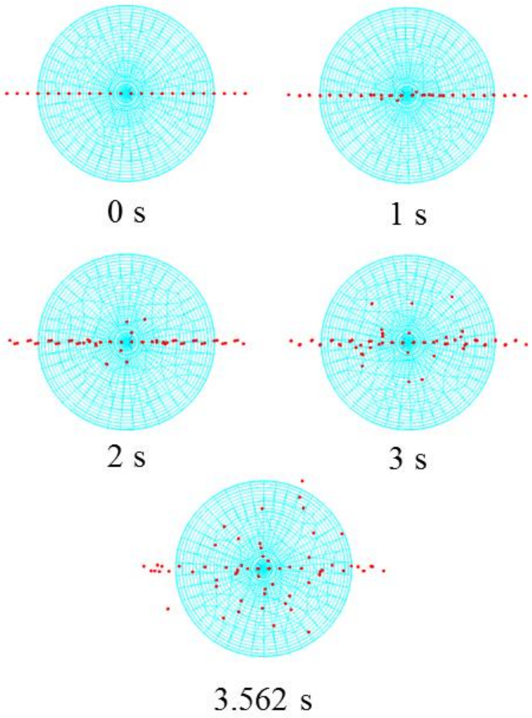

Figure 4.21: Material flow in the slow weld model during the plunge stage (Tool rotation: Anticlockwise direction).

Figure 4.24 and 4.25 represent the top view of the material flow in the workpiece for both models during the dwell stage by the help of Tracer set – 1. Since the heat in the dwell stage has softened the workpiece material around the tool surface, the tracer particles can be seen moving with lower resistance. This also explains the relation of the tool’s rotational speed and the temperature values with the material movement in the region.

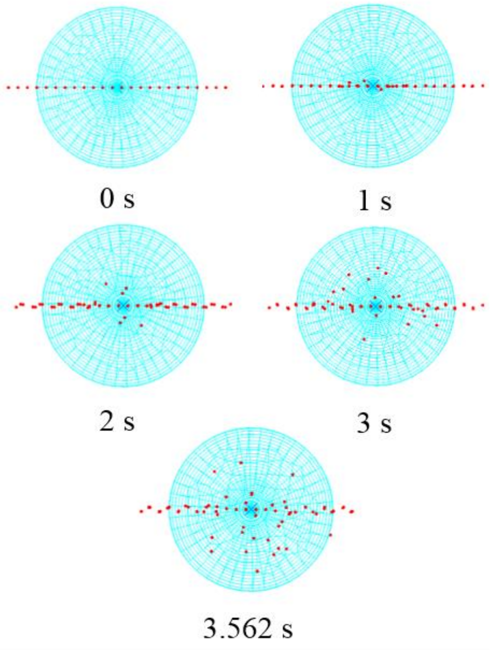

Figure 4.22: Material flow in the fast weld model during the plunge stage (Tool rotation: Anticlockwise direction).

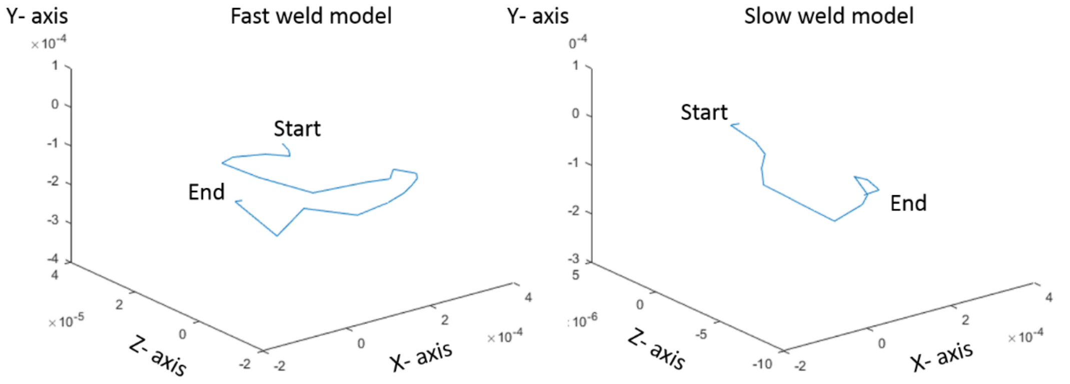

Figure 4.23: Tracer particle displacement (mm) at the end of the plunge stage for both models.

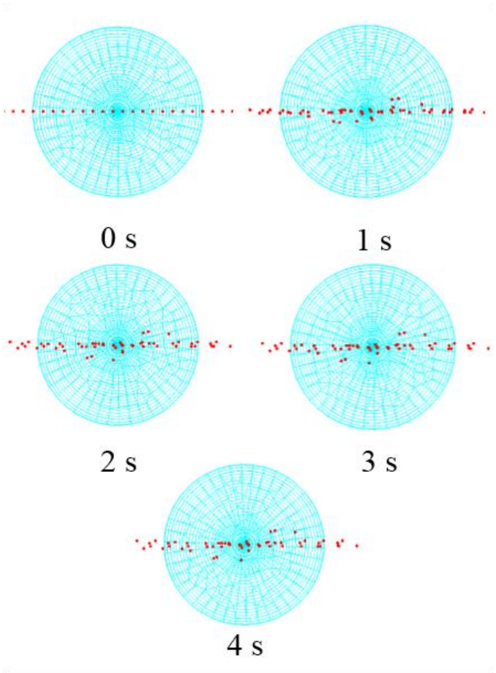

Figure 4.24: Material flow in the slow weld model during the dwell stage (Tool rotation: Anticlockwise direction).

Figure 4.26 and 4.27 represent the top view of the material flow in the workpiece for both models during the traverse stage with the help of Tracer sets – 2, 3 and 4. The tool is traversing in the upward direction in both Figure 4.26 and 4.27. When the tool traverses, the workpiece material located on the leading edge begins to follow the movement of the tool, swirling from the advancing side to the retreating side. The material then flows through the trailing edge, also reported by Kumar et al. [4.35] and Xu et al. [4.36]. Once the tool further traverses, some of the particles are mixed and left behind while some of them keep swirling around the moving tool (Figure 4.26 and 4.27). The material swirling around the tool influences the traverse force acting on the tool such that an increase in swirling will result in lowering the reaction forces on the tool to traverse through the workpiece [4.37]. Nandan et al. [4.38] reported that substantial material flow occurs closely to the FSW tool. Similar results can be observed in all FSW stages for both models.

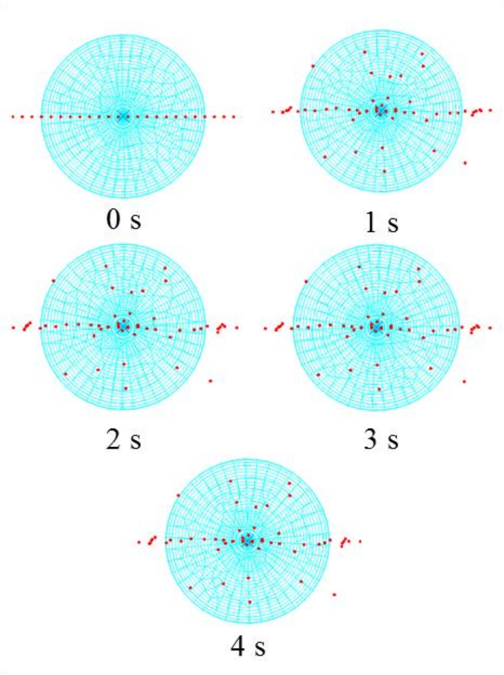

Figure 4.25: Material flow in the fast weld model during the dwell stage (Tool rotation: Anticlockwise direction).

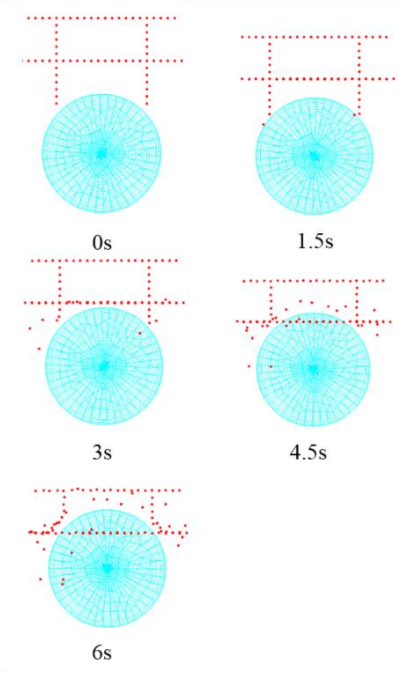

Figure 4.26: Material flow in the slow weld model during the traverse stage (Tool rotation: Anticlockwise direction).

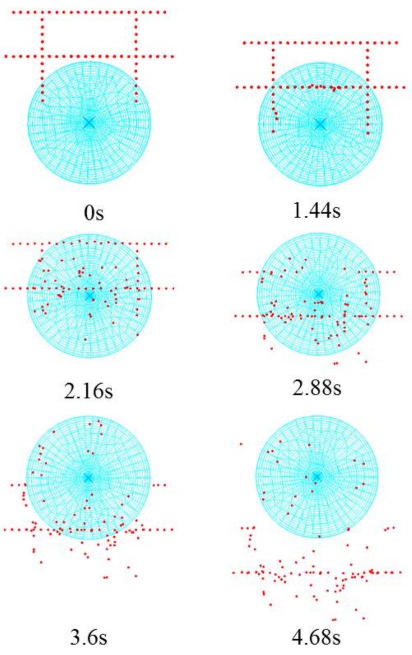

Figure 4.27: Material flow in the fast weld model during the traverse stage (Tool rotation: Anticlockwise direction).

The asymmetry of the temperature distribution during the FSW process influences the variation of the material flow in the workpiece [4.7]. Since the material flow during the FSW process is related to the tool probe's rotational and traverse speed [4.30], the material flow visualisation of both models depict that the increased rotational and traverse speed of the tool allows the material to move in the traverse stage more vigorously.

4.2.6. Flash and potential defect generation

Top surface and cross-sectional macrographs were produced for the actual friction stir welds and the numerical models. A maximum flash was observed on the workpiece's surface in the slow weld model (Figure 4.30a). This occurred since the slow traversing speed resulted in lower peak temperatures, hence causing the material on the upper surface of the workpiece to abrade away instead of thermomechanically stirring. In addition, an increased resistance for the material to flow to the trailing side resulted in the flash formation by making the material flow out of the workpiece surface, also reported by Kumar et al. [4.35].

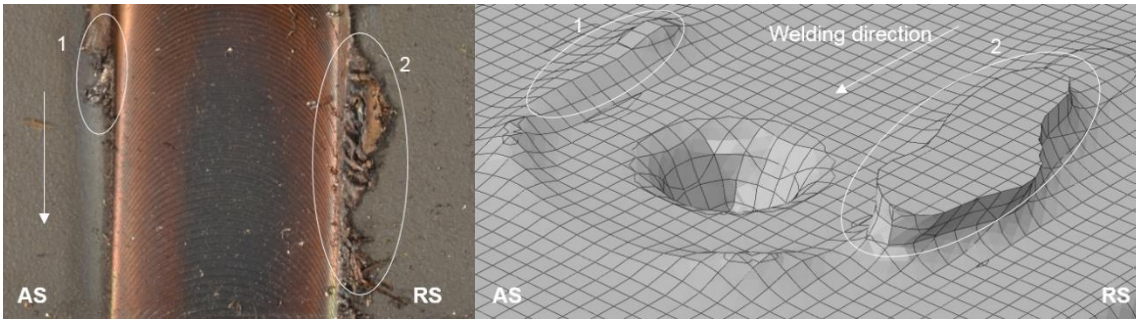

Figure 4.28: Visualisation of flash generated experimentally and numerically in the slow weld model.

In the fast weld model, the high rotation and translation of the tool led to maximum stirring in the TMAZ hence producing an insignificant flash. Similar results have also been seen in weld macrographs for both of these models as shown in Figure 4.28 and 4.29.

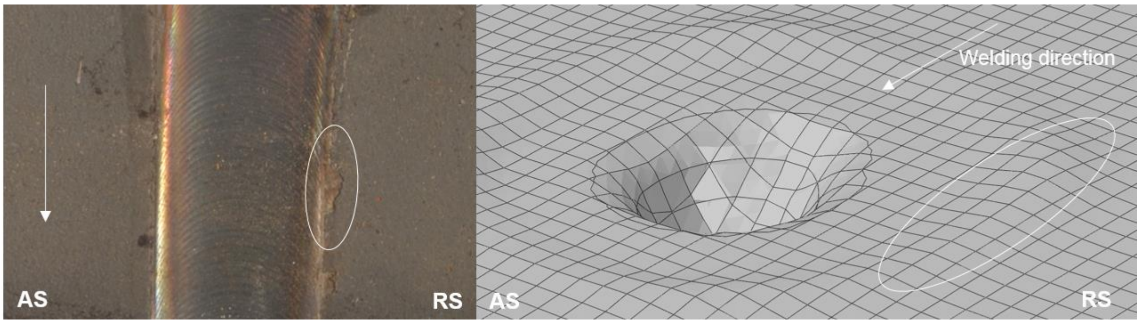

Figure 4.29: Visualization of flash generated experimentally and numerically in the fast weld model.

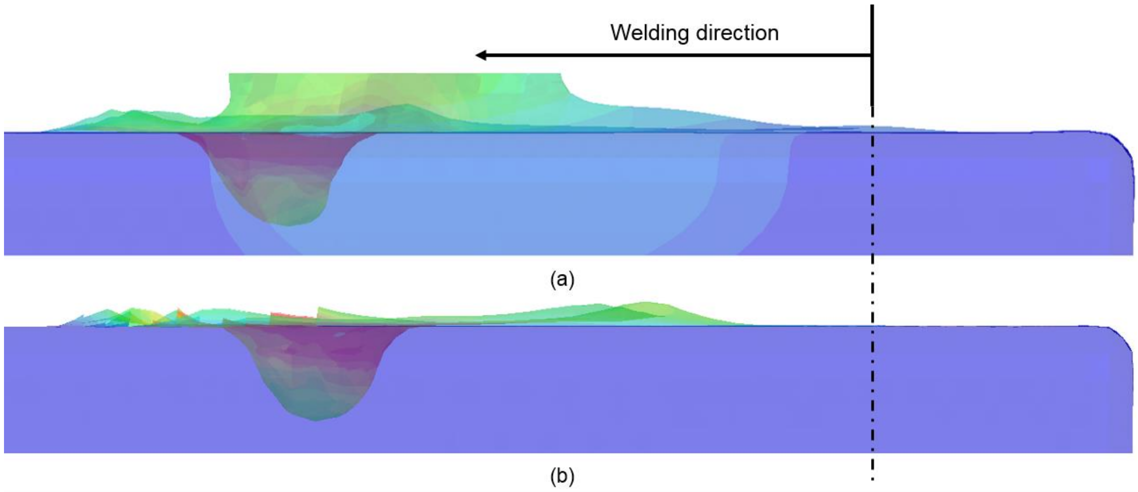

Figure 4.30: Visualisation of flash from the side view in the (a) slow weld model, (b) fast weld model.

In FSW, even small changes in the process parameters can generate certain defects in the weld joint [4.27]. The application of different process parameters in FSW helps to overcome these possible defects by analysing various changes during the process. Table 4.6 lists the key property differences between the two sets of weld models.

Table 4.6: Major findings from the numerical results for both models.

Weld model	Slow weld	Fast weld
Tool rotational speed	200 rpm	700 rpm
Traverse speed	120 mm/min	500 mm/min
Max. temperature achieved at Plunge	770°C	889°C
Max. temperature achieved at Dwell	994°C	1084°C
Max. temperature achieved at Traverse	964°C	1157°C
Flash formation	High	Low

4.3. Conclusions

A three-dimensional numerical model of FSW for low alloy steel grade DH36 was developed in Abaqus/Explicit software. Since the Johnson Cook's model exhibits an unrealistic melting temperature for the case of steel alloys, real-time temperature dependent material data have been used for the workpiece. By using the coupled Eulerian Lagrangian approach, both tool and workpiece were modelled as solid bodies and minimal assumptions were made for the boundary conditions. The model successfully predicted the temperature distribution, plastic strain, reaction forces, material flow and flash generation in all three stages, i.e. plunge, dwell and traverse. Use of experimentally generated temperature dependent DH36 properties provided an accurate behaviour of the complete welding process.

The results of two characteristic models with substantially different rotational and traverse speeds were discussed. The TMAZ was more symmetric in the slow weld model than the fast weld model. It was observed that the heat affected zone in the slow weld model was larger than the fast weld model in the traverse stage. The plastic strain was found to be greater in the slow weld model than the fast weld model with the plastic strain values being higher near the tool shoulder than the tool probe tip for both models. Reaction forces on the tool provided an estimate to reduce the wear on the tool during the welding process, hence improving the tool's life. The material flow in the TMAZ was improved by increasing the tool's rotational and traverse speeds. Major flash was observed on the retreating side of the slow weld model workpiece whereas the weld upper surface in the fast weld model demonstrated slight incomplete fusion. No flaws were detected in both models, which shows that the process is durable for diverse process parameters. The results from both models indicate that the fast weld parameters can be used where increased productivity with acceptable weld quality is desirable, and the slow weld parameters can be applied where excellent quality is preferred. All the results obtained from the software were in good agreement with the experimental findings.

4.4. References

[4.1] Toumpis A, Galloway A, Cater S, McPherson N. Development of a process envelope for friction stir welding of DH36 steel - A step change. Mater Des 2014;62:64–75. doi:10.1016/j.matdes.2014.04.066.

[4.2] Toumpis AI, Galloway AM, Arbaoui L, Poletz N. Thermomechanical deformation behaviour of DH36 steel during friction stir welding by experimental validation and modelling. Sci Technol Weld Join 2014;19:653–63. doi:10.1179/1362171814Y.0000000239.

[4.3] Toumpis A, Galloway A, Cater S, Micallef D, Camilleri D, Poletz N, et al. Advances in friction stir welding of steel – project HILDA. Transp. Res. Arena, Paris, France: 2014.

[4.4] Micallef D, Camilleri D, Toumpis A, Galloway A, Arbaoui L. Local heat generation and material flow in friction stir welding of mild steel assemblies. Proc Inst Mech Eng Part L J Mater Des Appl 2015;230:586–602. doi:10.1177/1464420715583163.

[4.5] Simulia 6.14. Abaqus Documentation. 23.2.3 Rate-Dependent Yield. 2014.

[4.6] MegaStir. Friction Stir Welding of High Melting Temperature Materials. 2013.

[4.7] Nandan R, Roy GG, Lienert TJ, DebRoy T. Numerical modelling of 3D plastic flow and heat transfer during friction stir welding of stainless steel. Sci Technol Weld Join 2006;11:526–37. doi:10.1179/174329306X107692.

[4.8] Ambroziak A, Winnicki M, Laska P, Lachowicz M, Zwierzchowski M, Lesniewski J. Examination of friction coefficient in friction welding process of tubular steel elements. Arch Metall Mater 2011;56:975–80. doi:10.2478/v10172-011-0107-8.

[4.9] Assidi M, Fourment L, Guerdoux S, Nelson T. Friction model for friction stir welding process simulation: Calibrations from welding experiments. Int J Mach Tools Manuf 2010;50:143–55. doi:10.1016/j.ijmachtools.2009.11.008.

[4.10] Al-Moussawi M, Smith A, Young AE, Cater S, Faraji M. Modelling of friction stir welding of DH36 steel. Int J Adv Manuf Technol 2017;92:341–60. doi:10.1007/s00170-017-0147-y.

[4.11] Simulia 6.14. Abaqus Documentation. 37.2.1 Thermal Contact Properties. 2014.

[4.12] Al-Badour F, Merah N, Shuaib A, Bazoune A. Coupled Eulerian Lagrangian finite element modeling of friction stir welding processes. J Mater Process Technol 2013;213:1433–9. doi:10.1016/j.jmatprotec.2013.02.014.

[4.13] Simulia 6.14. Abaqus Documentation. 14.1.1 Eulerian Analysis. 2014.

[4.14] Simulia 6.14. Abaqus Documentation. 6.3.3 Explicit Dynamics Analysis. 2014.

[4.15] Simulia 6.14. Abaqus Documentation. 27.1.4 Section Control. 2014.

[4.16] Simulia 6.14. Abaqus Documentation. 3.5.3 Parallel Execution in Abaqus/Explicit. 2014.

[4.17] Simulia 2016. Abaqus Documentation. 11.6.1 Mass Scaling. 2016.

[4.18] Li H. Coupled Thermo-Mechanical Modelling of Friction Stir Welding. University of Strathclyde, 2008.

[4.19] Dubourg L, Dacheux P. Design and properties of FSW tools : a literature review. 6th Int. Symp. Frict. Stir Weld., Saint-Sauveur: 2006, p. 2.

[4.20] Colegrove PA, Shercliff HR. 3-Dimensional CFD modelling of flow round a threaded friction stir welding tool profile. J Mater Process Technol 2005;169:320–7. doi:10.1016/j.jmatprotec.2005.03.015.

[4.21] Selvamani ST, Umanath K, Palanikumar K. Heat Transfer Analysis during Friction Stir Welding of Al6061-T6 Alloy. Int J Eng Res Appl 2011;1:1453–60.

[4.22] Jweeg M, Tolephih MH, M. MA. Effect of friction stir welding parameters (rotation and transverse) speed on the transient temperature distribution in friction stir welding of AA 7020-t53. ARPN J Eng Appl Sci 2012;7:436–46.

[4.23] Xu W, Liu J, Luan G, Dong C. Microstructure and mechanical properties of friction stir welded joints in 2219-T6 aluminum alloy. Mater Des 2009;30:3460–7. doi:10.1016/j.matdes.2009.03.018.

[4.24] Camilleri D, Micallef D, Mollicone P. Thermal stresses and distortion developed in mild steel DH36 friction stir-welded plates: An experimental and numerical assessment. J Therm Stress 2015;38:485–508. doi:10.1080/01495739.2015.1015856.

[4.25] Ulysse P. Three-dimensional modeling of the friction stir-welding process. Int J Mach Tools Manuf 2002;42:1549–57. doi:10.1016/S0890-6955(02)00114-1.

[4.26] Reynolds AP, Hood E, Tang W. Texture in friction stir welds of Timetal 21S. Scr Mater 2005;52:491–4. doi:10.1016/j.scriptamat.2004.11.009.

[4.27] He X, Gu F, Ball A. A review of numerical analysis of friction stir welding. Prog Mater Sci 2014;65:1–66. doi:10.1016/j.pmatsci.2014.03.003.

[4.28] Álvarez AI, Cid V, Pena G, Sotelo J, Verdera D. Assisted friction stir welding of carbon steel: Use of induction and laser as preheating techniques. Frict Stir Weld Process VII 2016:117–26. doi:10.1007/978-3-319-48108-1_13.

[4.29] Rai R, De A, Bhadeshia HKDH, DebRoy T. Review: friction stir welding tools. Sci Technol Weld Join 2011;16:325–42. doi:10.1179/1362171811Y.0000000023.

[4.30] Cho JH, Boyce DE, Dawson PR. Modeling strain hardening and texture evolution in friction stir welding of stainless steel. Mater Sci Eng A 2005;398:146–63. doi:10.1016/j.msea.2005.03.002.

[4.31] Morisada Y, Fujii H, Kawahito Y, Nakata K, Tanaka M. Three-dimensional visualization of material flow during friction stir welding by two pairs of X-ray transmission systems. Scr Mater 2011;65:1085–8. doi:10.1016/j.scriptamat.2011.09.021.

[4.32] Lorrain O, Favier V, Zahrouni H, Lawrjaniec D. Understanding the material flow path of friction stir welding process using unthreaded tools. J Mater Process Technol 2010;210:603–9. doi:10.1016/j.jmatprotec.2009.11.005.

[4.33] Mandal S, Rice J, Elmustafa AA. Experimental and numerical investigation of the plunge stage in friction stir welding. J Mater Process Technol 2008;203:411–9. doi:10.1016/j.jmatprotec.2007.10.067.

[4.34] Ji S, Jin Y, Yue Y, Zhang L, Lv Z. The effect of tool geometry on material flow behavior of friction stir welding of titanium alloy. Eng Rev 2013;33:107–13.

[4.35] Kumar K, Kailas S V. The role of friction stir welding tool on material flow and weld formation. Mater Sci Eng A 2008;485:367–74. doi:10.1016/j.msea.2007.08.013.

[4.36] Xu S, Deng X, Reynolds AP, Seidel TU. Finite element simulation of material flow in friction stir welding. Sci Technol Weld Join 2001;6:191–3. doi:10.1179/136217101101538640.

[4.37] Colegrove PA, Shercliff HR. Development of Trivex friction stir welding tool Part 1 – two-dimensional flow modelling and experimental validation. Sci Technol Weld Join 2004;9:352–61. doi: 10.1179/136217104225021670.

[4.38] Nandan R, Roy GG, Debroy T. Numerical simulation of three-dimensional heat transfer and plastic flow during friction stir welding. Metall Mater Trans A 2006;37:1247–59. doi:10.1007/s11661-006-1076-9.

5. Optimisation of the FSW process through laser assisted heating

During friction stir welding (FSW), maximum process forces occur on the tool in the plunge stage [5.1,5.2]. It was discussed in section 4.2.4 that the tool damage may be avoided by preheating the workpiece prior to the tool plunge. Therefore, this chapter describes the addition of a laser heat source to the already developed FSW model previously explained in Chapter 4. Additional numerical settings, such as the heat source configuration and process parameters, will be detailed based on the experimental setup from previously published work. Various models will demonstrate the feasibility of different heat source distances from the tool, and welding process parameters for the optimisation of the process. A comparison built on the reaction forces on the tool along with the temperature distribution and plastic strain in the workpiece will provide a suitable distance between the traversing tool and the laser heat source. Furthermore, in comparison to the maximum experimentally determined traverse speed of 500 mm/min on FSW of steel [5.2-5.4], laser assisted friction stir welding (LAFSW) prospects will be evaluated to increase the traverse speed, while achieving defect free welds. The numerical results will be discussed for all stages, plunge, dwell and the traverse, and compared by the previous research [5.5].

5.1. Model description

5.1.1. Laser heat source

LAFSW uses a supplementary heating source to sequentially preheat the material, before and during the FSW process. In addition to the conventional stages of FSW, a heating stage is present prior to the tool plunging into the workpiece, as shown in Figure 5.1. The total heat ‘Q’ generated during both FSW and LAFSW can be shown in the equations (5.1) [5.6] and (5.2), respectively.

$$Q_{FSW} = Q_{Friction\ between\ tool\ and\ workpiece} + Q_{Material\ deformation} \tag{5.1}$$

$$Q_{LAFSW} = Q_{FSW} + Q_{Laser} \tag{5.2}$$

$$Q_{Laser} = Initial\ preheating + Heating\ during\ the\ traverse\ stage \tag{5.3}$$

Initially, the laser heats a concentrated surface on the workpiece, following which the tool immediately starts to plunge and then dwell. In the traverse stage, the laser heating is applied on the workpiece through a moving heat source, as shown in Figure 5.1. The distance between the moving laser source and the tool is kept constant by maintaining the speed of both the tool and the laser source at a same rate. This way, the workpiece is preheated uniformly before the welding occurs. The temperature drop between the preheating and plunge stage is negligible, as the tool would take approx. 2-3 seconds for relocation to the welding position. For this reason, the tool is already placed on the plunge position in the current models to reduce the computational time.

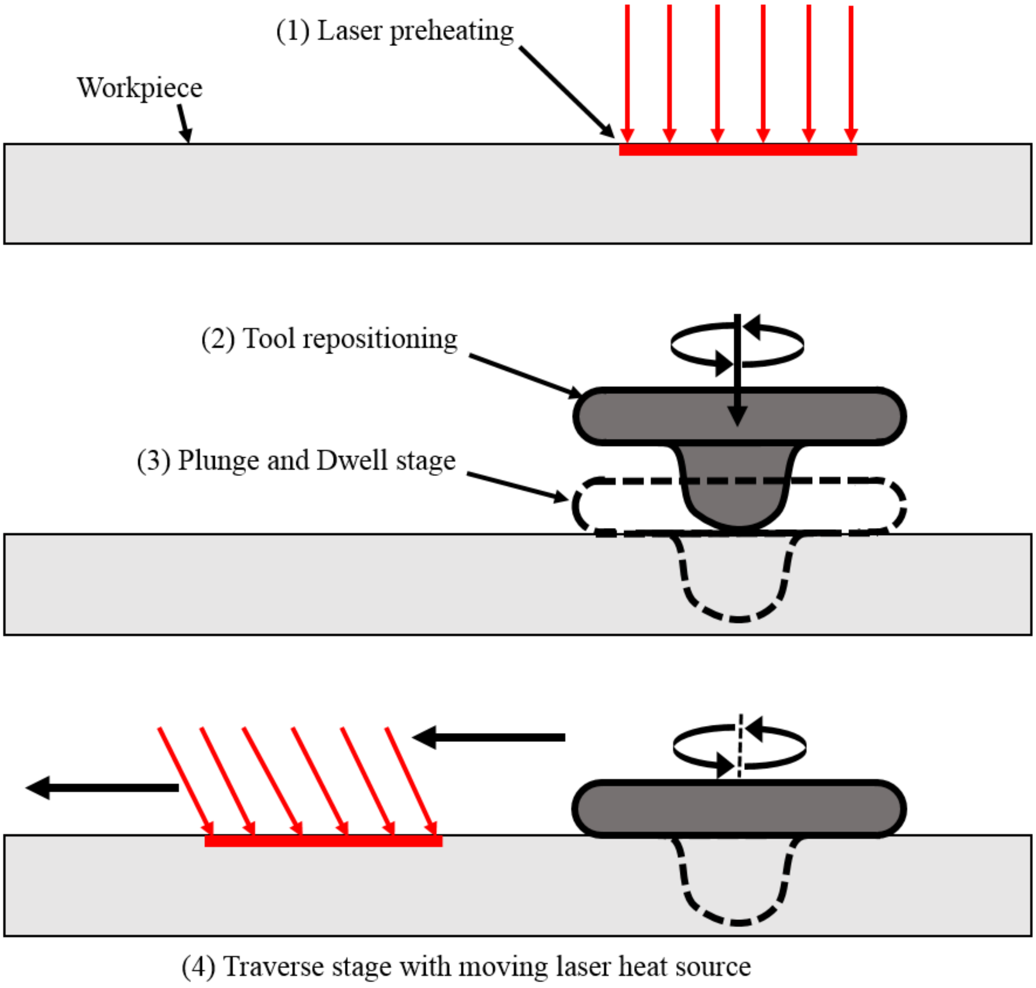

Figure 5.1: All stages of LAFSW.

In LAFSW, three factors greatly influence the process; laser power, heat source diameter and the distance between the heat source and the tool. Several experimental works [5.7-5.11] on laser heating have been performed using Nd:YAG (neodymium-doped yttrium aluminium garnet) laser generators. Therefore, the numerical models discussed in this chapter can be experimentally validated through, for example, a Nd:YAG laser generator. As concluded by Able et al. [5.12], increasing the average weld temperature and the size of HAZ not only affects the microstructure of the workpiece but also increases the overall power consumption. A power range of 150W – 2000W has been used for the application of laser heating for different materials [5.7,5.8,5.10,5.12-5.17]. The laser power during LAFSW should be able to raise the workpiece temperature more than 0.4 times the melting temperature of the material [5.18]. Different trials with various heat inputs showed that sufficient temperature up to 950^{o}C could be achieved on the surface by a heat source of 500 W maintained for 5 seconds. Therefore, a heat input of 500 W has been applied for all models, as configured by previous research groups [5.16,5.17]. Since FSW is a very localised process, the diameter of the heat source has been kept small (10 mm) so that only the workpiece surface area near the tool probe can be preheated. Since the typically recommended temperature of laser heating for steel LAFSW is 700^{o}C [5.18], the combination of the above described laser power and diameter achieved the desired temperature on the surface of the workpiece during the preheating stage.

5.1.2. Model settings

A three dimensional finite element model has been produced in Abaqus/Explicit. The Coupled Eulerian and Lagrangian (CEL) approach, thoroughly described in sections 3.1.2.2 and 4.1, has been applied in the current models as well, which enhanced the ability to measure large deformations in the models. Similar temperature dependent material properties from section 4.1.1 have been used for the respective materials. The coupled structural and thermal elements allowed the models to calculate the thermal and structural results, simultaneously. All geometrical dimensions have been kept the same from section 4.1.2 for both FSW and LAFSW models to observe an accurate comparison between them. Initial and boundary conditions have been applied to replicate the real life conditions. All model settings were replicated from the fast weld model [5.5], as explained in section 4.1.3.

A commonly used technique for modelling the moving laser source, named as the “DFlux” routine, is not available in the Abaqus/Explicit [5.19]. Therefore, an alternative approach was configured in the model by discretising the traverse step of LAFSW into several sub steps. A specified surface on the workpiece was heated in every sub step for a very short period. The laser heat was then resurfaced by slight movement in a linear direction for the next sub step, as shown in Figure 5.2. Hence, a smoother linear motion of the laser heating was achieved during the whole traverse stage due to very short time duration in each sub step.

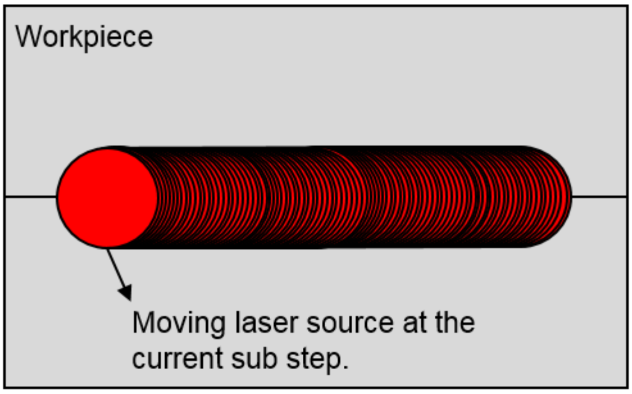

Figure 5.2: Illustration of the moving laser source by creating new surfaces in each sub step.

Like FSW, visualisation of the material flow in LAFSW is crucial as the process contains high plastic deformation [5.6]. Four sets of tracer particles were defined in all models so that the material flow could be thoroughly observed in all stages of the welding, as shown previously in Figure 4.7. The first set is located where the tool plunges and then dwells, whereas other sets are placed in the middle of the traverse stage. Double precision was selected to improve the accuracy of the simulations.

5.1.3. Process parameters

Since the aim of the current research is to consider the potential advantages of using a supplementary laser heat source, a diverse range of process parameters have been selected and modelled to compare different heat source distances. Three laser heat source distances from the tool have been modelled and discussed, so that the reaction forces on the tool could be minimised. The position control method has been applied in the models to achieve an accurate tool probe depth. Table 5.1 shows the process parameters for all the models discussed in the present study.

The model FSW-1 has been validated through the experimental data [5.5], and discussed in Chapter 4 (named as the fast weld model). Therefore, this has been set as a benchmark for modelling LAFSW, and obtaining an appropriate heat source distance so that the process parameters could be maximised. Since the initial position of the tool on the workpiece has been changed to analyse the complete effect of preheating, the reaction forces on the FSW-1 model have been recalculated and discussed in this model. From LAFSW-1 to 3, the weld speeds have been kept constant to accurately analyse the effect of changing the distance between the moving laser heat source and the tool during the traverse stage. The weld process parameters have been optimised to achieve a defect-free weld after a suitable heat source distance was found by observing the weld quality and the reaction forces on the tool probe tip, and the temperature distribution, plastic strain and the material flow in the workpiece.

Table 5.1: Process parameter specifications to determine the suitable heat source distance from the tool.

Model ID	Plunge stage		Dwell stage		Traverse stage	
	Tool rotational speed (rpm)	Tool feed rate in downward direction (mm/min)	Tool rotational speed (rpm)	Rotating speed (rpm)	Tool traverse and laser speed (mm/min)	Distance between moving laser and tool (mm)
FSW-1[5.5]*	800	100	700	700	500	-
LAFSW-1	800	100	700	700	500	20
LAFSW-2	800	100	700	700	500	30
LAFSW-3	800	100	700	700	500	40

* does not include the laser source.

5.2. Results and discussion

Several numerical models were simulated with varying auxiliary heat source distances and process parameters. However, only the notable results have been presented and discussed in this chapter. As shown in Table 5.1, the effect of changing the heat source distance has been compared by FSW-1, while keeping all other process parameters constant. A parametric view of a LAFSW weld is shown in Figure 5.3. The total duration of the preheating, plunge, dwell and traverse stages is 5, 3.56, 4 and 5.4 seconds, respectively.

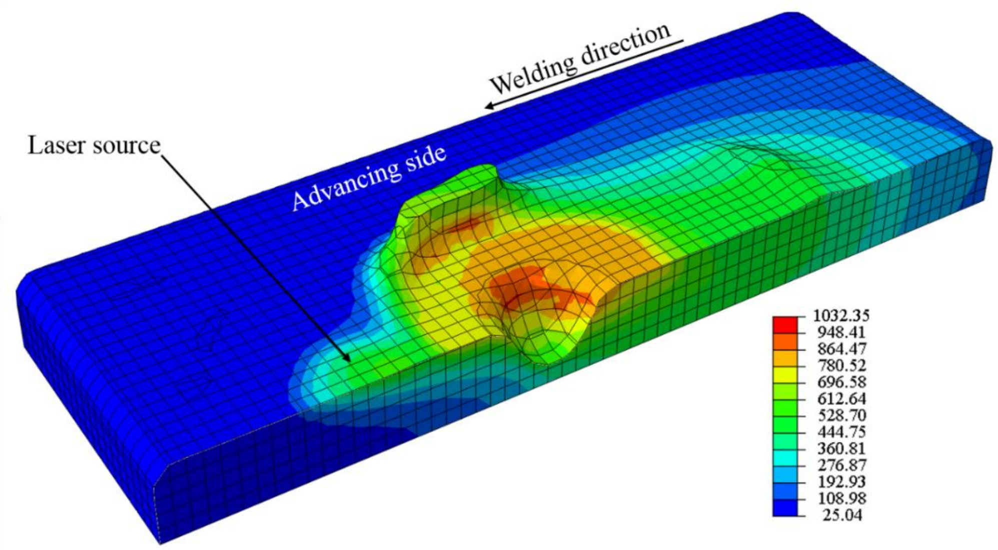

Figure 5.3: A Parametric view of LAFSW-1 featuring the temperature distribution in ^{o}C (Tool rotation: Anticlockwise direction).

5.2.1 Reaction forces

In both FSW and LAFSW models, the maximum reaction forces were measured at the lower part of the tool probe. The reaction forces on the probe tip of the tool have been calculated and presented in Figure 5.4. Since the tool was not in contact with the workpiece during the preheating stage, the reaction force results have only been discussed for the plunge, dwell and traverse stages. Unlike FSW where the maximum forces occur on the tool during the plunge stage [5.20], all LAFSW models had less reaction forces on the tool during the plunge stage as compared to the traverse stage, also seen in Figure 5.4. During the first 2.7 seconds of the plunge stage, the reaction force on the probe tip increased linearly. The maximum reaction force of 120 kN is calculated right after the tool fully penetrated into the workpiece for the FSW-1 model (t=3.56 s). An average peak reaction force of 55 kN has been obtained for the laser assisted models during the plunge stage. The preheating of the workpiece reduced the reaction forces in LAFSW by an average difference of 65 kN compared to the conventional FSW. This shows a reduction of approx. 55% in the reaction forces on the tool during the plunge stage with the laser assistance to FSW. Similar results up to 33% and 40% reduction in the downward forces on the tool during the plunge and the traverse stage have been achieved for the LAFSW of carbon steel by Alvarez et al. [5.1]. In another recent research study [5.21], the force on the tool was shown to decrease by up to 43% with the LAFSW of aluminium alloy 6061.

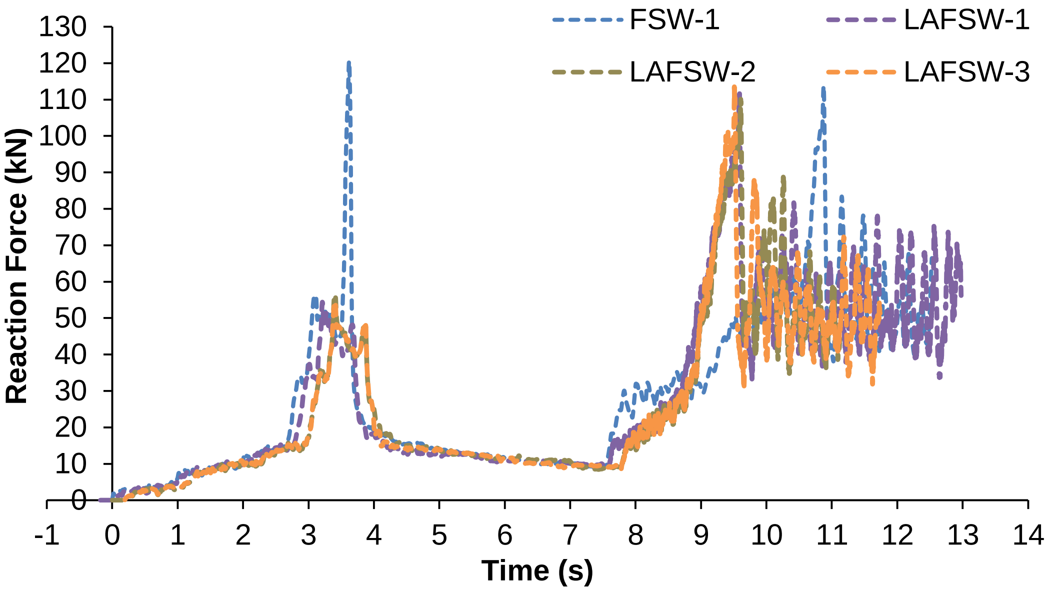

Figure 5.4: Reaction forces comparison on the tool tip in the FSW and LAFSW models.

During the dwell stage, the preheating energy had already softened the workpiece material, hence the tool probe observed a stabilised reaction force. As the tool started traversing, there was a linear increase in reaction force from 7.6 to 8.8 seconds. This phenomenon occurred because the heat, which was transferred previously into the HAZ, dissipated to the surroundings, hence creating a larger HAZ in the traverse stage. The increased preheating assisted in lowering the reaction forces on the tool at the initiation of the traverse stage. This effect of preheating during the dwell stage has also been reported by Yu et al [5.22]. After the tool no longer experienced any heat effect from the previous stages, the reaction forces were stabilised, yet minimised, due to the moving laser heating ahead of the tool.

Among each of the LAFSW models discussed in this study, the least reaction force was found in the model type LAFSW-1 which comprised of a distance of 20 mm between the laser heating source and the tool rotating axis. This shows that the advantages of heat assistance could be maximised by maintaining a minimum distance between the heat source and the FSW tool. Figure 5.5 represents the rectangular components of the reaction forces for FSW-1 and LAFSW-1 models. It can be observed that the Z-force (RF-Y) was reduced to -55 kN in the plunge stage due to the effect of laser heating, whereas RF-X and RF-Z had no significant changes in their values. All force components followed a similar pattern in the dwell stage due to the minimal influence of the laser heating. In the traverse stage, RF-Y observed an initial linear increase as discussed previously for the Figure 5.4. A substantial difference between the forces of FSW and LAFSW was not observed during the traverse stage. This was due to the fact that the heat generated by the laser heat source did not greatly influence the bottom surface of the workpiece.

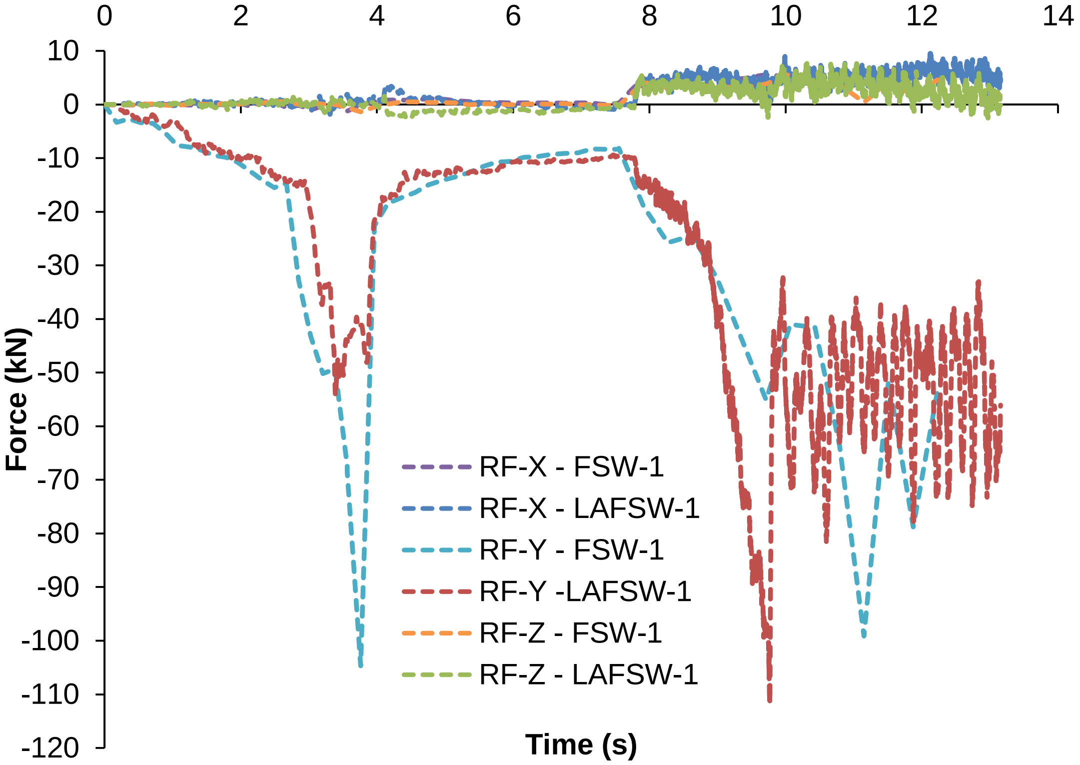

Figure 5.5: Reaction forces components comparison for FSW-1 and LAFSW-1 models.

5.2.2 Temperature distribution

Figure 5.6 shows the temperature distribution from the top and the side view for LAFSW welding configurations during the preheating stage. A peak temperature of 953.44 °C was calculated in the preheating stage. Since no changes have been made in the preheating stage for all models, a temperature of 224°C is recorded at 1.6 mm from the bottom surface of the workpiece. This shows that sufficient heat could be dissipated in the tool plunge region within 5 seconds of heating before the plunge stage. The heat from the laser preheating can therefore assist in the softening of the workpiece before the tool plunge, also reported by Fei et al. [5.23].

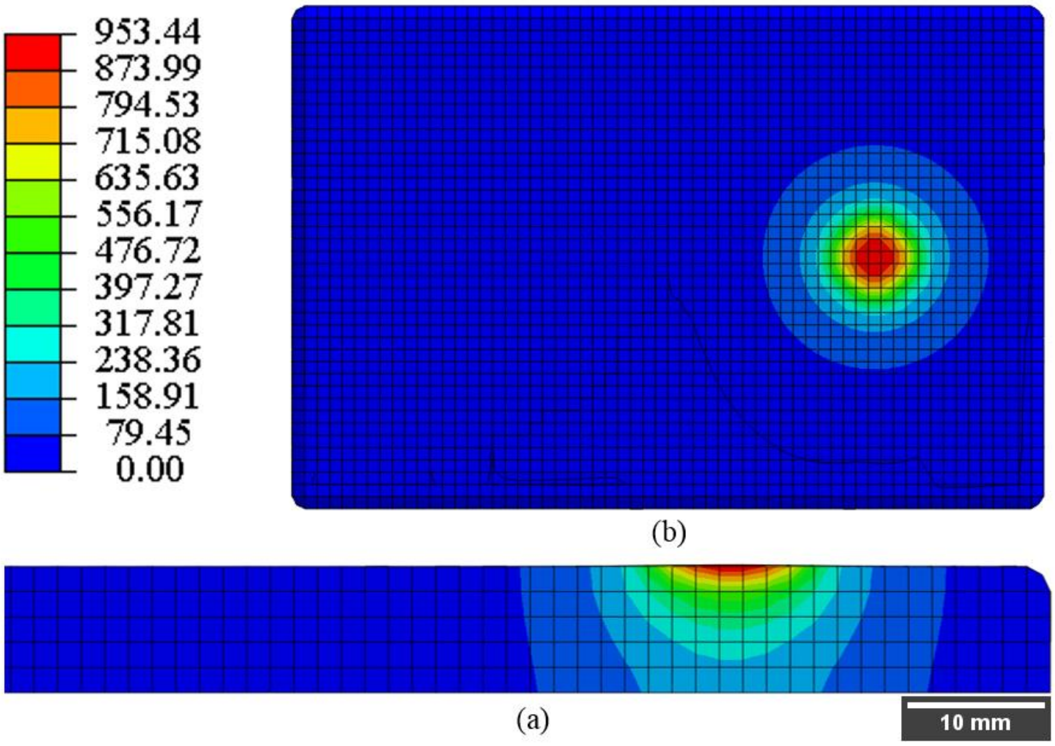

Figure 5.6: Temperature distribution in ^{o}C in LAFSW after the laser preheating/before the plunge stage; (a) side view of the weld model, (b) top view – Not set according to the scale.

In the dwell stage, the temperature in the TMAZ was higher in LAFSW compared to FSW as a reasonable amount of heat was already present in the workpiece that increased the temperature in the TMAZ and HAZ regions (Figure 5.7). This suggests that the total duration of the dwell stage could be reduced by the use of laser assistance without even compromising the overall temperature distribution in the weld region.

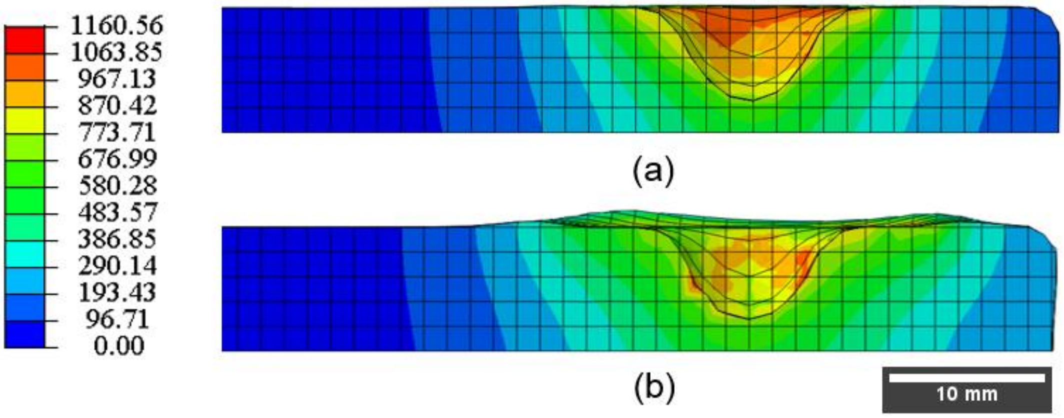

Figure 5.7: Temperature distribution in ^{o}C at the end of the dwell stage; (a) Side view of the LAFSW-1 model, (b) side view of the FSW-1 model. (Tool rotation: Anticlockwise direction).

The top views of the temperature distribution for all models during the traverse stage are shown in Figure 5.8. The temperature contours of laser heating created a prolonged effect due to the continuous movement along with the traversing tool (Figure 5.8). A higher temperature was observed in the advancing side (AS) of all welds as compared to the retreating side (RS). This asymmetric temperature distribution in the welding region demonstrates that the rotational direction of the tool also assists in the heat flow from AS to RS.

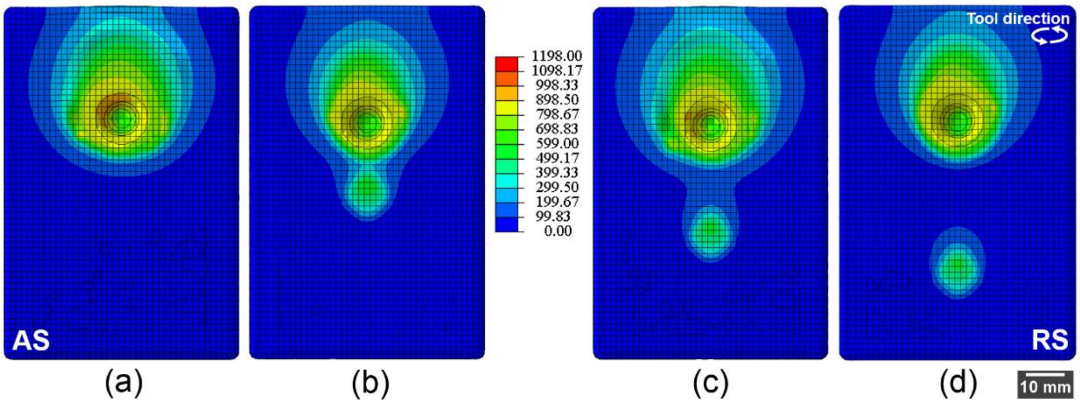

Figure 5.8: Temperature distribution in ^{o}C in the top views at traverse stage of; (a) FSW-1 model without laser heating, (b) LAFSW-1 model with 20 mm heat source distance, (c) LAFSW-2 model with 30 mm heat source distance, (d) LAFSW-3 model with 40 mm heat source distance.

A wider temperature profile is observed in the cross sectional view of LAFSW-1 (Figure 5.9 (b)) as compared to the other models. The laser heating creates an increased temperature range near the tool [5.24], which can be seen in Figure 5.9. A sufficient amount of heat is dissipated to the bottom surface of the workpiece, which may assist in an increased material deformation near the tool probe, hence reducing any potential weld defects. This also establishes the feasibility of using a smaller heat source distance from the welding tool. Daftardar [5.15] also concluded that the temperature distribution in the workpiece was increased when there was a minimum distance between the heat source and the tool.

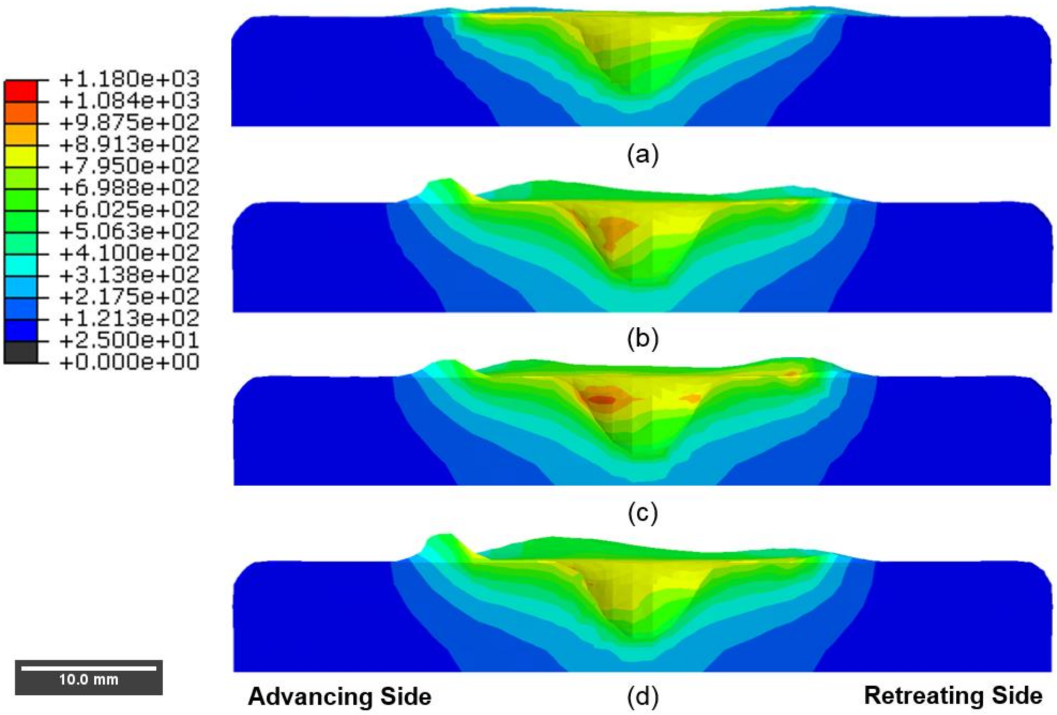

Figure 5.9: Temperature distribution in ^{o}C in the cross sectional views at traverse stage of (a) FSW-1 model, (b) LAFSW-1 model, (c) LAFSW-2 model, (d) LAFSW-3 model. (Tool rotation: Anticlockwise direction).

Figure 5.10 demonstrates the temperature distribution in each of the models discussed in the Table 5.1, with respect to the displacement along the weld line. A comparatively higher surface temperature of 580^{o}C was recorded when the laser heating distance was set at 20 mm from the tool's centre. This also shows the potential application of using a minimum heat source distance to achieve higher temperature gradient.

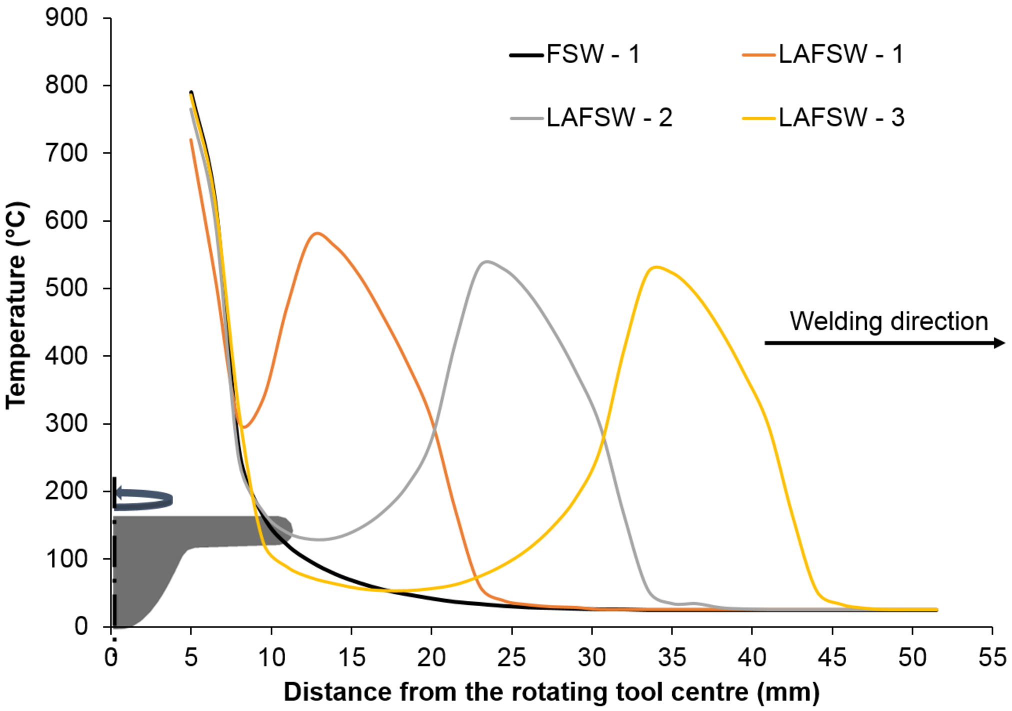

Figure 5.10: Surface temperature comparison for all discussed models along the welding line in front of the FSW tool.

5.2.3. Plastic strain

The equivalent plastic strain demonstrates the material's deformation in the workpiece, hence identifying the TMAZ and the HAZ in the welds. A relatively larger amount of plastic strain was observed when the distance between the laser heat source and the tool was the shortest. The outskirts of the plastic strain profile appeared to be very irregular and rough when visualising from the workpiece's top surface. This is highly likely to be due to the excessive softening of the workpiece's top surface by the laser heating for comparatively low traverse speeds. The application of the laser assistance resulted in an increased flash generation, as shown in Figure 5.11. The undesirable flash can be reduced by increasing the traverse speed, as explained later in section 5.2.5. Moreover, the workpiece's region experiencing the deformation was larger in the models with the heat source than the typical FSW-1 model. The laser heating source softened the material prior to the welding tool to an extent that made the stirring easier without altering any other process parameter.

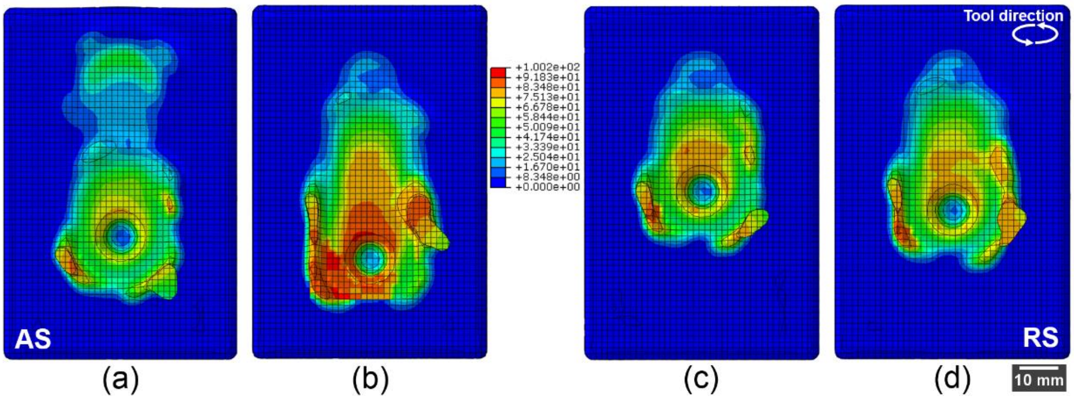

Figure 5.11: Equivalent plastic strain in the top views of; (a) FSW-1 model without laser heating, (b) LAFSW-1 model with 20 mm heat source distance, (c) LAFSW-2 model with 30 mm heat source distance, (d) LAFSW-3 model with 40 mm heat source distance.

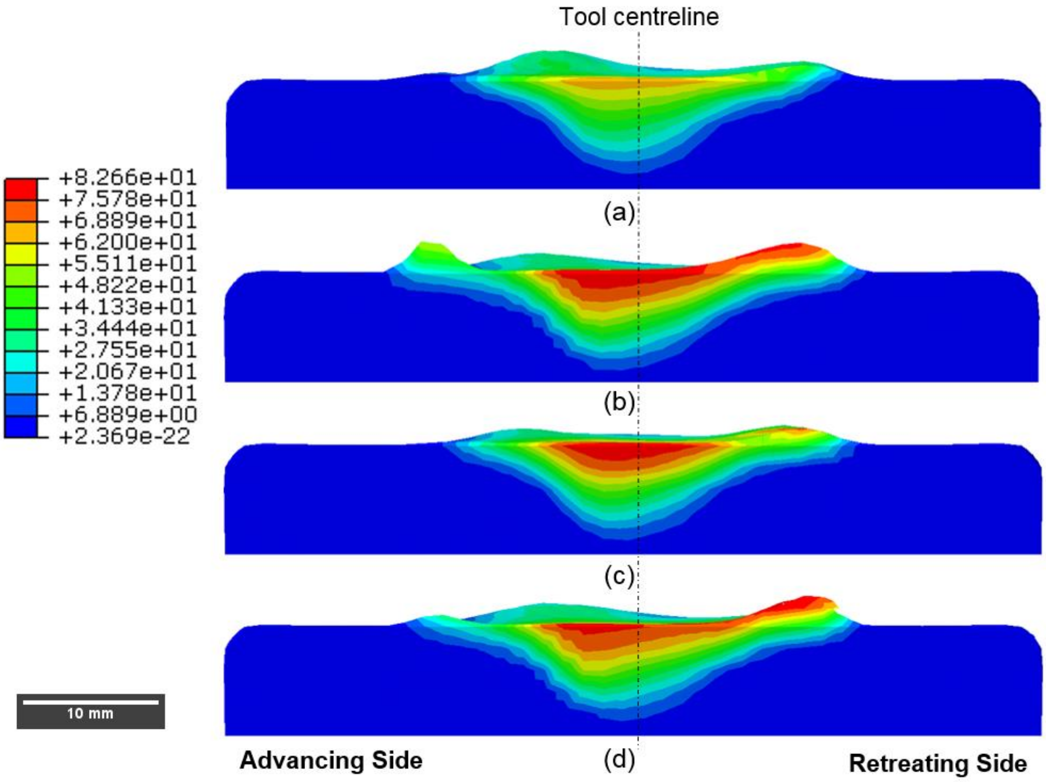

Figure 5.12: Equivalent plastic strain in the cross sectional views of; (a) FSW-1 model without laser heating, (b) LAFSW-1 model with 20 mm heat source distance, (c) LAFSW-2 model with 30 mm heat source distance, (d) LAFSW-3 model with 40 mm heat source distance. (Tool rotation: Anticlockwise direction).

The cross sectional view of the friction stir welds assists in determining the presence of any weld defects by visualising the plastic strain in that specific region. It can be seen in Figure 5.12 that the material in the TMAZ is deformed in a more irregular manner with the laser heating. The highest plastic strain of 82.66 is achieved in all the three models with laser heating, while the LAFSW-1 model has on average the largest area amassing the high plastic strains in the weld zone among all other models. A relatively higher plastic strain at the bottom side of the LAFSW-1 model was observed as compared to the other models, which also justifies the applicability of a smaller distance between the laser heat source and the welding tool.

5.2.4. Material flow

The material movement in FSW – 1 and LAFSW – 1 models was visualised by the assistance of tracer particles present in the workpieces. The initial positions for all tracer sets, shown in Figure 4.7, captured the material movement in terms of mesh nodes during the plunge and traverse stages. Figure 5.13 represents the top view of the material flow in the workpiece for both models during the plunge stage by the help of Tracer set - 1. To further assist in visualising the material flow during FSW/LAFSW, the workpiece material is not shown in the figures of this section. Due to the insufficient amount of thermal softening of the material in the conventional FSW [5.25], there was less material flow in the FSW-1 model during the plunge stage as compared to the LAFSW-1 model. As the temperature became higher in the plunge region, the tracer particles exhibiting the material flow started to swirl in the anticlockwise direction as seen in Figure 5.13.

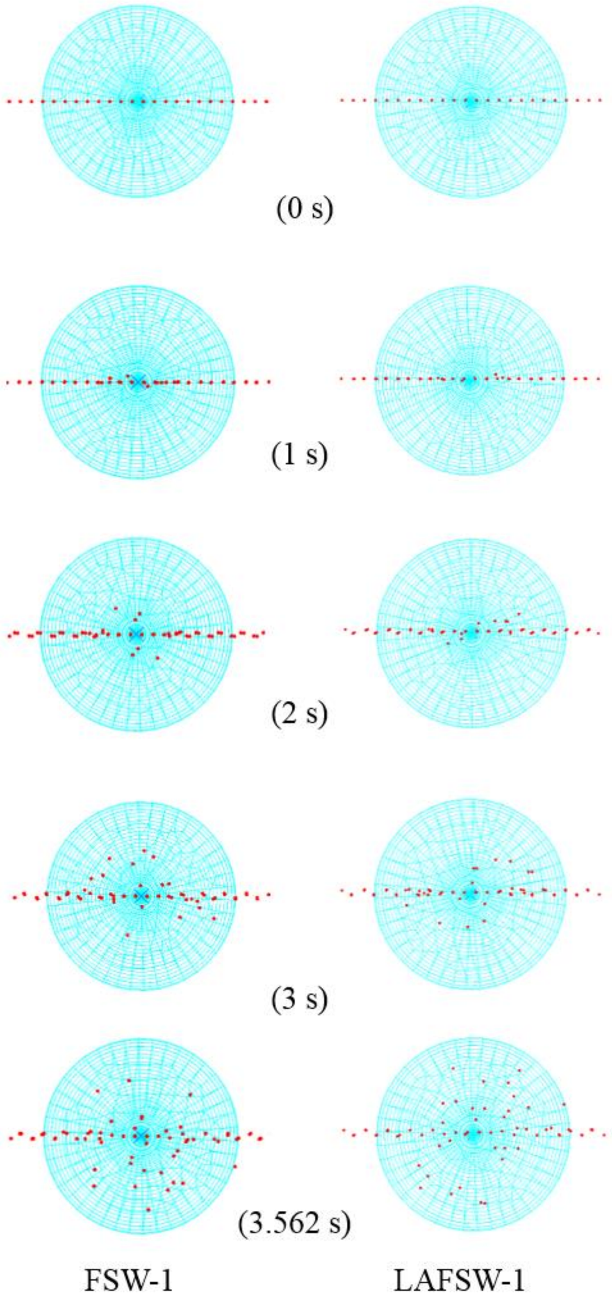

Figure 5.13. Material flow comparison in FSW-1 and LAFSW-1 models during the plunge stage. (Tool rotation: Anticlockwise direction).

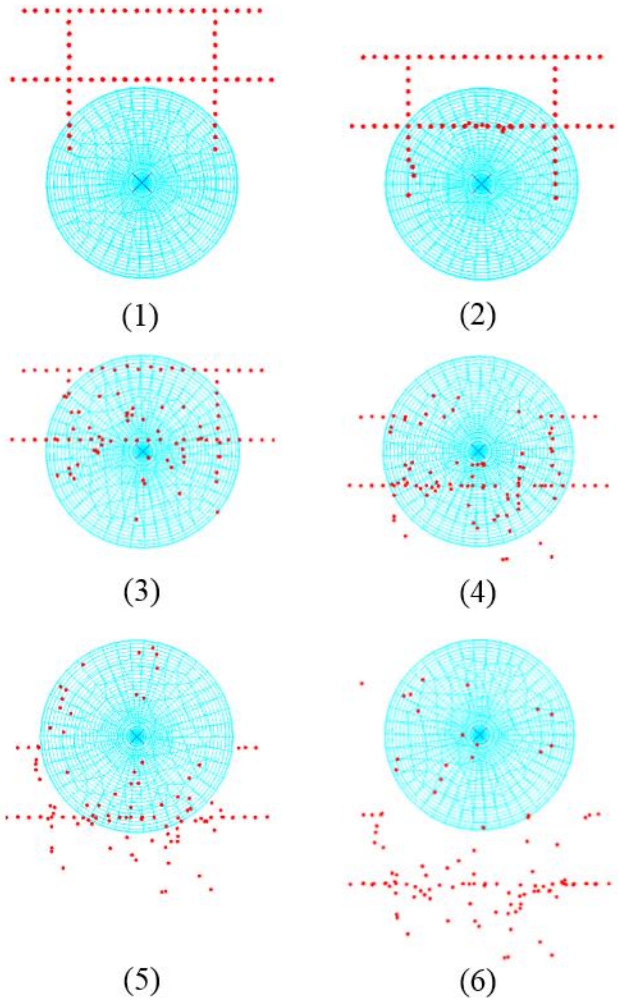

Figure 5.14. Material flow in the FSW-1 model during the traverse stage (1 to 6 represents periodic movement of the tool to the upward direction - Tool rotation: Anticlockwise direction).

Figure 5.14 and 5.15 represent the top view of the material flow in the workpiece for the FSW-1 and LAFSW-1 models, respectively, during the traverse stage by the help of Tracer sets – 2, 3 and 4. The tool is shown as traversing in the upward direction in Figure 5.14 and 5.15. When the tool started traversing in the weld direction, the workpiece material located slightly ahead of the tool's geometry began to follow the movement of the tool, swirling from the advancing side to the retreating side. It was also concluded by Guerra et al. [5.26] that the material in the advancing side rotates and moves along the tool. The material flow is typically reduced due to the increased strength of the stir zone [5.27]. However, the tracer particles movement was improved in the LAFSW-1 model during the traverse stage. This was due to the continuous heating in the workpiece region prior to the tool traverse. Sinclair et al. [5.21] reported that the material flow was improved due to the assistance of the preheating during FSW. Similar results of an increase in material flow have been reported by Bang et al. [5.28] by using a preheating source to weld aluminium Al6061-T6 to steel STS304. Since sufficient material flow is required to obtain defect free welds [5.29], the material flow visualisation of models illustrates that the addition of laser heat source increases the material flow in the workpiece during the plunge and the traverse stage, also concluded by Padhy et al. [5.6].

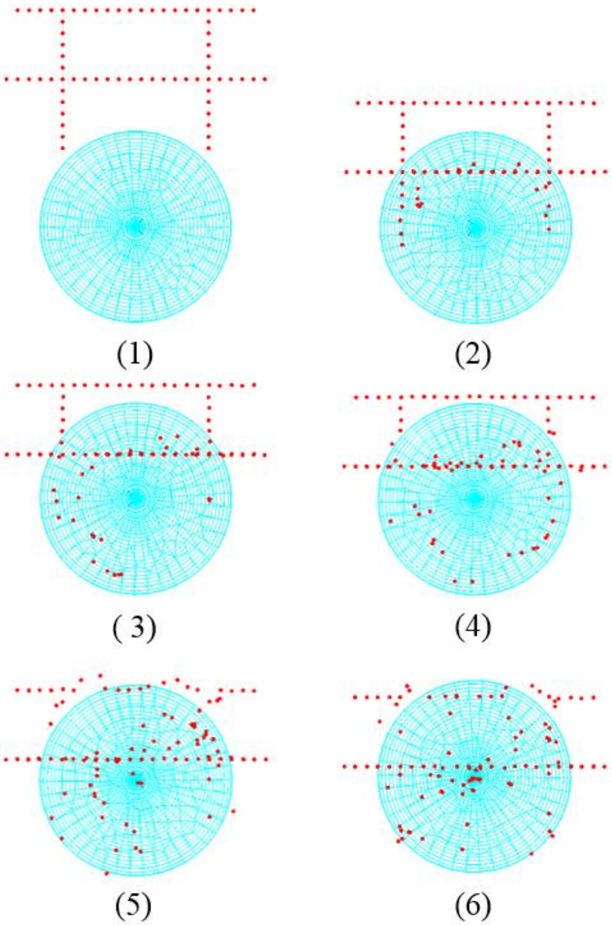

Figure 5.15. Material flow in the LAFSW-1 model during the traverse stage (1 to 6 represents periodic movement of the tool to the upward direction - Tool rotation: Anticlockwise direction).

5.2.5. Optimised LAFSW process parameters

Besides visualising the material flow during the whole process, which cannot be achieved experimentally, another significant advantage of the numerical simulation of FSW/LAFSW is to guide the experimental procedures by providing optimised process parameters for excellent quality welds at high welding speeds. Considering the economic aspects in the industrial sector, it is vital to improve the traverse speed of the process [5.30]. The temperature distribution in the workpiece (Figure 5.8 and 5.9) revealed that relatively more heat was dissipated in the TMAZ and HAZ in the LAFSW-1 model. In addition, Figure 5.4 demonstrated that the lowest reaction force was calculated with the distance of 20 mm for all weld stages. This demonstrated that a distance of 20 mm is appropriate when applying the laser heating with FSW as compared to other distances. The joining of 1 mm thick dissimilar metals (steel DC04 and aluminium AA6061) through LAFSW was optimised by Merklein et al. [5.31]. A traverse speed up to 2000 mm/min was reported by applying 55% of the total radiation through laser on the steel [5.31]. Therefore, attempts have been made in the current research to increase the traverse speed for steel LAFSW. As the FSW process is highly sensitive to the alterations in rotational speeds at increased traverse speeds [5.3], several models with different process parameters have been selected and simulated, for both FSW and LAFSW, to obtain defect-free welds with substantially increased traverse speed. Potential defects in the workpieces have been analysed, and their results have been presented in the Table 5.2. A fixed distance of 20 mm between the moving heat source and the tool has been used for all LAFSW models, discussed in the Table 5.2.

Table 5.2. Process parameters specifications for models for the optimisation of LAFSW.

Model name	Process Parameters		Presence of defects
	Traverse speed (mm/min)	Rotational velocity (rpm)	
FSW-1 [5.5]	500	700	No
FSW-2	1000	1000	Yes

LAFSW-4	700	700	No
LAFSW-5	900	700	No
LAFSW-6	1000	700	No
LAFSW-7	1200	700	Yes
LAFSW-8	1000	1500	Yes
LAFSW-9	1000	1800	No
LAFSW-10	1500	1800	No
LAFSW-11	2000	2000	Yes
FSW-3	1500	1800	Yes

Since a maximum traverse speed of 800 mm/min has been achieved by laser preheating in FSW of S45C steel [5.8], numerical attempts have been made in the present research to increase the traverse speed by the application of laser heating. No defects were observed in the conventional FSW until the traverse speed was increased to 1000 mm/min (Table 5.2). Root flaws and other surface defects appeared in the FSW-2 model. To prevent these issues, the LAFSW models were simulated with increased process parameters (LAFSW-4 to 11). It was observed that a weld of acceptable quality could be obtained up to 1500 mm/min of traverse speed with the laser heat assistance. Therefore, the numerical results of the LAFSW-10 model will be discussed and compared with the conventional FSW-1 model in detail.

5.2.5.1. Reaction forces

The reaction forces during the plunge stage do not change in either of the LAFSW models, as the rotational and the plunge speed is kept constant, as shown in Figure 5.16. The dwell rotational speed of the LAFSW-10 model is increased to 1300 rpm, reducing the reaction forces on the tool during the dwell stage. This demonstrates that increasing the rotational speed does not adversely influence the tool with the application of preheating the workpiece. Despite the fact that the moving heat source has a minimal effect on the bottom side of the tool probe, as mentioned in section 5.2.1, the reaction forces in LAFSW-10 during the traverse stage are minimum (25 kN) as compared to FSW-1 and LAFSW-1. The traverse region of LAFSW-10 is comparatively shorter due to the increased traverse speed.

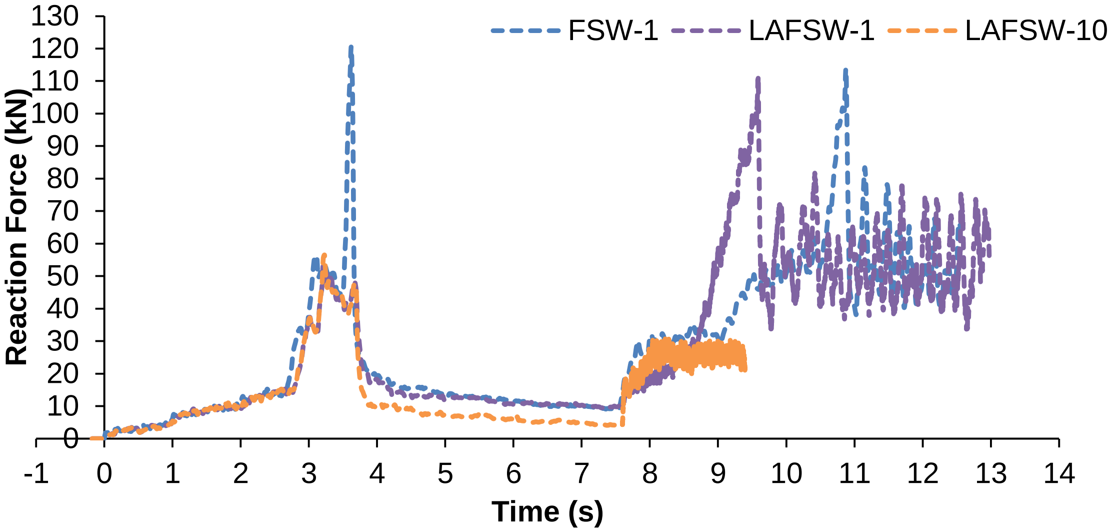

Figure 5.16: Reaction force comparison on the tool tip in the FSW-1, LAFSW-1 and the optimised LAFSW-10 models.

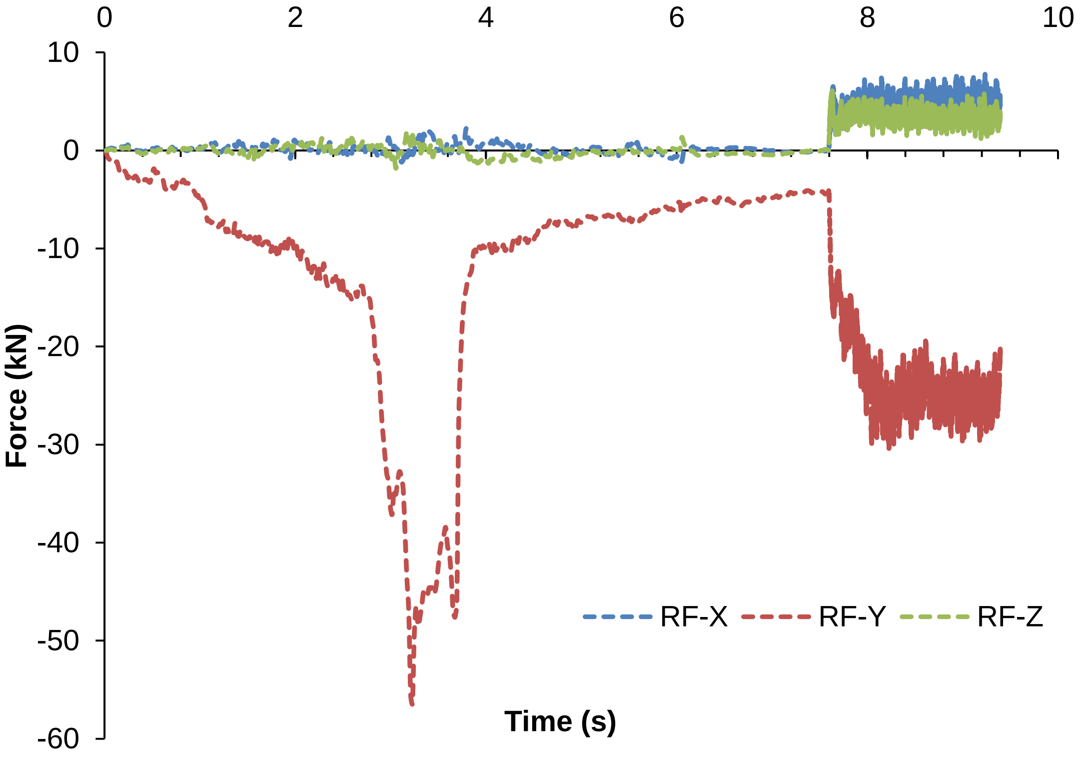

Figure 5.17: Reaction forces components for the LAFSW-10 model.

The components of the reaction forces in the LAFSW-10 model can be seen in the Figure 5.17. The X and Z-forces (RF-X and RF-Z, respectively) appeared to be almost same as the LAFSW-1 model forces from the Figure 5.5. However, the Y-force (RF-Y) was reduced up to an average of -25 kN, as compared to the -55 kN in the LAFSW-1 model during the traverse stage. In addition, the amplitude of all force components experienced less wave disturbances due to the increased process parameters. This suggests that the optimised process parameters can increase the tool's life, hence reducing the process cost [5.30].

5.2.5.2. Temperature distribution

Figure 5.18 shows the temperature distribution of the optimized LAFSW-10 model with a traverse speed of 1500 mm/min and rotational speed of 1800 rpm. A relatively narrower weld zone is produced due to the increased traverse speed than the models with the traverse speed of 500 mm/min.

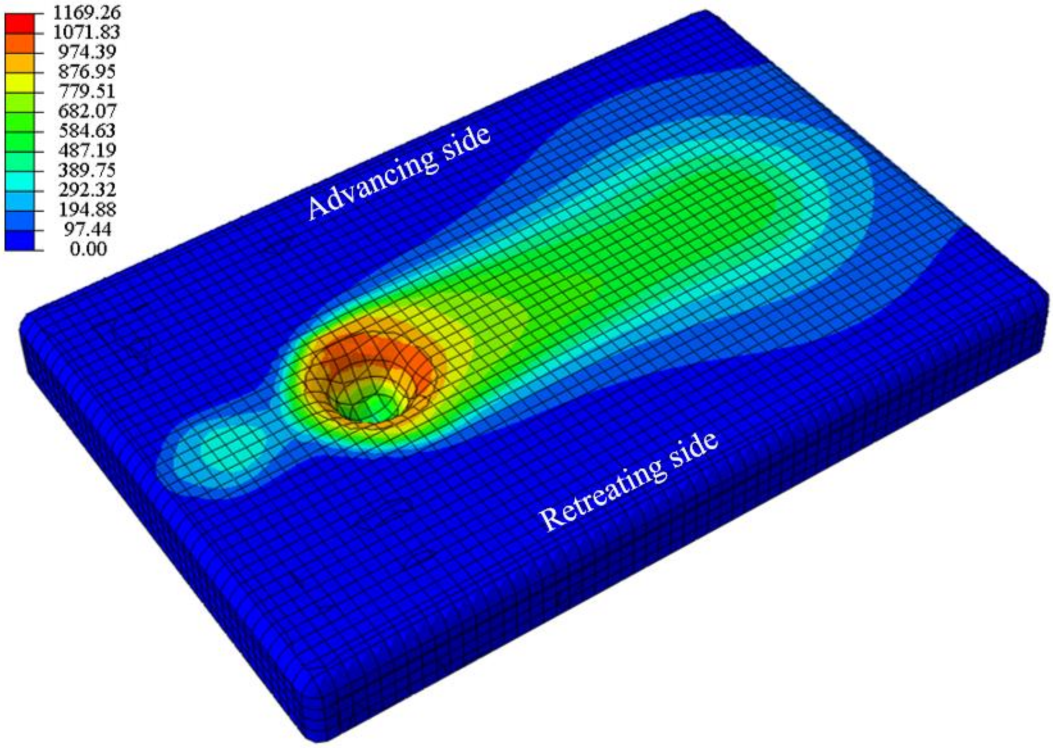

Figure 5.18: Temperature distribution in ^{o}C in the parametric view with increased process parameters in the LAFSW-10 model (Tool rotation: Anticlockwise direction).

A temperature distribution comparison has been made between the FSW-1 and LAFSW-10 models for the plunge stage, as shown in Figure 5.19. Both models follow a similar temperature profile, with the LAFSW-10 model having relatively higher values. The dissipated heat in the preheating stage has raised the temperature values at the bottom side of the workpiece during the plunge stage. This has helped in stirring the material around the tool, more efficiently. A maximum temperature of 902°C is achieved during the plunge stage of the LAFSW-10 model.

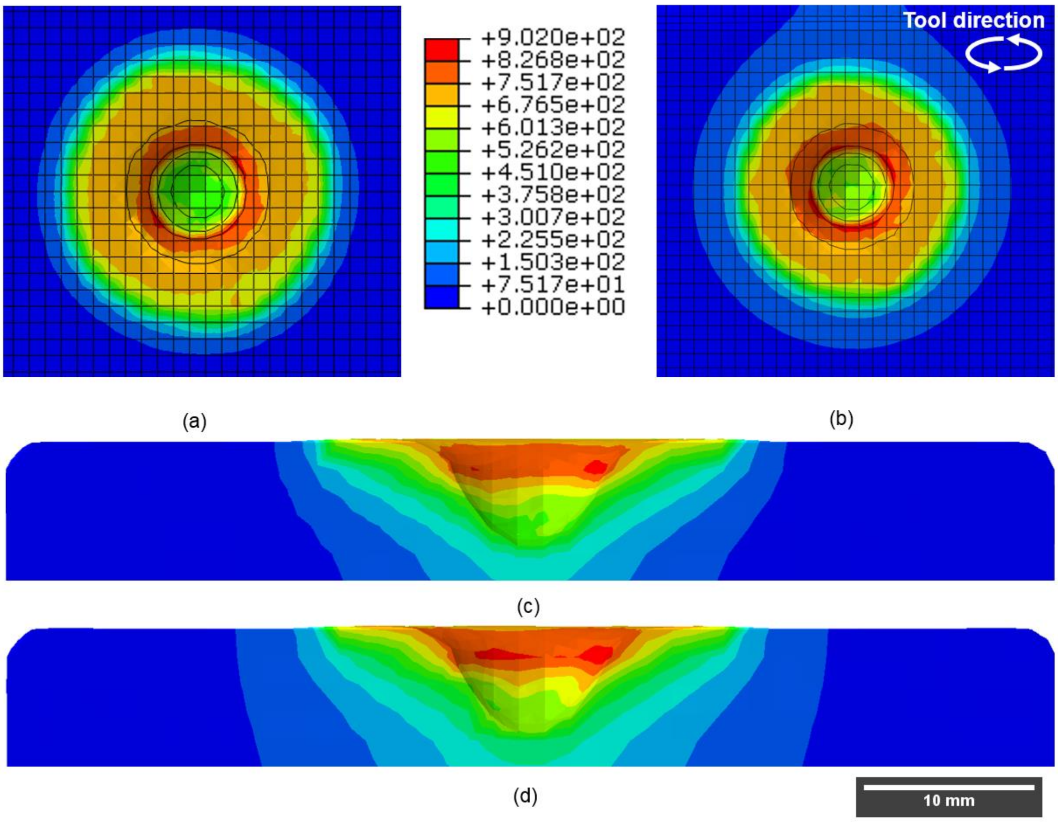

Figure 5.19: Temperature distribution in °C at the end of the plunge stage; (a) Top view of the FSW-1 model without laser heating, (b) Top view of the optimised LAFSW-10 model, (c) Cross sectional view of the FSW-1 model and (d) Cross sectional view of the LAFSW-10 model. (top views are not set according to the scale).

The increased rotational speed raised the temperature in the TMAZ and HAZ, as discussed by previous researchers [5.32,5.33]. An elevated temperature of 1157°C was achieved on many locations at the tool and the workpiece contact during the dwell stage, as shown in Figure 5.20. However, the overall temperature profile in the LAFSW-10 was not horizontally stretched, as compared to FSW-1. This can be justified by the already raised temperature values at the end of the plunge stage. In addition, a relatively less flash was observed during the dwell stage when the process parameters are optimised with the laser assistance.

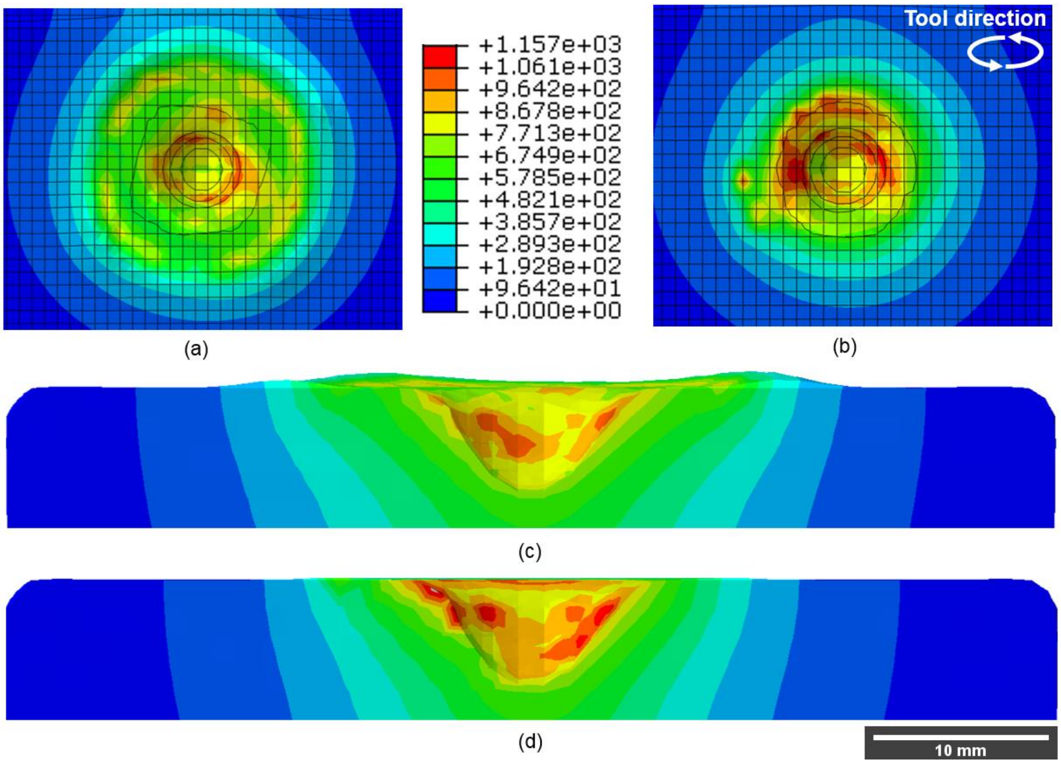

Figure 5.20: Temperature distribution in ^{o}C at the end of the dwell stage; (a) Top view of the FSW-1 model without laser heating, (b) Top view of the LAFSW-10 model, (c) Cross sectional view of the FSW-1 model and (d) Cross sectional view of the LAFSW-10 model. (top views are not set according to the scale).

The temperature was relatively higher (a maximum of 1180 ^{o}C) in the advancing side than the retreating side (Figure 5.21), which is typical in FSW [5.34]. A narrower TMAZ and HAZ was obtained by optimising the process parameters in the LAFSW-10 model as compared to the FSW-1 model. It was reported by Micallef et al. [5.35] for FSW of steel DH36 that the width of the TMAZ and HAZ were considerably reduced by increasing the traverse speed.

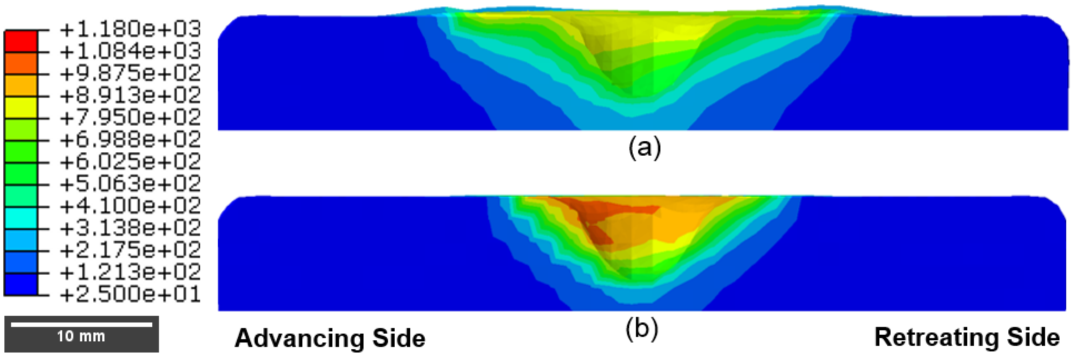

Figure 5.21: Temperature distribution in °C in the cross sectional views at the traverse stage of (a) FSW-1 model without laser heating, (b) LAFSW-10 model with 20 mm heat source distance. (Tool rotation: Anticlockwise direction).

5.2.5.3. Plastic strain

A maximum plastic strain of 20.66 has been recorded at the plunge stage for the LAFSW-10 model, as shown in Figure 5.22. Unlike other FSW and LAFSW models with 500 mm/min displayed in Figure 5.11, the material is deformed closer to the weld centreline, hence forming a smoother and narrower TMAZ (Figure 5.22). It is apparent that the plastic strain is not symmetrical along the weld centreline, and the advancing side has relatively higher values of plastic strain than the retreating side. The application of laser heating has helped in improving the material flow even at higher traverse speed. The high plastic strain in the centre of the TMAZ in Figure 5.23 corresponds to the accumulation of the weld nugget, as indicated by previous researches [5.36,5,37]. This can be observed that the weld nugget is slightly offset towards the advancing side from the tool centreline. The plastic strain distribution on the cross section appeared to be coarser on the advancing side. The reason for this phenomenon can be linked to the increased rotational and traverse speeds, hence causing the workpiece material to flow vigorously behind the tool. A refined weld zone is therefore obtained by the vigorous material flow during the process [5.38]. It was also reported by Song et al. [5.13] that a sufficient heat input by the laser heating could result in a refined weld zone at increased traverse speeds.

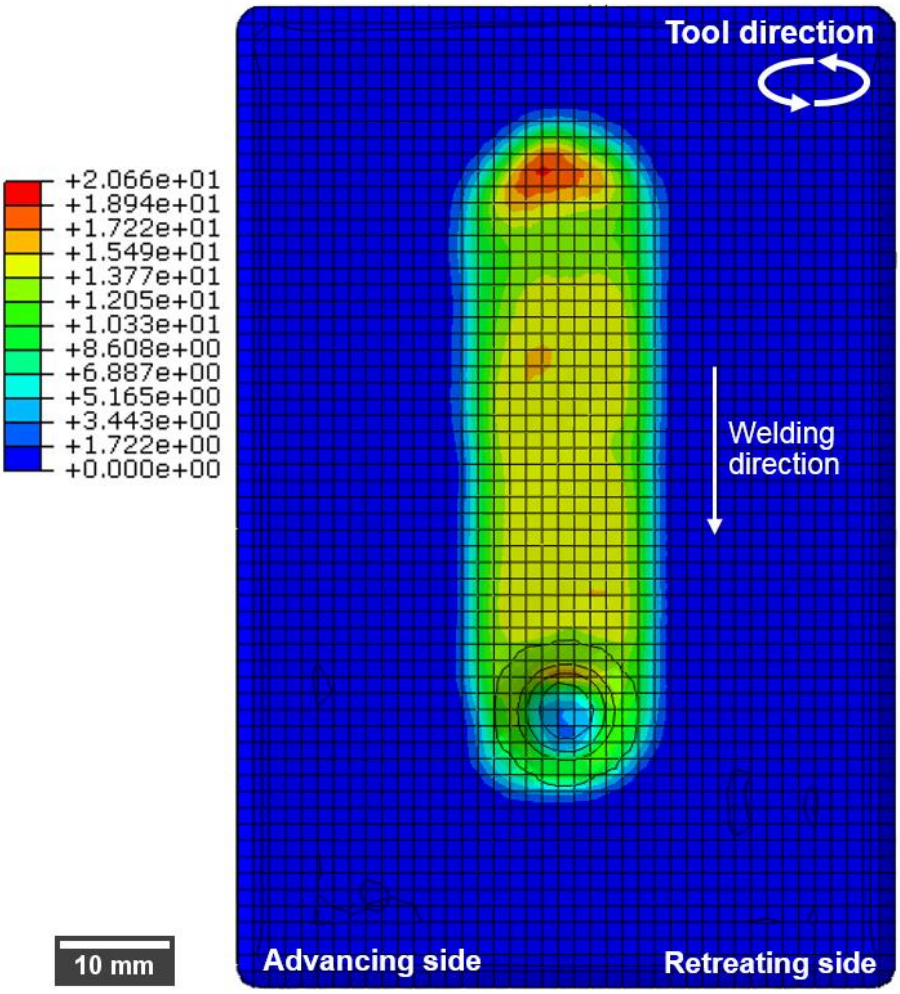

Figure 5.22: Equivalent plastic strain in the top view of the optimised LAFSW-10 model.

To compare the results at the increased traverse speed, an FSW model was simulated without any laser heat assistance, named as FSW-3 model in Table 5.2. As the weld quality is significantly influenced by the preheating [5.39], the results showed initiation of potential defects in the weld region without the laser heat assistance (Figure 5.24). It was discussed in section 4.2.6 that minimum amount of flash was produced with the use of fast process parameters than the slow ones. Similarly, minimal to no flash was produced with the optimised process parameters. This provides further evidence on the advantages of laser heating assistance at considerably higher welding speeds.

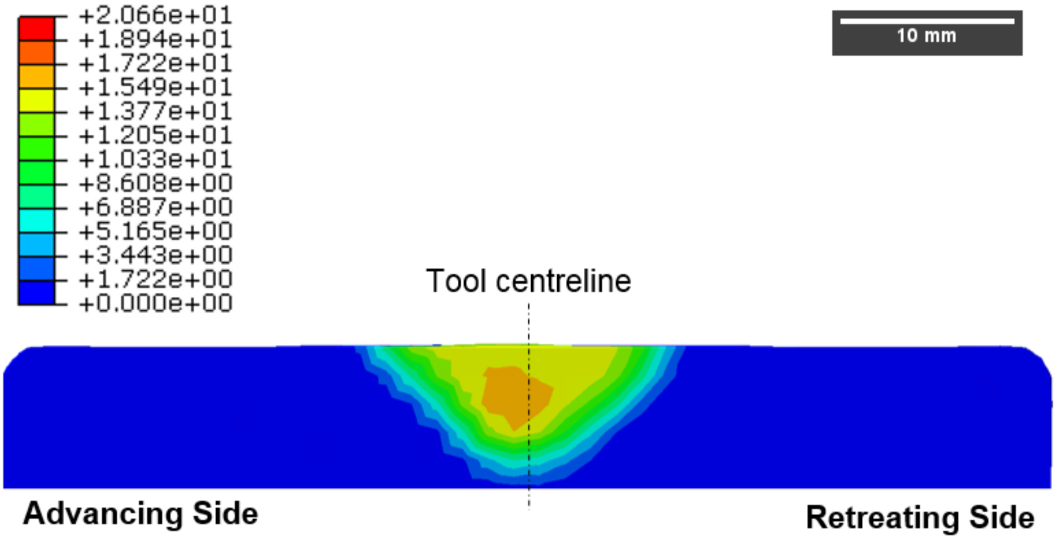

Figure 5.23: Equivalent plastic strain in the cross sectional view of the optimised LAFSW-10 model. (Tool rotation: Anticlockwise direction).

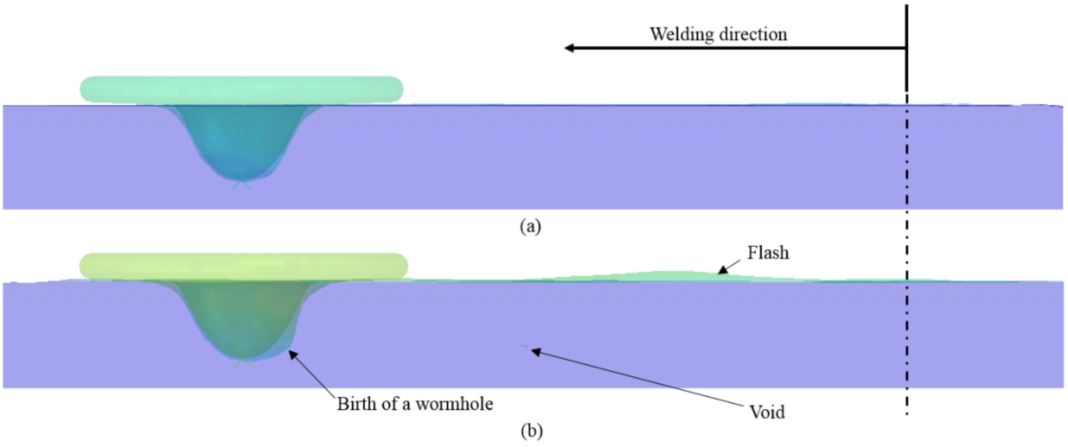

Figure 5.24: Visualisation of flash and weld defects from the side view in the (a) LAFSW-10 model, (b) FSW-2 model.

5.3. Conclusions

Fully coupled thermomechanical FSW and LAFSW models have been developed in Abaqus/Explicit. The use of experimentally generated temperature dependent material properties for low alloy steel grade DH36 and the CEL approach assisted in generating more accurate results than the other modelling techniques used in the relevant technical literature for laser assistance. Experimentally applicable laser heating parameters were used as a preheating and moving heat source in LAFSW. Reaction forces on the tool probe tip along with the temperature distribution, plastic strain and material flow in the workpiece were evaluated to calculate the most suitable distance between the tool and the moving heat source.

Preheating the workpiece prior to the tool plunge reduced the tool reaction forces up to 55% as compared to the plunge stage of conventional FSW. It was observed that sufficient heat could be dissipated in the TMAZ within 5 seconds of heating before the plunge stage. Therefore, the preheating is likely to assist in reducing the total duration of the dwell stage without compromising the overall temperature distribution in the TMAZ and HAZ. A distance of 20 mm between the laser heat source and the tool predicted the lowest tool reaction forces during the traverse stage, and an increased temperature and plastic strain distribution in the workpiece throughout the process. The resultant material flow was significantly enhanced due to the preheating of the workpiece as compared to the FSW model.

Optimised process parameters were developed to achieve defect free welds and minimise the reaction forces on the tool during LAFSW. It was concluded that by using LAFSW with the specified conditions, a maximum traverse speed of 1500 mm/min (with a rotational speed of 1800 rpm) could be achieved without compromising the weld quality. This represents a considerable increase compared to the previously achieved welding speeds for steel FSW. Moreover, the reaction forces were significantly reduced with the application of a smaller distance between the heat source and the tool during the traverse stage.

From this work, laser heating has been demonstrated to be an efficient and convenient assisted energy method in terms of providing defect free welds and a readily available addition to currently operational FSW equipment. As a result of the substantial increase in traverse speed that may be achievable on steel, LAFSW has the capability to enhance the productivity in potential industrial applications.

5.4. References

[5.1] Álvarez AI, Cid V, Pena G, Sotelo J, Verdera D. Assisted friction stir welding of carbon steel: Use of induction and laser as preheating techniques. Frict Stir Weld Process VII 2016:117–26. doi:10.1007/978-3-319-48108-1_13.

[5.2] Toumpis A, Galloway A, Cater S, McPherson N. Development of a process envelope for friction stir welding of DH36 steel - A step change. Mater Des

2014;62:64–75. doi:10.1016/j.matdes.2014.04.066.

[5.3] Toumpis A, Galloway A, Cater S, Micallef D, Camilleri D, Poletz N, et al. Advances in friction stir welding of steel – project HILDA. Transp. Res. Arena, Paris, France: 2014.

[5.4] Toumpis AI, Galloway AM, Camilleri D, Arbaoui L. Recent Developments in Steel Friction Stir Welding: Project HILDA. Proc. ASME 2015 Int. Mech. Eng. Congr. Expo., Houstan: 2015, p. 11. doi:10.1115/IMECE2015-51349.

[5.5] Ahmad B, Galloway A, Toumpis A. Advanced numerical modelling of friction stir welded low alloy steel. J Manuf Process 2018;34:625–36. doi:10.1016/j.jmapro.2018.07.003.

[5.6] Padhy GK, Wu CS, Gao S. Auxiliary energy assisted friction stir welding – status review. Sci Technol Weld Join 2015;20:1362171815Y.000. doi:10.1179/1362171815Y.0000000048.

[5.7] Fedotov I, Fedotova T, Pityana SL, Labuschange K, Shatalov M, Potgieter JH. A mathematical model of laser surface heat-cooling treatment for medium carbon steel. J South African Inst Min Metall 2011;111:379–84.

[5.8] Sun YF, Konishi Y, Kamai M, Fujii H. Microstructure and mechanical properties of S45C steel prepared by laser-assisted friction stir welding. Mater Des 2013;47:842–9. doi:10.1016/j.matdes.2012.12.078.

[5.9] Torkamany MJ, Tahamtan S, Sabbaghzadeh J. Dissimilar welding of carbon steel to 5754 aluminum alloy by Nd:YAG pulsed laser. Mater Des 2010;31:458–65. doi:10.1016/j.matdes.2009.05.046.

[5.10] Kohn G, Greenberg Y, Makover I, Munitz A. Laser-assisted friction stir welding. Weld J 2002;81:46–8.

[5.11] Chang WS, Rajesh SR, Chun CK, Kim HJ. Microstructure and Mechanical Properties of Hybrid Laser-Friction Stir Welding between AA6061-T6 Al Alloy and AZ31 Mg Alloy. J Mater Sci Technol 2011;27:199–204. doi:10.1016/S1005-0302(11)60049-2.

[5.12] Able N, Pfefferkorn F. Laser-assisted friction stir lap welding of aluminum. ASME Summer Heat Transf. Conf., San Francisco: 2005, p. 425–9. doi:10.1115/HT2005-72829.

[5.13] Song KH, Tsumura T, Nakata K. Development of Microstructure and Mechanical Properties in Laser-FSW Hybrid Welded Inconel 600. Mater Trans 2009;50:1832–7. doi:10.2320/matertrans.M2009058.

[5.14] Wu CS, Zhang HT, Chen J. Numerical simulation of keyhole behaviors and fluid dynamics in laser–gas metal arc hybrid welding of ferrite stainless steel plates. J Manuf Process 2017;25:235–45. doi:10.1016/j.jmapro.2016.11.009.

[5.15] Daftardar S. Laser Assisted Friction Stir Welding: Finite Volume Method and Metaheuristic Optimization. Louisiana State University, 2009.

[5.16] Casavola C, Cazzato A, Moramarco V. Thermographical Analysis of Friction Stir Welding and Laser Assisted Friction Stir Welding. XIII Youth Symp. Exp. Solid Mech., Decin, Czech Republic: 2014, p. 15–9.

[5.17] Campanelli SL, Casalino G, Casavola C, Moramarco V. Analysis and comparison of friction stir welding and laser assisted friction stir welding of aluminum alloy. Materials (Basel) 2013;6:5923–41. doi:10.3390/ma6125923.

[5.18] Gabriel K. Process and Apparatus for Friction Stir Welding, 2005.

[5.19] Simulia 6.14. Abaqus Documentation. 34.4.4 Thermal Loads 2014.

[5.20] Rai R, De A, Bhadeshia HKDH, DebRoy T. Review: friction stir welding tools. Sci Technol Weld Join 2011;16:325–42. doi:10.1179/1362171811Y.0000000023.

[5.21] Sinclair PC, Longhurst WR, Cox CD, Lammlein DH, Strauss AM, Cook GE. Heated friction stir welding: An experimental and theoretical investigation into how preheating influences process forces. Mater Manuf Process 2010;25:1283–91. doi:10.1080/10426914.2010.496122.

[5.22] Yu M, Li WY, Li JL, Chao YJ. Modelling of entire friction stir welding process by explicit finite element method. Mater Sci Technol 2012;28:812–7. doi:10.1179/1743284711Y.0000000087.

[5.23] Fei X, Ye Y, Jin L, Wang H, Lv S. Special welding parameters study on Cu/Al joint in laser-heated friction stir welding. J Mater Process Technol 2018;256:160–71. doi:10.1016/j.jmatprotec.2018.02.004.

[5.24] Sundqvist J, Kim K, Bang H, Bang H, Kaplan AFH. Numerical simulation of laser preheating of friction stir welding of dissimilar metals. Sci Technol Weld Join 2018;23:351–6. doi:10.1080/13621718.2017.1391936.

[5.25] Potluri H, Jones JJ, Mears L. Comparison of Electrically-Assisted and Conventional Friction Stir Welding Processes by Feed Force and Torque. ASME 2013 Int. Manuf. Sci. Eng. Conf., Madison: 2013, p. 10. doi:10.1115/MSEC2013-1192.

[5.26] Guerra M, Schmidt C, McClure JC, Murr LE, Nunes AC. Flow patterns during friction stir welding. Mater Charact 2002;49:95–101. doi:10.1016/S1044-5803(02)00362-5.

[5.27] Nami H, Adgi H, Sharifitabar M, Shamabadi H. Microstructure and mechanical properties of friction stir welded Al/Mg2Si metal matrix cast composite. Mater Des 2011;32:976–83. doi:10.1016/j.matdes.2010.07.008.

[5.28] Bang HS, Bang HS, Jeon GH, Oh IH, Ro CS. Gas tungsten arc welding assisted hybrid friction stir welding of dissimilar materials Al6061-T6 aluminum alloy and STS304 stainless steel. Mater Des 2012;37:48–55. doi:10.1016/j.matdes.2011.12.018.

[5.29] Arora A, De A, Debroy T. Toward optimum friction stir welding tool shoulder diameter. Scr Mater 2011;64:9–12. doi:10.1016/j.scriptamat.2010.08.052.

[5.30] Fraser KA, St-Georges L, Kiss LI. Optimization of friction stir welding tool advance speed via monte-carlo simulation of the friction stir welding process. Materials (Basel) 2014;7:3435–52. doi:10.3390/ma7053435.

[5.31] Merklein M, Giera A. Laser assisted Friction Stir Welding of drawable steel-aluminium tailored hybrids. Int J Mater Form 2008;1:185–8. doi:10.1007/s12289-008-0141-x.

[5.32] Nandan R, Roy GG, Lienert TJ, DebRoy T. Numerical modelling of 3D plastic flow and heat transfer during friction stir welding of stainless steel. Sci Technol Weld Join 2006;11:526–37. doi:10.1179/174329306X107692.

[5.33] Colegrove PA, Shercliff HR. 3-Dimensional CFD modelling of flow round a threaded friction stir welding tool profile. J Mater Process Technol 2005;169:320–7. doi:10.1016/j.jmatprotec.2005.03.015.

[5.34] Jweeg M, Tolephih MH, M. MA. Effect of friction stir welding parameters (rotation and transverse) speed on the transient temperature distribution in friction stir welding of AA 7020-t53. ARPN J Eng Appl Sci 2012;7:436–46.

[5.35] Micallef D, Camilleri D, Toumpis A, Galloway A, Arbaoui L. Local heat generation and material flow in friction stir welding of mild steel assemblies. Proc Inst Mech Eng Part L J Mater Des Appl 2015;230:586–602. doi:10.1177/1464420715583163.

[5.36] Reynolds AP, Tang W, Posada M, Deloach J. Friction stir welding of DH36 steel. Sci Technol Weld Join 2003;8:455–60. doi:10.1179/136217103225009125.

[5.37] Vijay SJ, Murugan N. Influence of tool pin profile on the metallurgical and mechanical properties of friction stir welded Al-10wt.% TiB2 metal matrix composite. Mater Des 2010;31:3585–9. doi:10.1016/j.matdes.2010.01.018.

[5.38] Sato YS, Harayama N, Kokawa H, Inoue H, Tadokoro Y, Tsuge S. Evaluation of microstructure and properties in friction stir welded superaustenitic stainless steel. Sci Technol Weld Join 2009;14:202–9. doi:10.1179/136217108X386518.

[5.39] Yaduwanshi DK, Pal S, Bag S. Effect of Preheating on Mechanical Properties of Hybrid Friction Stir Welded Dissimilar Joint. 5th Int. 26th All India Manuf. Technol. Des. Res. Conf. (AIMTDR 2014), Guwahati: 2014.

6. Conclusions and future work

This thesis has focussed on the numerical optimisation of the friction stir welding (FSW) of steel, and has been conducted along two themes; development of a fully coupled thermomechanical FSW model for steel, and increasing the traverse speed for steel FSW through laser assisted additional heating.

6.1. Thermomechanically coupled FSW model

A detailed study of the experimental and numerical advancement of steel FSW has been presented. The numerical results present a better level of accuracy for the critical insights of steel FSW such as the detailed temperature distribution, plastic strain and the material flow in the workpiece as compared to the experimental results. Therefore, the literature review has highlighted the need for a fully coupled thermomechanical model as the available technical literature has presented the modelling of steel FSW by considering either the FSW tool as a virtual heating source or the workpiece as a viscous fluid. These simplifications in the models have resulted in simulating solely the traverse stage of FSW, hence ignoring the first two stages (plunge and dwell). In the present work, different material models for FSW have been discussed, and it has been concluded that the temperature dependent material properties can provide accurate numerical results in line with the experimental results. The theoretical background of the FSW models developed in this thesis has been analysed in detail. Governing equations for the thermomechanical fundamentals have been presented. For a fully coupled thermal structural analysis, the feasibility of modelling through implicit and explicit analysis has been discussed.

A shipbuilding low alloy steel grade DH36 was friction stir welded using polycrystalline Boron Nitride (pcBN) tool. The simulation methodology for FSW was implemented in the finite element software Abaqus/Explicit using the coupled Eulerian Lagrangian (CEL) approach. Unlike previous modelling attempts of steel FSW by other research groups, the CEL approach assisted in modelling both the workpiece and the tool as solid bodies. The material behaviour of the steel was discussed with respect to the different strain rates and elevated temperatures. The mechanical and thermophysical material properties of steel were applied to the model. These were previously experimentally generated as a part of a wide ranging investigation. All three stages of FSW, i.e. plunge, dwell and traverse were successfully simulated and presented for two models with diverse process parameters, termed as slow (120 mm/min, 200 rpm) and fast (500 mm/min, 700 rpm) weld models. The models presented an accurate evaluation of the reaction forces on the tool, the temperature distribution, plastic strain, material flow and the flash generation in the weld based on comparisons to the literature. The following conclusions were drawn from the numerical results of both models.

1. The maximum temperature values in the weld were located next to the shoulder interface of both models. The temperature values were higher in the advancing side (AS) than the retreating side (RS) as it has been extensively reported in the literature. The fast weld parameters resulted in a narrower heat affected zone (HAZ) during the traverse stage. However, heat input per unit length was larger in the slow weld model during the traverse stage as more heat was dissipated in the workpiece when the tool was traversed slowly. The direct relation between the tool rotational speed and the temperature profile demonstrates that the dwell time can be reduced by increasing the tool rotational speed, hence potentially increasing industrial productivity. The temperature profiles of both models were in close alignment with the previously published experimental results.

2. The plastic strain was found to be greater in the slow weld model. The thermomechanically affected zone (TMAZ) was identified as the region with maximum plastic strain. The heat generation was increased by increasing the rotational speed, which is why the plastic strain in the TMAZ was inversely related to the rotational and the traverse speed of the tool. A similar pattern of results for plastic strain has been reported in the wider published work. High plastic strain values were located near the tool shoulder as compared to the tool probe tip for both models. This explains the presence of defects at the bottom of the TMAZ in the experiments from the literature.

3. The reaction forces were calculated on the tool probe tip during all stages of FSW. The tool probe tip experienced the maximum reaction forces in both models during the plunge stage. Decreasing the tool’s rotational speed increased the magnitude of the reaction forces on the tool probe. This explains why the tool reaction forces were greater in the slow weld model during the plunge stage. The tool experienced minimal reaction forces during the dwell stage as compared to the other stages due to no translational movement. However, the traverse speed had a direct relation with the reaction forces, which is why the fast weld model had increased reaction forces on

the tool probe tip. Comparable results for the reaction forces on the tool have been reported by experimentally focussed research groups.

4. It was observed that the material flow in the workpiece during FSW is closely related to the tool's rotational speed and the temperature values. The lower rotational speed in the slow weld model tended to establish a strong frictional contact on the tool-workpiece interface, hence enabling the material movement to flow more efficiently. The heat in the dwell stage softened the workpiece region around the tool surface for an enhanced material flow. The material flow in the TMAZ was improved during the traverse stage by increasing the tool's rotational speed. This is partly attributed to an enhanced temperature distribution and an intense virtual vortex created in the trailing edge (see Figure 1.1) of the weld due to the increased tool speed.

5. Maximum flash was observed on the RS of the slow weld model workpiece. This was due to the increased resistance for the material to flow to the trailing edge, hence generating the flash on the surface of the workpiece. The slow traversing speed resulted in lower peak temperatures, hence causing the material on the upper surface of the workpiece to abrade away instead of thermomechanically stirring. The improved material flow due to the increased tool's rotational and traverse speed demonstrated minimal weld surface disruptions in the fast weld model. No weld defects were found in both models, showing that FSW is suitable for diverse process parameters.

The slow process parameters developed a symmetrical TMAZ and HAZ while an asymmetry was produced in the weld zones for the increased process parameters. The numerical models successfully predicted various physical phenomenon of the FSW process. All numerical results were in good agreement with the previously published experimental findings.

6.2. Laser assisted FSW model

The economic viability of steel FSW is constrained by certain issues such as low traverse speed, high cost and short FSW tool life. Recently, auxiliary energy assisted FSW has been used to address these issues for high strength materials. Various auxiliary energies, such as electric, induction, ultrasonic, arc and laser energies, have been reviewed to optimise FSW. Among these, laser assisted friction stir welding (LAFSW) is an extensively applied modification to FSW to date. Therefore, experimental and numerical developments on LAFSW have been thoroughly discussed. Since there is fewer research on steel LAFSW, all stages of LAFSW should be numerically simulated to optimise the process parameters and reduce the reaction forces on the tool.

A laser heat source was modelled during the preheating and traverse stages along with FSW to observe its various effects. The LAFSW models were compared with the FSW results for the fast weld parameters. Different heat source distances from the tool were simulated during the traverse stage. Reaction forces on the tool probe tip along with the temperature distribution and plastic strain in the workpiece were compared to calculate an appropriate distance between the tool and the moving heat source. After a suitable distance was defined, the process parameters were optimised to achieve a defect free weld. The following points were concluded from the LAFSW models:

1. The reaction forces on the tool probe tip in the LAFSW models were significantly decreased during the plunge stage as compared to the FSW model. The preheating of the workpiece assisted in reducing the reaction forces on the tool probe tip up to 55% during the plunge stage. A substantial difference between the forces of FSW and LAFSW was not observed during the traverse stage, as the laser heating did not greatly influence the bottom surface of the workpiece due to the continuous movement in line with the tool. However, it is clear that increasing the laser power would provide sufficient heat dissipation in the bottom surface of the workpiece on the cost of extra softening of the workpiece surface material, hence increasing the flash. The reaction forces on the tool probe tip were least when a distance of 20 mm was applied between the heat source and the tool during the traverse stage as compared to 30 mm and 40 mm.

2. The laser preheating assisted in plastic softening of the workpiece before the tool plunge. It was concluded that sufficient heat could be dissipated in the workpiece region, which will later become the TMAZ, within 5 seconds of heating before the plunge stage. Moreover, the preheating could also help in reducing the total duration of the dwell stage without compromising the general temperature distribution in the TMAZ and HAZ. Similar to the FSW models, all LAFSW models presented higher temperature values in the AS compared to the RS due to the tool rotational direction. A wider cross sectional temperature profile was achieved by the use of smaller

distance between the heat source and the tool during the traverse stage. This is explained by the heat being dissipated away from the weld zone when a larger heat source distance from the tool was used. A distance of 20 mm between the heat source and the tool showed an increased temperature distribution during the traverse stage. This demonstrated the potential applications of using a minimum heat source distance to obtain higher temperature gradients. The higher temperature gradients will increase the material deformation near the tool probe, hence avoiding any weld defects near the bottom surface of the workpiece.

3. The TMAZ in the LAFSW models experienced larger plastic strains than the FSW model. The laser heating produced an irregular TMAZ and HAZ in the AS during the traverse stage due to the excessive softening of the weld zone. The heat source assisted in extra softening of the workpiece’s top surface prior to the tool traverse. A relatively high plastic strain was observed with the smaller distance between the heat source and the tool. This was due to the increased higher temperature gradients in the weld zone, as discussed above.

4. The material flow in the plunge stage was significantly improved by preheating the workpiece as the already increased temperature in the workpiece before the tool plunge assisted in thermal softening of the material. The continuous heating ahead of the tool during the traverse stage enhanced the material flow in the TMAZ. Since sufficient material flow is required for obtaining defect free welds, certain flaws can be avoided in the weld zones by the assistance of laser heat source. The application of laser assistance resulted in an increased flash generation. However, it was concluded that the flash could be reduced by increasing the traverse speed.

5. To optimise LAFSW, various process parameters were analysed to obtain defect free welds at substantially increased traverse speeds. It was observed that LAFSW with a traverse speed of 1500 mm/min and rotational speed of 1800 rpm produced defect free welds, which is up to three times than the maximum traverse speed achieved during the conventional FSW. The reaction forces with the optimised process parameters were minimum in all stages as compared to the fast weld model (500 mm/min, 700 rpm) for both FSW and LAFSW. This shows that the increase in the tool rotational speed does not negatively influence the tool when the heat assistance is used. A narrower temperature profile with increased values was achieved in the optimised LAFSW model than the FSW model during the traverse

stage. The material deformation was mainly restricted in the region near to the weld centreline. The plastic strain was not symmetrical along the weld centreline, and the AS had higher values of plastic strain than the RS. The high plastic strain in the centre of the TMAZ was related to the growth of the weld nugget. As discussed for the increased process parameters in FSW models, less flash was generated during the dwell stage while no flash generation was observed on the workpiece with the optimised traverse speed.

The application of laser heating improved the material flow even at higher traverse speed. Therefore, LAFSW could enhance the productivity in potential industrial applications.

6.3. Future work

The simulation methodologies presented in this thesis have significantly improved the state of the art in the research field of numerical modelling of FSW and LAFSW. In addition, these provide following research prospects for further numerical and experimental work.

1. Based on the temperature distribution in the workpiece, other models can be developed by integrating the existing results for the simulation of the microstructural development during and after FSW.

2. Investigations on the FSW modelling of steel with other dissimilar materials could be conceived by the application of temperature dependent material properties and the CEL approach, so that the tool and the workpieces could be modelled as solids.

3. Like aluminium and low melting temperature alloys, numerical developments should be made on the modelling of complex tool geometries for steel and other high strength alloys to further improve the material stirring in the weld zone.

4. The numerical modelling has provided a substantial understanding of both FSW and LAFSW. However, many important factors, such as the backing plate and the clamping configuration, may influence the concluded results of this thesis. Therefore, experimental examinations should be performed to verify all LAFSW numerical results presented in this thesis, so that FSW could be accepted in the industry as an efficient joining process for steel.

Appendix 1: Publications

The significant outcomes of this work have been published in the journal papers listed below.

1. Ahmad B, Galloway A, Toumpis A. Numerical optimisation of laser assisted friction stir welding of structural steel. Sci. Technol. Weld. Join 2019. doi:10.1080/13621718.2019.1570682.

2. Ahmad B, Galloway A, Toumpis A. Advanced numerical modelling of friction stir welded low alloy steel. J Manuf Process 2018;34:625–36. doi:10.1016/j.jmapro.2018.07.003.